# A NOVEL WAVEGUIDING SOLAR CONCENTRATOR

A Dissertation

by

RAN HUANG

Submitted to the Office of Graduate and Professional Studies of
Texas A&M University
in partial fulfillment of the requirements for the degree of

DOCTOR OF PHILOSOPHY

| | |
|---|---|
| Chair of Committee, | Christi K. Madsen |
| Committee Members, | Ohannes Eknoyan |
| | Jim Ji |
| | Alexey Belyanin |
| Head of Department, | Miroslav M. Begovic |

December 2015

Major Subject: Electrical Engineering

# ABSTRACT

Solar concentrating photovoltaic (CPV) systems have the potential to achieve higher efficiency and reduce total system cost. The main idea of (CPV) technology is to use cheaper optics such as lenses and mirrors to concentrate the sunlight onto a tiny area of photovoltaic (PV) cells. In this case, the required PV cell area is reduced with a given amount collection of incident power.  There are several advantages of CPV systems. First, the cost of the PV system can be reduced by replacing a large area of expensive PV cells with less expensive optical elements, which allows to use the most efficient multijunction (MJ) tandem designed cells which is also the most expensive cells. Also, the efficiency of PV cells can be significant increased under concentrating system. CPV system can be more cost competitive with other PV and electricity generation technologies because of its high efficiency.

However, traditional CPV systems have the problems of the high temperature and non-uniform irradiance on the solar cell at high concentration ratio, which can reduce the performance of the PV cell. Because of these disadvantages of the conventional CPV system, planar waveguides which are used as the secondary optics have been developed for CPV system since 2010. The advantage of the use of the waveguides as the secondary optics is that it can provide uniform illumination on PV cell and may have additional concentration.

Our designed lens-to-channel waveguiding concentrator contains channel waveguides array, a lens array and MJ cells. Compared with the single Fresnel lens, using a lens array as the primary concentrator can not only collect a large amount of solar radiation, but also reduce the thickness and weight of the whole system. In this system, any decoupling loss in the waveguide can be avoided.

The simulation and experiment results of three designed system are presented in this thesis. The concentration ratio can be increased to 920x if using tapered waveguide. A system efficiency of 86% can be achieved by using low loss material as the waveguide.

# DEDICATION

To my family

# ACKNOWLEDGEMENTS

I would like to thank my advisor Dr. Madsen for accepting me as her Ph. D student. It is Dr. Madsen who gave me an opportunity to join Texas A&M University and let me know what I should be capable as a researcher. The most important is that Dr. Madsen always shows her faith in me and encourages me to overcome every difficulty. Working and studying with Dr. Madsen is my great experience and treasure in my life.

I would like to thank my defense committee members Dr. Eknoyan, Dr. Ji and Dr. Belyanin for their guidance and effort to support my Ph. D work.

I would also like to thank my group members and ISSE staffs: Qi Chen, William Snider, Yifeng Zhou, Xin Wang, Jae Hyun Kim, Yuxiao Liu, Dwayne Macik, Chen Zhang, Larry Rehn, Robert Atkins, Jim Gardner and Dennie R. Spears. Thanks you all for the assistance and help in my research work.

Finally, I would like to thank my family, my parents and my girlfriend. It is you who support me and encourage to study in US and finish my Ph. D study.

# TABLE OF CONTENTS

Page

ABSTRACT ........ ii

DEDICATION ........ iv

ACKNOWLEDGEMENTS ........ v

TABLE OF CONTENTS ........ vi

LIST OF FIGURES ........ viii

LIST OF TABLES ........ xii

CHAPTER I INTRODUCTION ........ 1

- 1.1 Renewable energy ........ 1
- 1.2 Solar radiation ........ 3

CHAPTER II SOLAR PHOTOVOLTAIC TECHNOLOGY ........ 11

- 2.1 Introduction to photovoltaic technology ........ 11
- 2.2 Physics of PV cells ........ 11
- 2.3 Theory of solar cells ........ 15
- 2.4 Types of solar cell ........ 20
- 2.5 Multijunction solar cell ........ 25
- 2.6 The cost of PV cell ........ 32

CHAPTER III CONCENTRATING PHOTOVOLTAIC TECHNOLOGY ........ 34

- 3.1 Overview ........ 34
- 3.2 Types of concentrator ........ 35
- 3.3 Optics of Fresnel lens ........ 39
- 3.4 Basic characteristics of CPV system ........ 44
- 3.5 Types of CPV system ........ 47
- 3.6 Losses in CPV system ........ 48

CHAPTER IV INTEGRATED PHOTONICS ........ 56

4.1 Overview ........................................................................................ 56
4.2 Electromagnetic theory of light ........................................................ 58
4.3 Optic waveguide ............................................................................... 60
4.4 Measurement of waveguide losses ................................................... 62

CHAPTER V DESIGN OF LENS-TO-CHANNEL WAVEGUIDING CONCENTRATOR SYSTEM ........................................................ 64

5.1 Overview ........................................................................................ 64
5.2 Structure of lens-to-channel waveguiding concentrator system ...................... 64
5.3 Simulaton and discussion ................................................................. 68

CHAPTER VI DEMONSTRATION OF A MICRO WAVEGUIDING SOLAR CONCENTRATOR ............................................................ 76

6.1 Overview ........................................................................................ 76
6.2 Fabrication process of SU-8 waveguide ........................................... 77
6.3 Measurement setup and results ........................................................ 85
6.4 Conclusion ....................................................................................... 90

CHAPTER VII DEMONSTRATION OF A 2D-WAVEGUIDING SOLAR CONCENTRATOR ............................................................ 92

7.1 Overview ........................................................................................ 92
7.2 Simulation results of the 2d-waveguiding solar concentrator ......................... 93
7.3 Experiment results of the 2d-waveguiding solar concentrator ........................ 95
7.4 Conclusion ..................................................................................... 102

CHAPTER VIII DEMONSTRATION OF AN INTERMEDIATE-SCALE LENS-TO-CHANNEL WAVEGUIDE SOLAR CONCENTRATOR ..................................................... 103

8.1 Overview ...................................................................................... 103
8.2 Structure of the designed system .................................................. 103
8.3 Experiment method ....................................................................... 106
8.4 Results and discussion .................................................................. 111
8.5 Conclusion ..................................................................................... 115

CHAPTER IX CONCLUSION .................................................................. 117

REFERENCES ...................................................................................... 119

# LIST OF FIGURES

FIGURE Page

1. The evidence of global warming that the arctic sea ice is melting. Reprint from [3]. 1

2. Estimated global energy consumption in 2013. Reprint from [4]. 2

3. The potential for renewable energy sources. Reprint from [2]. 3

4. Diagram of ecliptic plane. Reprint from [6]. 4

5. Azimuth, zenith and altitude angle. Reprint from [8]. 5

6. Electromagnetic spectrum. Reprint from [10]. 6

7. Diffuse, direct, and absorbed sun light. 9

8. Solar spectrum of AM0, AM1.5G and AM1.5D. 10

9. Basic solar cell structure. 12

10. Direct and indirect energy band gap. Reprint from [20]. 15

11. The equivalent electrical circuit of an idea PV cell. Reprint from [21]. 16

12. (a) I-V characteristic of a solar cell and (b) the power generated by the cell. Reprint from [21]. 20

13. Market share of solar cell production in 2014. Reprint from [28]. 22

14. Typical structure of CdTe solar cell. Reprint from [21]. 23

15 .The structure of a ZnO/CdS/Cu(In,Ga)$Se_2$ thin film PV cell. Reprint from [21]...... 24

16. Schematic structure of a typical three junction PV cell with related solar spectrum. Reprint from [16]. 26

17. Band gap and lattice constant of semiconductor materials. Reprint from [21]. 28

18. Temperature dependency of current and voltage of polycrystalline silicon solar cell. Reprint from [39]. 31

19. Average price of PV cell and modules from 2003 to 2012. Reprint from [44]. 33

20. Development of efficiencies of MJ cell, CPV modules and system. Reprint from [46]. 35

21. (a) Refractive and (b) reflective concentrators. Reprint from [49]. 36

22. Schematic structure of (a) parabolic dish, (b) parabolic trough and (c) CPC reflector. Reprint from [49]. 37

23. Cross-section of a typical Fresnel lens. Reprint from [53]. 38

24. Transmission efficiency of Fresnel verse f-number based on the facing direction of the grooves. Reprint from [50]. 40

25. Lens efficiency verse f-number. Reprint from [53]. 41

26. Fresnel loss on the surface between the air (n=1) and PMMA (n=1.49) based on different incident angle. 42

27. Schematic of chromatic dispersion and deviation of incident sunlight. Reprint from [53]. 44

28. Description of acceptance angle and concentration ratio. 46

29. Estimated losses in CPV system. Reprint from [58]. 49

30. Hot spot on a PV cell because of the non-uniform irradiance in a Fresnel lens system. Reprint from [58]. 50

31.(a) I-V curve of multijunction PV cell under non-uniform irradiance and (b) examples of non-uniform light patterns on solar cells. Reprint from [68]. 53

32. Temperature dependence of (a) open circuit voltage, (b) short circuit current, (c) fill factor and (d) efficiency of InGaP/InGaAs/Ge PV cell. Reprint from [71]. 55

33. Integrated photonics: combining waveguide technology to several other technologies. 56

34. Common used waveguide: (a) planar waveguide, (b) channel waveguide and (c) optical fiber. Reprint from [72]. 58

35. Refraction of light and total internal reflection. Reprint from [73] 61

36. Experiment setup for waveguide loss measurement by the end-coupling method. Reprint from [75]. 63

37. The top side of the lens-to-channel waveguiding concentrator system. Reprint from [82, 83]. 65

38. The schematic structure of tapered waveguide concentrator. 67

39. The relationship between the spot size, the incident angle and the marginal ray angle. 68

40. Simulation result of the intensity distribution at the waveguide output. 69

41. (a) The incident light with an incident angle; Simulation of (b) ray traces in waveguide and (c) the angle of the reflected light at the coupler surface based on different coupler angle. 75

42. Mask design of straight waveguide and tapered waveguide. 78

43. Photolithography process for making SU-8 waveguide. 79

44. SU-8 spin speed versus thickness. 81

45. The picture of the sample after the spin coating. The photoresist on the edge is removed by Q-tips. 81

46. Key procedures of fabrication process for SU-8 waveguide with 45˚ coupler: (a) thermal oxidation, (b) photoresist spin coating, (c) exposure in the water and (d) development and photograph of (e) the tilt stage and (f) coupler. 84

47. Photograph of the cross section of the polished SU-8. 85

48. Experimental setup for measuring the optical loss of the waveguide. 86

49. The measurement results of (a) the transmission spectrum, (b) propagation loss and coupling loss, and (c) the picture of the waveguide during the measurement. 87

50. Surface uniformity and surface roughness measurement using DekTak surface profiler. 89

51. (a) Experiment setup for the waveguide with a 45˚ coupler and (b) the picture of the measurement. 90

52. The maximum achievable waveguide concentration for the system. 95

53. A PMMA waveguide is made by CO2 laser cutter. 96

54. (a) Full Spectrum H-Series 20×12 $CO_2$ laser cutter and (b) the control panel of RetinaEngrave3D. 97

55. (a) The waveguide loss is measured by cut back method with a 532 nm laser. (b) The loss versus waveguide curve is obtained by shorten the waveguide. 98

56. Experiment setup for measuring optical efficiency of the system. 99

57. The demonstration of 1×3 lens-to-channel waveguiding concentrator system. 102

58. The relationship between the incident angle, coupler angle and efficiency for PMMA waveguide. 105

59. (a) A 3D view of lens-to-channel waveguide system with separated 45° coupler. (b) Side view and (c) top view of the system. 106

60. Photograph of (a) 8 ×8 Fresnel lens array, (b) waveguide holder stage and (c) the output of waveguide. 107

61. Optical measurement setup for measuring (a) the intensity of the waveguide output and (b) the incident sunlight. 109

62. Angular response of photodiode and ideal cosine response. (b) Linearity response of photodiode. 110

63. Measurement setup of the lens-to-channel waveguide system with a MJ cell. 111

64. The simulation model in ZEMAX. 112

65. Measurement result of MJ cell V-I curve. 114

# LIST OF TABLES

TABLE Page

1. The energy band gap of some semiconductor materials at 300K [18, 19]. .................. 14

2. Confirmed solar cell efficiencies [27]. ........................................................................ 29

3. Spectral loss calculation for three junction PV cell .................................................... 71

4. Spectral loss calculation for four junction PV cell...................................................... 72

5. Fabrication parameters of two samples. ...................................................................... 88

6. Simulation results of lens-to-waveguide system. ........................................................ 94

7. The experiment results of lens-to-channel waveguide system. ................................. 101

8. ZEMAX simulation results of the system. ................................................................ 113

9. Detected power verse distance from waveguide output. ........................................... 113

10. Measurement results of current system and estimated efficiency of the system with better components. ...................................................................... 115

# CHAPTER I

# INTRODUCTION

## 1.1 Renewable energy

Energy plays the most significant role in the world and sustained energy supply is important for all countries today. Most of the electrical power is generated using fossil fuels, which also produce air pollution every second and will run out eventually. In recent decades, the increased demands for energy result in environment and health problems such as air pollution, global warming and water quality [1, 2]. The burning of coal which is one of the essential fuel generates both $CO_2$ and particulates, which produces a greenhouse effect and increases the temperature of the Earth. Figure 1 shows the evidence of global warming that the arctic sea ice is melting [3].

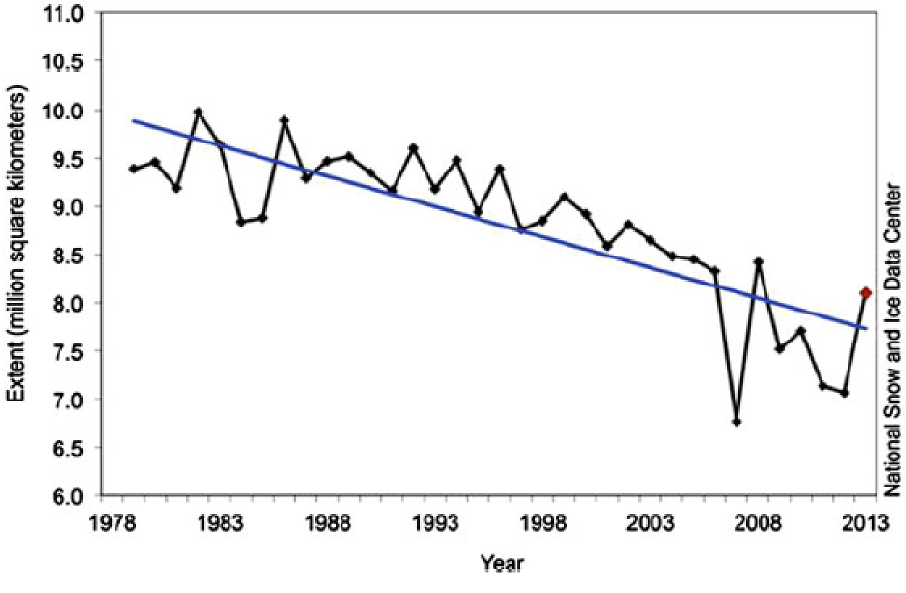

Figure 1. The evidence of global warming that the arctic sea ice is melting. Reprint from [3].

Unlike fossil fuels, renewable energy is clean and cause less harm to the environment. More importantly, renewable energy is essentially inexhaustible. Figure 2 shows the estimated global energy consumption in 2013, 78.3% of the energy consumption comes from fossil fuels such as coal and oil, 19.1% of the energy is generated by renewable energy and only 1.3% of energy is developed by wind, solar, biomass and geothermal power [4]. Thus, it is critical to develop an affordable and environmentally friendly energy for human living and meet energy needs in future.

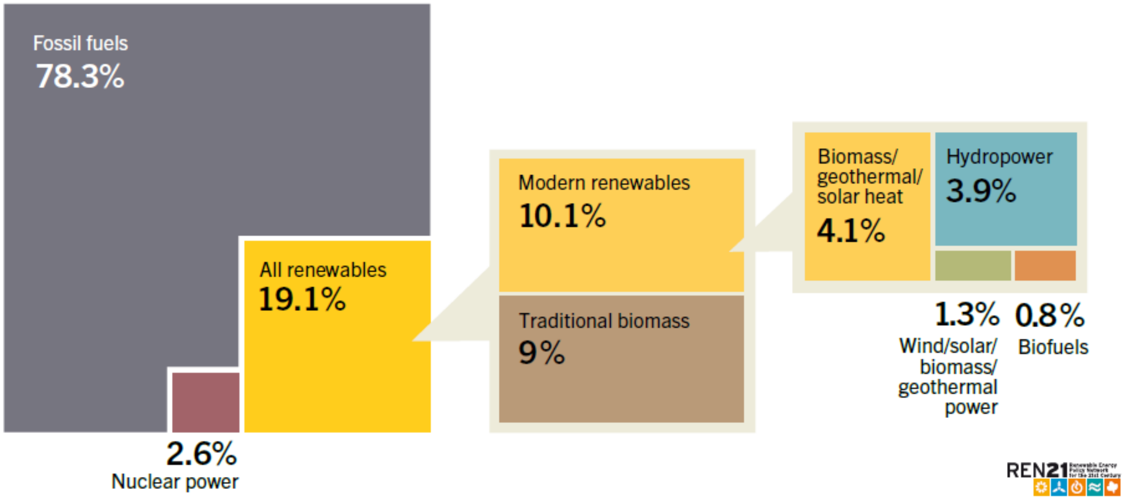

Figure 2. Estimated global energy consumption in 2013. Reprint from [4].

As we all known, solar energy is inexhaustible, free and clean. Also, sun light is the most plentiful energy source for the Earth, which does not emit carbon dioxide. All nations can receive the solar radiation equally and fairly. There is no expense and investment for collecting sunlight. Moreover, solar energy has great potential to meet huge energy demands for the future, which is shown in Figure 3 [2]. All the solar energy received on the Earth in one day can make people live for more than 20 years [2].

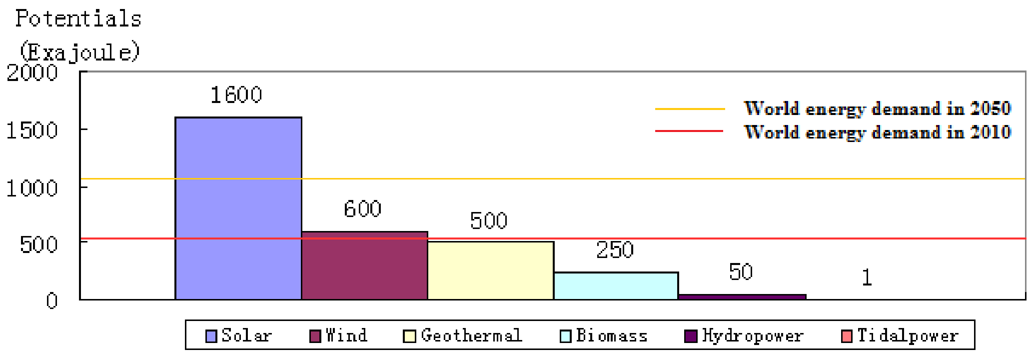

Figure 3. The potential for renewable energy sources. Reprint from [2].

### 1.2 Solar radiation

If the Earth is used as the reference, the sun moves around the Earth in a slightly elliptical path. The sun’s path is called the ecliptic, which is shown in Figure 4. The tilt angle between the Earth’s spin axis and the Earth solar orbit is around 23.5°. The tilted rotation axis causes the daily changes of the sun’s path and the changes of the seasonal weather [5].

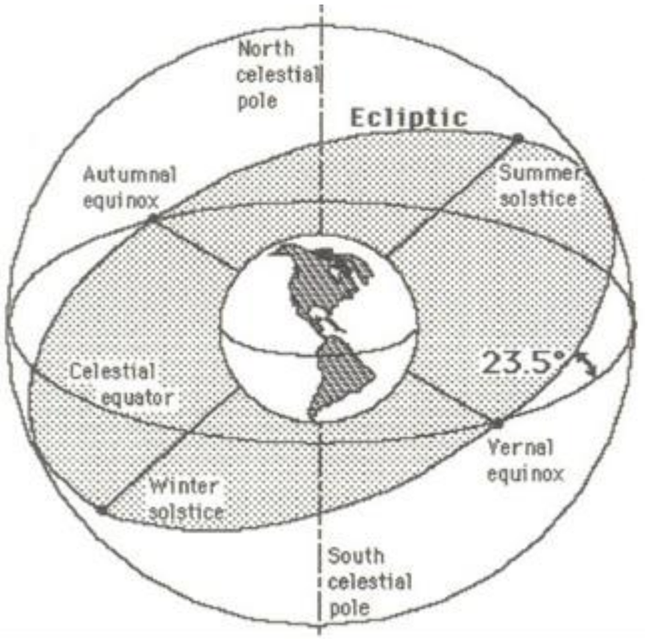

Figure 4. Diagram of ecliptic plane. Reprint from [6].

The mean distance between sun and Earth is called one astronomical unit which is:

$$1 \text{ AU} = 1.496 \times 10^8 \text{ km} \tag{1.1}$$

The minimum distance between sun and Earth is around 0.983 AU and happens around the first week in January; the maximum distance is about 1.017 AU and happens around the first week of July [5, 7]. The total of solar radiation that can reach the Earth is inversely proportional to the square of the distance between the sun and the Earth.

The sun path and solar location of sunrise and sunset vary for different location because of the tilted rotation angle. Solar elevation and azimuth angle are usually used to determine the solar position, which is shown in Figure 5. The altitude angle or elevation angle are obtained from the horizontal to the height of the sun. The zenith angle is also used to locate sun's position, which is measured from vertical to the height of the sun. The azimuth angle is the compass angle, which is obtained in clockwise from north.

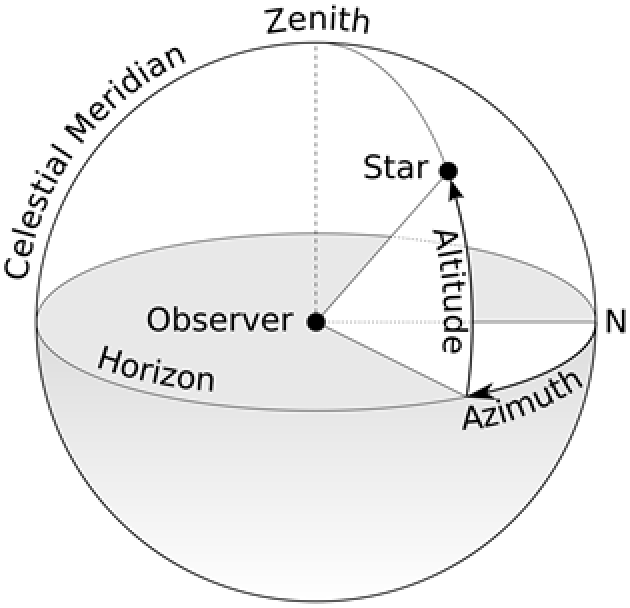

Figure 5. Azimuth, zenith and altitude angle. Reprint from [8].

The angle between the ecliptic plane and the equatorial plane of the Earth is called the declination angle which also varies with different season because of the tiled rotation angle of the Earth. The declination angle δ can be calculated as [9]:

$$\delta = \sin^{-1}\left(\sin\left(23.45°\right)\cdot\sin\left(\frac{360}{365}\left(d-81\right)\right)\right) \tag{1.2}$$

where d is the day of the year. For example, d is 1 for January 1st. The declination angle of the sun varies from -23.45˚ to +23.45˚, since the tilted angle of the Earth is 23.45˚.

Most of the solar radiation that can reach to the Earth is in the thermal radiation range which is shown in Figure 6. Thermal radiation is commonly called light and heat, which is emitted by bodies in the form of electromagnetic waves. Frequency of an electromagnetic wave is defined as

$$\upsilon = \frac{c_0}{\lambda_{vac}} \tag{1.3}$$

where $c_o$ is the speed of the electromagnetic wave in vacuum which is 2.998 $\times 10^8$ m/s; λ is wavelength of the electromagnetic wave. The speed of an electromagnetic wave in a medium is defined as

$$c = \frac{c_0}{n} \tag{1.4}$$

where n is the refractive index of the medium. The wave number or wave vector k is defined as:

$$k = \frac{1}{\lambda} \tag{1.5}$$

Thus, the solar radiation can travel from the sun to Earth in about 8 minutes.

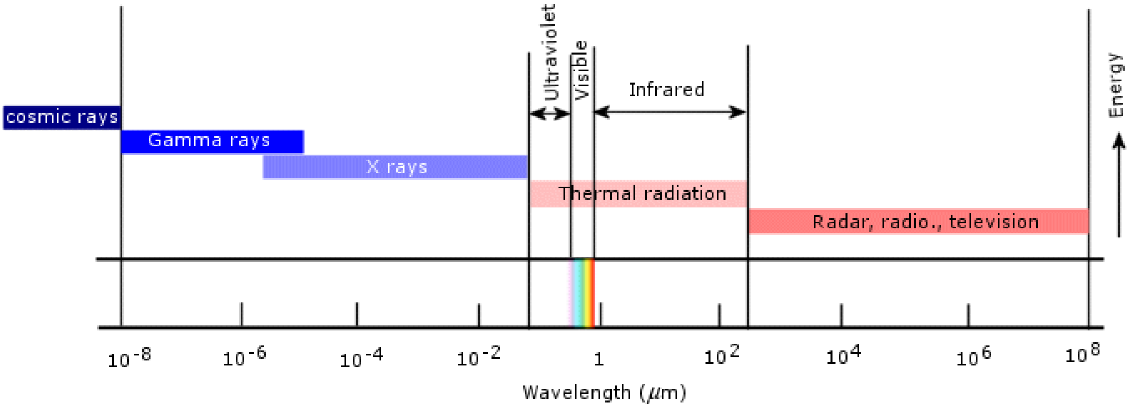

Figure 6. Electromagnetic spectrum. Reprint from [10].

Solar radiation spectrum can be divided into three sections based on the wavelength and photon energy, such as ultraviolet, visible and infrared radiation. The relationship between the photon energy E and wavelength λ is defined as:

$$E(J) = \frac{hc}{\lambda} \tag{1.6}$$

where h is Planck’s constant and the unit is Joule. Another usually used unit of energy is eV (electron-volt), which is defined as:

$$E(eV) = \frac{1.24}{\lambda(\mu m)} \tag{1.7}$$

The wavelength of ultraviolet radiation is between 100 nm to 400 nm, which is about 10% of total energy that can reach the Earth from the sun. Most of the ultraviolet radiation is absorbed by the Earth’s atmosphere. Most of the sun light that can reach the Earth is the radiation in visible range. The visible spectrum is between 400 nm to 800 nm, which consists of different colors. Also, this part of the spectrum is mainly collected by PV equipment and used to generate electricity. The infrared spectrum can be divided into two portions: near infrared and far infrared, which is useful to generate heat and electricity [7, 11].

The surface temperature of the sun is around 5777K. If the sun is considered as a black body which absorbs all electromagnetic waves in all directions and all wavelength and emits energy at all wavelength of the electromagnetic wave, most of the energy of the sun would be in the short wavelength range. The range of solar radiation is mainly within the wavelength from 300 nm to 4000 nm [7].

Power density or intensity are used to define the solar radiation, and the unit is watts per square meter of area (W/m$^2$) [5]. The highest intensity of sunlight that is measured at the top of the Earth's atmosphere is around 1367 W/m$^2$ [11], which is called solar constant. Solar constant is defined as the mean solar irradiance on a unit area that is perpendicular to the rays of the sun at a distance of one astronomical unit (AU) from the sun [7]. The solar constant includes the solar energy at all wavelength and varies by 3.4% [12].

However, when sun light arrives on the ground of the Earth, it is attenuated by the scattering and absorption in the atmosphere of the Earth which can be divided into two types: atmosphere with clouds and atmosphere without clouds. The maximum solar radiation can be collected under clear and cloudless skies which consists of about 78% nitrogen, 21% oxygen, 1% argon and 0.33% carbon dioxide [7]. Except for air molecules, the clean air also contains water vapor and aerosols.

When sun light passes through the atmosphere of the Earth, the light intensity is reduced to around 900-1100 W/m$^2$by scattering and absorption, which is shown in Figure 7. The scattered light by particles and molecules in the atmosphere which arrives on the ground is called diffuse radiation or diffuse horizontal irradiance (DHI). The light that arrives on the ground on a straight line from the sun is called beam radiation, also called direct radiation or direct normal irradiance (DNI). The total solar irradiance including diffuse horizontal irradiance (DHI) and direct normal irradiance (DNI) is called global horizontal irradiance (GHI). The relationship between DNI, DHI and GHI can be expressed by the equation [5]:

$$GHI = DNI \cdot \cos(\theta) + DHI \tag{1.8}$$

where θ is the angle of the incident light which is measured from the vertical.

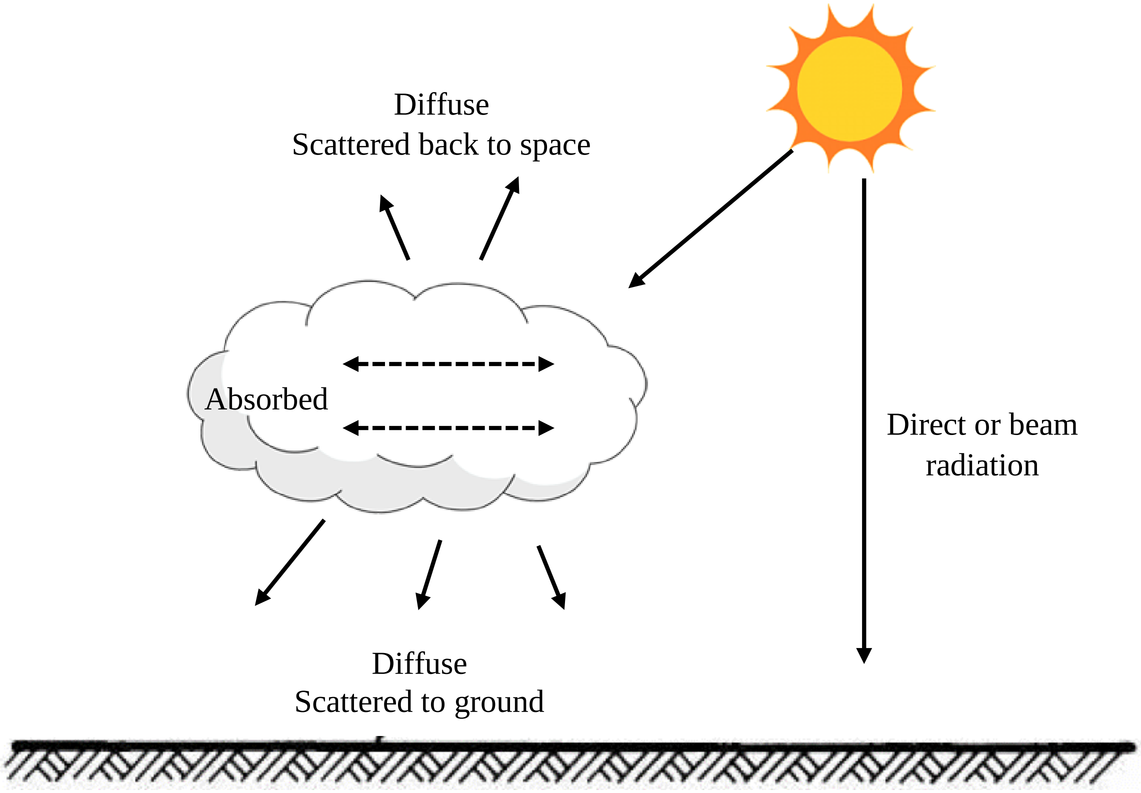

Figure 7. Diffuse, direct, and absorbed sun light.

When the position of the sun is very high in the sky, direct and diffuse solar radiation are about 85% and 15% of the total radiation that received by the ground. When the sun is lower in the sky, the maximum percentage of the diffuse radiation is around 40% [13]. Also, the percentage of the diffuse radiation is higher in the places with high latitude and more cloud.

The “air mass” is defined as the shortest path length that light takes through the atmosphere and reach to the ground [5]:

$$AM = \frac{1}{\cos(z)} = \frac{1}{\sin(e)} \tag{1.9}$$

where z is the zenith angle which is obtained from vertical, e is the elevation angle. AM 1.5 Direct (AM1.5D) and AM 1.5 Global are used as the standard terrestrial solar spectral irradiance for all standardized testing or rating solar cells or modules by the American Society for Testing and Materials (ASTM) [14]. AM 1.5 spectral irradiance is obtained at a zenith angle of 48.2˚. The reason that AM 1.5 spectra was chosen as the standard spectral irradiance is that AM 1.5 is studied to be the average conditions for the 48 contiguous states of the United States of America over a period of one year [14]. AM 0 means there is no atmosphere, which is the solar spectrum in space. Figure 8 shows the spectrum of AM 1.5D and AM1.5G.

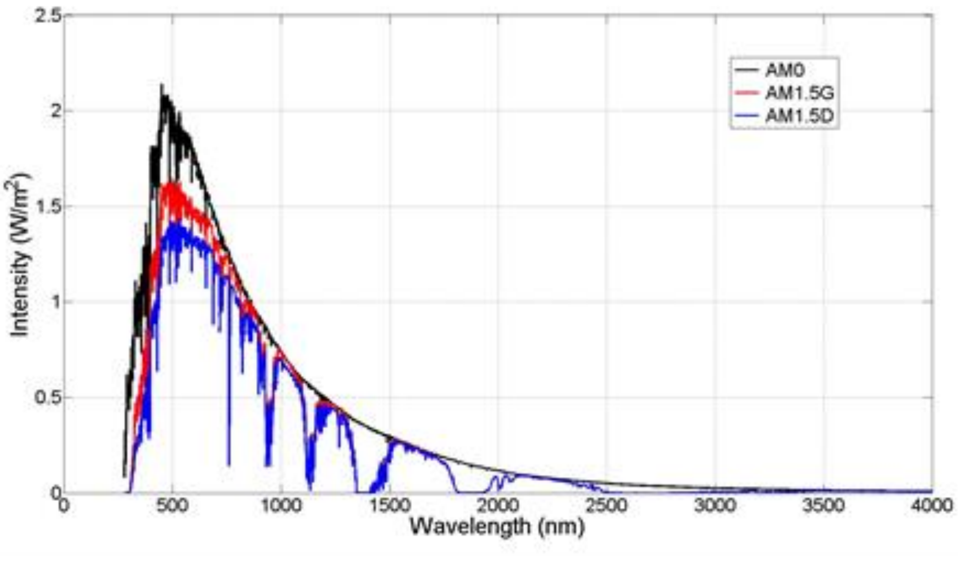

Figure 8. Solar spectrum of AM0, AM1.5G and AM1.5D.

# CHAPTER II

# SOLAR PHOTOVOLTAIC TECHNOLOGY

## 2.1 Introduction to photovoltaic technology

Photovoltaic (PV) technology is the most important and effective method to convert solar energy to electricity. Photovoltaic effect was first time observed by Henri Becquerel in 1839 [15, 16]. In 1954, the first silicon PV cell was established by Chapin et al, which had an efficiency of 6% [16, 17].

Compared with other technology for generating electricity, the advantage of PV technology is that it can direct convert solar energy into electricity with no noise, no pollution, low temperature and long lifetime.

## 2.2 Physics of PV cells

Figure 9 shows the typical solar PV cell structure which consists of a contact layer, an antireflection (AR) layer, an emitter and a base layer. Solar PV cell is generally made from semiconductor materials. The most critical component of the PV cell is p-n junction which can absorb photons and generate electron-hole pair and current. For silicon solar cell, n type semiconductor is usually produced by doping silicon with phosphorus (P) which has five electrons in its outer shell. Phosphorus is called donor in silicon. Since silicon has a valance of four, the extra electron creating by doping phosphorus is easily to be excited to the conduction band. In this case, negatively charged electrons are the dominant carrier for the current. In the opposite way, p type semiconductor can be made by doping Boron (B) to silicon. Boron has three electrons in the outer shell and is called acceptor in silicon. Positively charged holes are the dominant current carrier of p type semiconductor. P-n junction can be created by combining n type and p type semiconductor material into contact [18].

When the incident sunlight hit on the solar cell surface, semiconductor material will absorb incident photons to generate heat and electron. If the energy of the incident photon is larger than the energy band gap of the semiconductor material, electron-hole pairs will be created. The generated electron-pairs are divided by the flow to the external circuit and electric field of the p-n junction [16, 18].

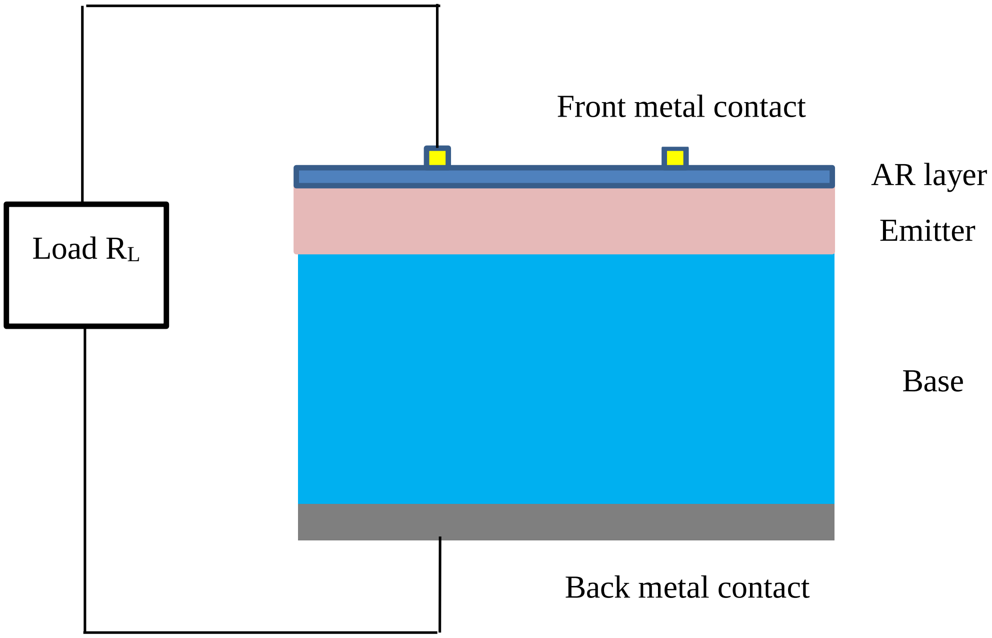

Figure 9. Basic solar cell structure.

The energy gap $E_g$ of a semiconductor material is the minimum energy required to excite an electron from the valence band $E_v$ to the conduction band $E_c$ [18], which is defined as:

$$E_g = E_c - E_v \tag{2.10}$$

So as to excite an electron from valence band to the conduction band, it is required that the incident photon energy is larger than the energy of the band gap. The relationship between the wavelength and the energy of the band gap is given by:

$$\lambda = \frac{h \cdot c}{E_g} \tag{2.2}$$

where h is Planck’s constant and c is the speed of light. For example, the energy band gap of silicon is 1.12 eV, the maximum wavelength of the light that silicon can absorb is around 1100 nm. Table 1 shows the energy band gap of some semiconductor materials.

Table 1. The energy band gap of some semiconductor materials at 300K [18, 19].

| Material | Symbol | Band gap $E_g$ (eV) |
|---|---|---|
| Silicon | Si | 1.12 |
| Gallium arsenide | GaAs | 1.43 |
| Germanium | Ge | 0.67 |
| Gallium phosphide | GaP | 2.25 |
| Indium phosphide | InP | 1.35 |
| Silicon carbide | SiC | 2.2 |
| Gallium antimonide | GaSb | 0.7 |
| Silicon dioxide | $SiO_2$ | 9 |
| Cadmium telluride | CdTe | 1.44 |

Generally, there are two kinds of energy band gap: indirect band gap and direct band gap, which is shown in Figure 10. The minimum energy required to generate electron-hole pairs of a semiconductor material with direct energy band gap is the energy gap itself, such as Gallium Arsenide (GaAs). In the case of indirect energy band gap such as Silicon (Si), since the maximum of the valence band and the minimum of the conduction band are not at the same momentum, more energy is required to generate electrons from valence band to conduction band. Therefore, the absorption efficiency of the semiconductor material with indirect band gap is lower than the material with direct band gap. In this case, optical devices such as LEDs and semiconductor lasers are usually made from the semiconductor material with direct band gap such as GaAs.

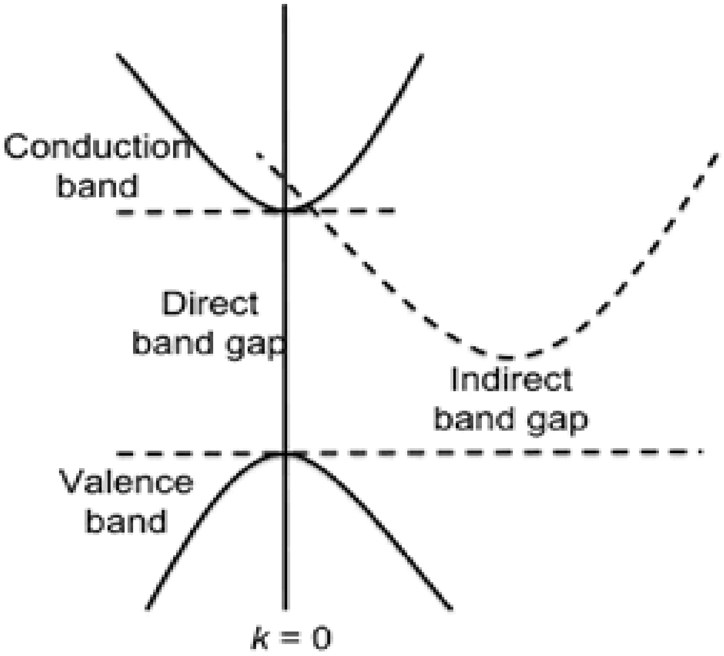

Figure 10. Direct and indirect energy band gap. Reprint from [20].

### 2.3 Theory of solar cells

In electrical circuit, a PV cell can be described by a current source which is connected with a diode in parallel. The equivalent electrical circuit of a PV cell is shown in Figure 11. The current can be calculated by Shockley PV cell equation [18]:

$$I = I_{ph} - I_o \left( e^{\frac{qV}{k_B T}} - 1 \right) \tag{2.3}$$

Where $I_{ph}$ is the photogenerated current which is related to the incident photon flux, $I_o$ is the diode saturation current which is the sum of injection current and generation recombination current, T is the absolute temperature, $k_B$ is the Boltzmann constant, V is the voltage of the cell and q is the electron charge [21].

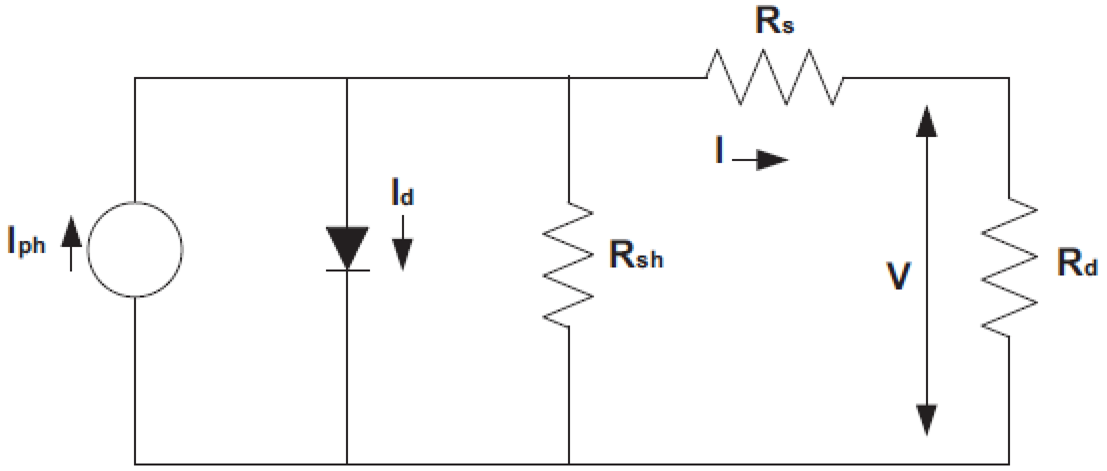

Figure 11. The equivalent electrical circuit of an idea PV cell. Reprint from [21].

In Figure 11, Rp and Rs are shunt resistance and series resistance, respectively. Series resistance consists of three parts: the resistance between the semiconductor material and the metal contact, the resistance of the front and back metal contacts and the movement of the current from base and emitter material. The fill factor can be reduced due to the large series resistance and the current becomes as:

$$I = I_{ph} - I_o \cdot \exp\left(\frac{q \cdot (V + I \cdot R_s)}{k_B \cdot T}\right) \tag{2.4}$$

The shunt resistance which is mainly due to the manufacturing defects can reduce the current passing through the PV cell junction and have power losses in PV cells, particularly severe at low light levels. Considering the effect of a shunt resistance, the current becomes as:

$$I = I_{ph} - I_o \cdot \exp\left(\frac{q \cdot V}{k_B \cdot T}\right) - \frac{V}{R_p} \tag{2.5}$$

In the equivalent electrical circuit of an actual PV cell, the current is given with series resistance and shunt resistance:

$$I = I_{ph} - I_o \cdot \exp\left(\frac{q \cdot (V + I \cdot R_s)}{k_B \cdot T}\right) - \frac{V + I \cdot R_s}{R_p} \tag{2.6}$$

The short-circuit current of a PV cell is defined as the maximum current passing through the PV cell when the voltage of the cell is zero or the cell is short circuited. The short circuit current depends on several factors, such as the number of incident photons, the intensity of the incident light or the PV cell area, the spectrum of the incident light and the collection probability of generated carriers. For an ideal PV cell, the short circuit current is same with the photogenerated current. Anther common used parameter is current density, which is a function of $E_g$ and can be calculated by solar photon flux $\phi$ and electronic charge e [22]:

$$J_{ph} = e \cdot \phi \tag{2.7}$$

The maximum current density of silicon solar cell is around 46 mA/cm$^2$ under an AM1.5D spectrum. Commercially, the short circuit current of a PV cell is around 28 mA/cm$^2$ to 35 mA/cm$^2$ [23].

The open circuit voltage is defined as the maximum voltage of a PV cell when the current of the cell is zero, which is given by [18]

$$V_{oc} = \frac{k_B T}{q} \ln\left(1 + \frac{I_{ph}}{I_o}\right) \tag{2.8}$$

From the equation, the open circuit voltage is a function of photogenerated current and dark current of solar cell which depends on generation recombination current. Large dark current can reduce the signal to noise ratio, so it must be minimized [18]. The open circuit voltage also can be expressed by the carrier concentration [24]:

$$V_{oc} = \frac{k_B T}{q} \ln\left(\frac{\left(N_A + \Delta n\right)\cdot \Delta n}{n_i^2}\right) \tag{2.9}$$

where $\frac{k_B T}{q}$ is the thermal voltage, $n_i$ is the intrinsic carrier concentration, $\Delta n$ is the excess carrier concentration and $N_a$ is the doping concentration.

The I-V characteristic of the solar cell is shown in Figure 12. The maximum power is calculated by:

$$P_m = \mathrm{I_m} \cdot V_m \tag{2.10}$$

and is described by the rectangle within the dashed line in the figure. There is a key factor in evaluating the performance of the PV cell, which is called fill factor (FF). The fill factor is defined as the ratio of the actual maximum power of the solar cell to the product of the open circuit voltage and the short circuit current of a PV cell [18]:

$$FF = \frac{\mathrm{I_m} \cdot V_m}{I_{sc} \cdot V_{oc}} \tag{2.11}$$

High fill factor means that the solar cell has a high equivalent shunt resistance, a low equivalent series resistance, and more electric power generated by the PV cell is transmitted to the external load. The maximum theoretical fill factor can be determined by the expression [21, 25]:

$$FF = \frac{v_{oc} - \ln\left(v_{oc} + 0.72\right)}{v_{oc} + 1} \tag{2.12}$$

where $v_{oc}$ is defined as:

$$v_{oc} = \frac{V_{oc}}{k_B T} \tag{2.13}$$

The power efficiency of a PV cell $\eta$ is defined as ratio of the output electrical power produced by the PV cell to the incident optical power:

$$\eta = \frac{P_{out}}{P_{in}} \times 100\% \tag{2.14}$$

The efficiency can also be expressed with fill factor:

$$\eta = FF \cdot \frac{I_{sc} \cdot V_{oc}}{P_{in}} \tag{2.15}$$

The efficiency of a solar cell depends on different parameters such as the spectrum of the input sunlight, absorption coefficient, carrier lifetime, temperature and the energy band gap of the semiconductor material.

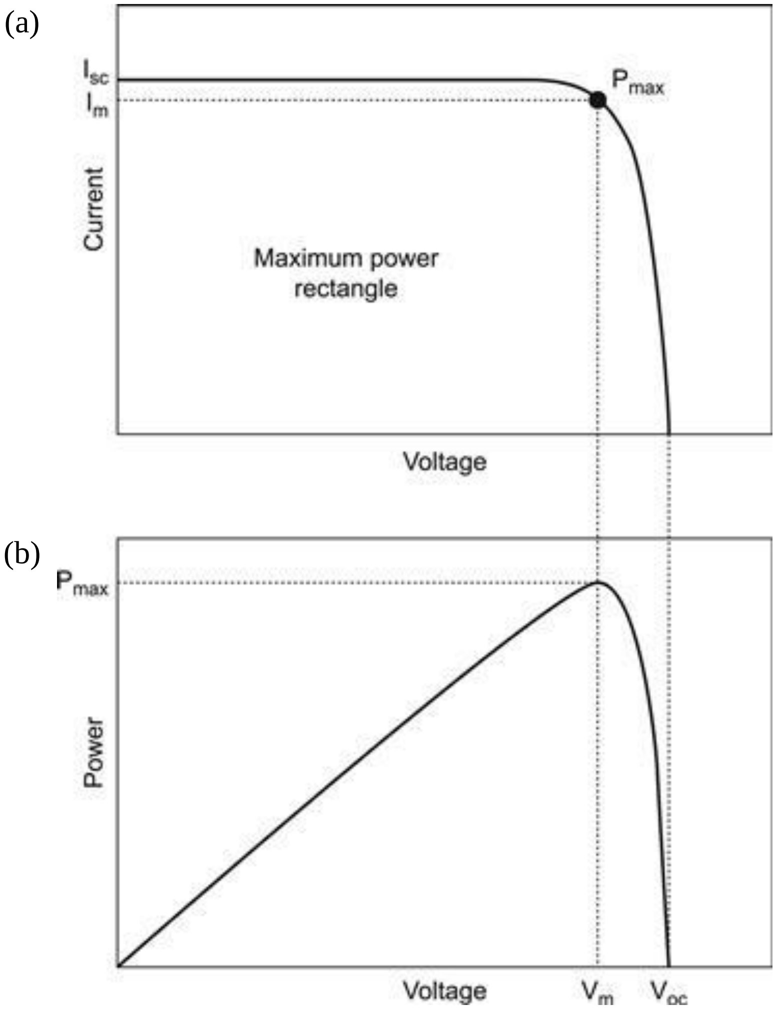

Figure 12. (a) I-V characteristic of a solar cell and (b) the power generated by the cell. Reprint from [21].

## 2.4 Types of solar cell

Silicon solar cell is the first generation PV cell, which is also the most widely used PV cell. Silicon is the second most abundant element in the Earth's crust, which is around 27.7% by weight [26]. Also, silicon is the most popular material for making solar cell, but silicon is not the ideal material for the PV application because of its indirect band gap and low absorption efficiency for solar radiation. The energy band gap of silicon is 1.12 eV, which leads to the cut off wavelength around 1100 nm.

Silicon solar cell can be separated into three categories: single crystalline silicon, multicrystalline silicon, and amorphous silicon. The highest efficiencies of single crystalline, multicrystalline and amorphous silicon solar cells are around 25.6%, 20.8% and 10.2%, respectively, which was obtained under the global AM1.5 spectrum at 25˚C [27]. However, the cost of generating crystalline silicon solar cell is much more expensive than the cost of multicrystalline and amorphous silicon solar cell, since the required purity of silicon is very high, which leads to the complicated fabrication process with high temperature. The cost of multicrystalline and amorphous silicon solar is cheaper than single crystalline silicon solar cell, since they do not request very high purity of the silicon, but the efficiency is lower than single crystalline silicon solar cell.

Due to the fact that silicon supply is abundant in Earth, silicon solar cells have a relatively high efficiency and there is almost no degradation in crystalline silicon, solar cell that is based on crystalline silicon covers more than 80% of today’s PV market and it will continue in the near future. However, because of the complicated fabrication process and the high cost of crystalline silicon solar cell, thin film solar cell and new technology solar cell are growing rapidly. The market share of solar cell materials is shown in Figure 13.

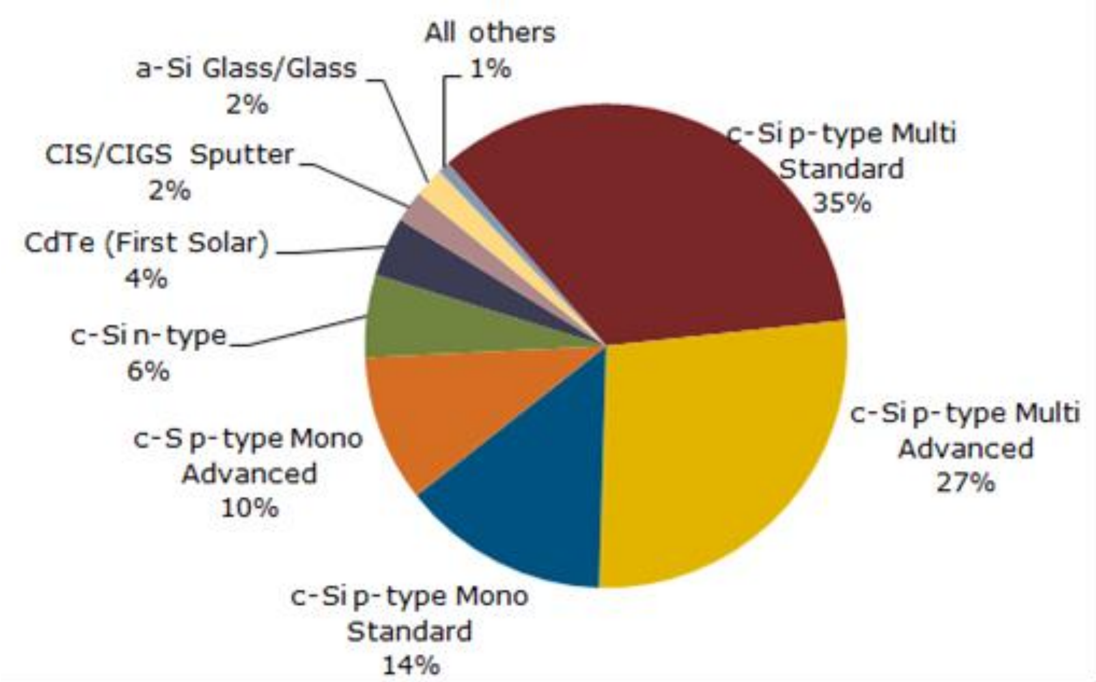

Figure 13. Market share of solar cell production in 2014. Reprint from [28].

Second generation PV cell is called thin film solar cell which is based on cadmium telluride (CdTe), copper indium gallium diselenide (CIGS) and amorphous silicon (a-Si). The main advantage of thin film solar cell is the cost, since the expensive high purity silicon wafer is not required, which accounts for around 50% of total manufacturing cost [29].

The strength of the thin film solar cell based on a-Si is its simple fabrication process by using nontoxic and abundant silicon material and with relatively low temperature, but it has degradation problems and low efficiency which is around 12% [27, 29].

CdTe solar cell can have an efficiency of 21% because of its high absorption coefficient and an ideal direct band gap which is around 1.45 eV [21, 27]. Based on the

Shockley-Queisser limit, the maximum conversion efficiency of a single junction solar cell is around 33% and happens when the band gap is around 1.4 eV [16, 30]. Also, cadmium is abundant in Earth. Figure 14 shows the typical structure of CdTe PV cell which is composed of a glass substrate, ITO/ZnO absorber, CdTe p-n junction and back contact [31]. The main problem of CdTe solar cell is the environment issues since cadmium is toxic and Tellurium is an extremely rare element in Earth.

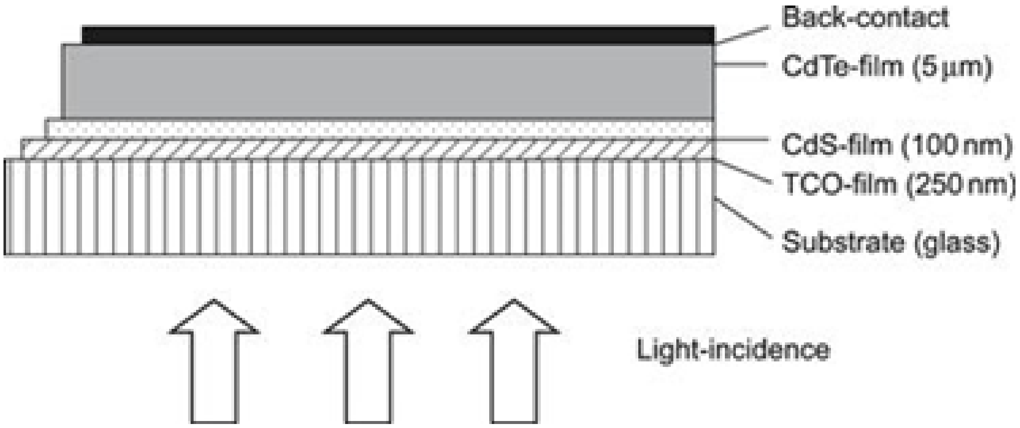

Figure 14. Typical structure of CdTe solar cell. Reprint from [21].

CIGS solar cells are based on materials $CuInSe_2$ and $CuGaSe_2$ which are from I-III-$VI_2$ from the periodic table. Figure 15 shows the structure of a ZnO/CdS/Cu(In,Ga)$Se_2$ thin film PV cell. The maximum efficiency of CIGS is around 21% and the band gap energy is from 1.04 eV in $CuInSe_2$ up to 2.4 eV in $CuGaSe_2$ with modification [21]. The limitation of CIGS solar cell is its low open circuit voltage and material supply since indium and gallium are rare elements.

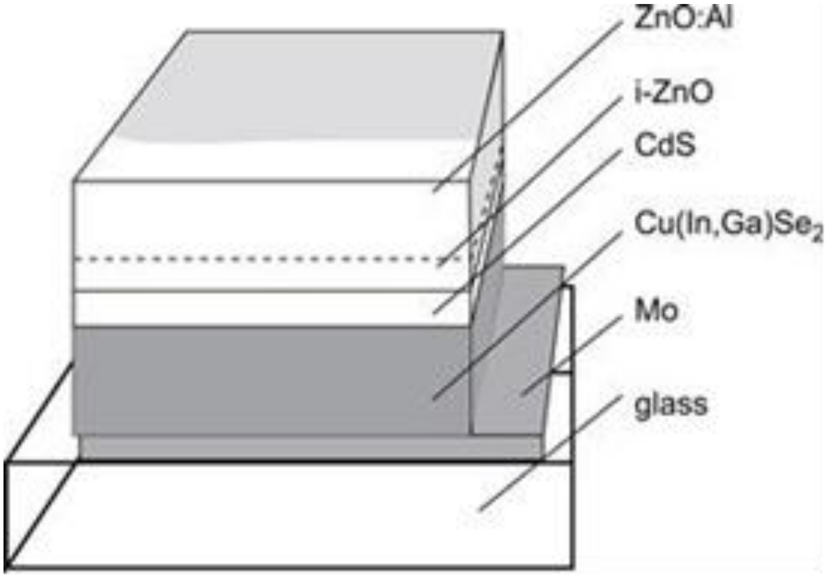

Figure 15 .The structure of a ZnO/CdS/Cu(In,Ga)$Se_2$ thin film PV cell. Reprint from [21].

The third generation solar cell technology includes multi-junction solar cell which is also called tandem cell, organic solar cell and dye-sensitized cell. Both dye-sensitized and organic solar cell are using new technology to generate electrons and current, which is quite different from the first two generation PV cells that are based on p-n junction.

The principle of dye-sensitized solar cells is based on photoelectrochemistry which use the dye to absorb photons and directly inject electrons which are obtained from absorption into semiconductor material such as zinc oxide (ZnO) and titanium dioxide ($TiO_2$) with a wide band gap [16, 21, 29]. The cost of producing dye-sensitized solar cells is lower than the cost of the first two generation PV cell. The highest efficiency of dye-sensitized solar cell is reported around 12% [27]. The main problem of this new technology is the stability and degradation of the cell.

Organic solar cells use organic molecules and conjugated polymers as the active layer to absorb photons, separate electron and holes and transport charges [21]. The advantages of organic solar cell are its mechanical flexibility and very low cost, since the thickness of the cell is far below 1 μm which needs only a small amounts of material [16, 29]. The efficiency of organic solar cell is around 11% [27]. The main challenges for future development of organic solar cell technology are to improve its long term stability, device encapsulation and material degradation. Also, producing a compatible and flexible substrate for organic solar cell is another critical issue for future [21].

## 2.5 Multijunction solar cell

Multijunction (MJ) solar cells are based on semiconductor materials in group III and V from the periodic table, and they have the highest solar cell efficiencies so far. The common materials that are used in MJ cells are gallium indium arsenide (GaInAs), gallium indium phosphide (GaInP), gallium antimonide (GaSb), indium phosphide (InP) and gallium arsenide (GaAs). To achieve high efficiency, MJ solar cells combine several cells or p-n junctions with different band gaps into multijunction structure, which can absorb sunlight in a different part of the solar spectrum. Figure 16 shows the typical triple junction structure of MJ solar cell, which consists of GaInP, GaInAs and Ge from top to the bottom. The top cell is side that points toward the sun. The cells in the multijunction structure are electrically connected in series and assembled with low resistive tunnel diodes. The subcell on the top position has the highest band gap energy, which can absorb photons with the highest energy and shortest wavelength in the solar spectrum. Also, the top subcell transmits photons with the energy that is lower than the energy band gap of the top cell to the cells in lower position, which can absorb the lower energy photons [32]. Thus, the broad solar spectrum is separated into several parts with different wavelength, which is absorbed by subcells with different band gap. Each subcell can absorb photons with the energy that is close to its energy band gap, so that the wide band gap combinations can be realized and thermalisation losses can be reduced [21]. The maximum theoretical efficiency of two cells which are connected in series is reported to be 41.9%, and a efficiency of 50% can be expected if using more cells connected in series [16].

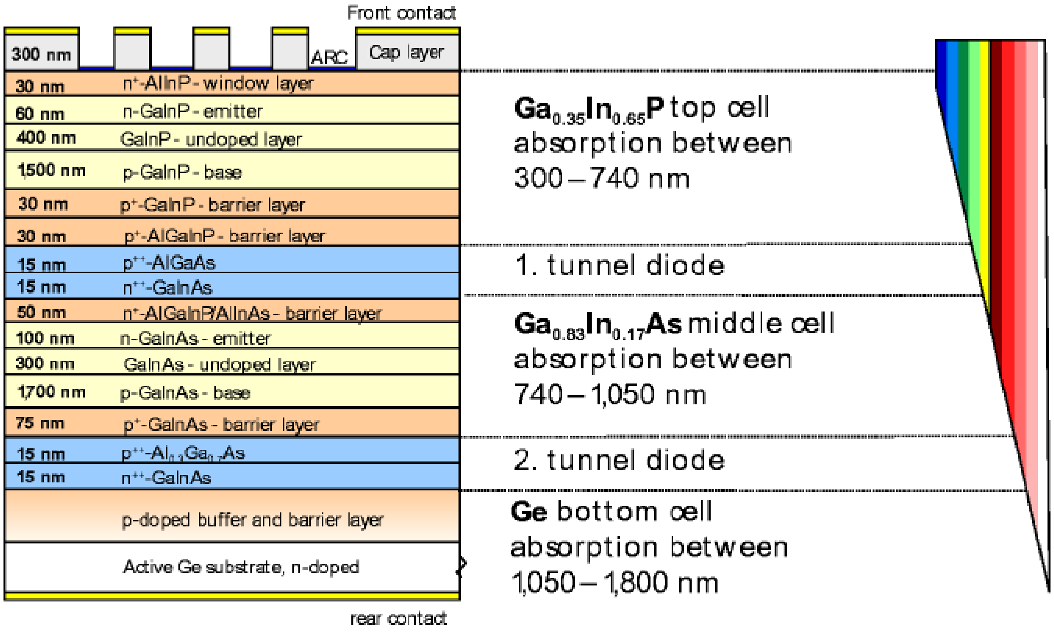

Figure 16. Schematic structure of a typical three junction PV cell with related solar spectrum. Reprint from [16].

The main challenge of MJ solar cell is the material combination to achieve the optimal band gap and current matching of the subcells. In order to grow semiconductor materials with high quality, lattice constant of each material is required to be matched. Figure 17 shows the energy lattice constant and energy band gap for semiconductor materials which are used for MJ cells. Growing semiconductor materials with different lattice constant can have the problem of dislocation, which reduces the quality of the device. Another problem of MJ cell is the current balance of the subcell materials. Since the subcells are connected in series, the total current of the MJ cell is determined by the minimum current generated by the subcell. For an ideal three junction PV cell on Ge, the band gap energy is around 1.7 eV/1.1 eV/0.67 eV from top to Ge substrate, but the real GaInP/GaAs/Ge cell is limited to 1.9 to 1.8 eV/1.4 eV/0.67 eV, which leads to a large current generated by Ge subcell. Since Ge is the lowest band gap in the structure, some of the photons with higher energy can be turned to heat. Since the subcells are connected in series, there are tunnel junctions between subcells. When the light passes through the top subcell to the bottom subcell, the tunnel junctions are required to be highly transparent and electrically conducting. In order to have high transparency, materials that have higher band gap energy than the upper subcell can be used to produce tunnel junction [32].

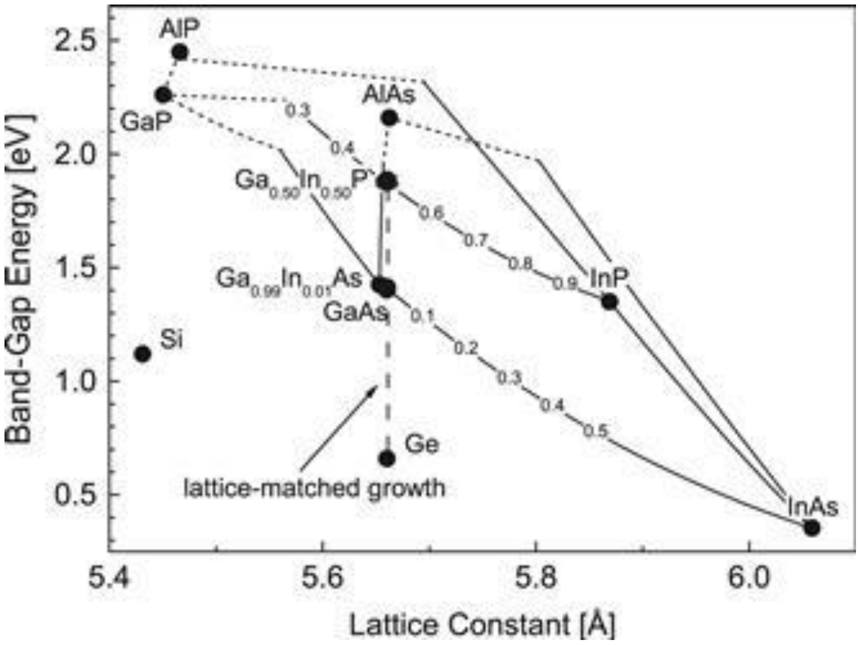

Figure 17. Band gap and lattice constant of semiconductor materials. Reprint from [21].

The maximum efficiency of a triple junction cell which is made of GaInP (1.8-1.9 eV)/GaAs (1,3-1,4 eV)/Ge (0.7eV) is around 41.6% under concentrated sunlight [33], but the device performance of this type of PV cell is limited by the large excess current produced by the Ge bottom junction. To improve the efficiency of the device, dilute nitride semiconductor material GaInNAs or inverted metamorphic GaInAs can be used as the bottom junction instead of Ge, which has an energy band gap of around 1.0 eV and an efficiency of around 44.4% at a concentration ratio of 302 [33-36]. Another method to improve the performance is adding more junctions. Today's champion efficiency of MJ cell is reported to be 44.7% at a concentration of 297x under the AM 1.5D by using GaInP/GaAs//GaInAsP/GaInAs four junction. This type of MJ cell has a band gap energy that is close to the theoretical optimum band gap combination for a four junction cell [33]. Table 2 shows the maximum efficiency of different types of solar cell so far. Concentration ratio can be described using "suns". One sun represents the light intensity of 1000 W/m$^2$. For example, 300 suns means the concentration ratio is 300x.

Table 2. Confirmed solar cell efficiencies [27].

| Classification | Efficiency (%) | Intensity (suns) |
|---|---|---|
| Si (crystalline) | 25.6 ±0.5 | 1 |
| Si (multicrystalline) | 20.8 ±0.6 | 1 |
| Si (amorphous) | 10.2 ±0.3 | 1 |
| GaAs (thin film) | 28.8 ±0.9 | 1 |
| CIGS (cell) | 20.5 ±0.6 | 1 |
| CdTe (cell) | 21.0 ±0.4 | 1 |
| Dye | 11.9 ±0.4 | 1 |
| Organic thin-film | 11.0 ±0.3 | 1 |
| GaInP/GaAs; GaInAsP/GaInAs | 46.0 ±2.2 | 508 |
| GaInP/GaInAs/Ge | 40.4 ±2.8 | 365 |
| GaInP/GaAs//GaInAsP/GaInAs | 44.7 | 297 |

It is critical to know the behavior of PV cells with different cell temperature, since temperature can vary from 288K to 323K in terrestrial applications and go up to higher temperature with concentrator system and space applications [37]. Several reports show that temperature is an important parameter that can have significant impact on PV cell efficiency [37-39]. Increasing the temperature of solar cells can cause increasing photogenerated current and short circuit current, which is mainly due to the increase in absorption coefficient and the decrease in band gap energy [39]. Also, increasing the temperature of PV cells can decrease open circuit voltage, the maximum current and maximum voltage. Figure 18 shows the measurement result from Erdem Cuce et al. [39]. Therefore, the efficiency of PV cells can be reduced with the increase of temperature, which leads to the fact that a cooling system is necessary for the solar cell system to keep it at high efficiency[40].

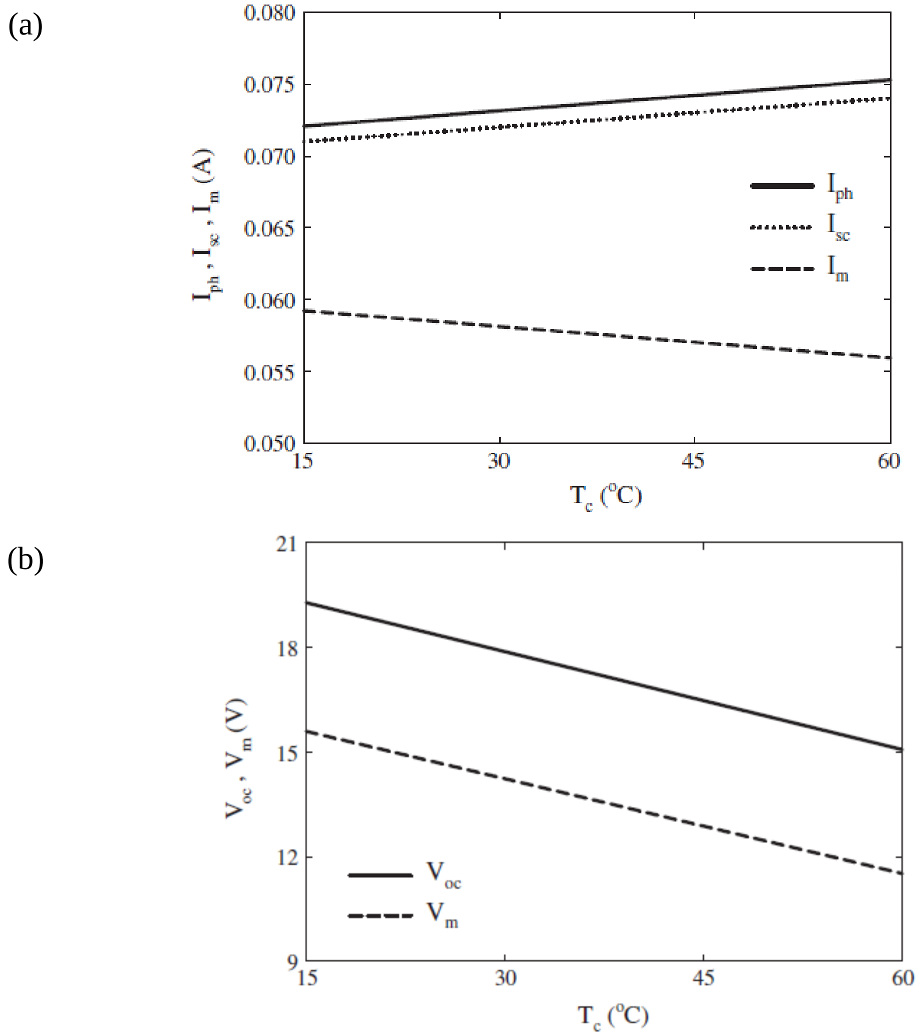

Figure 18. Temperature dependency of current and voltage of polycrystalline silicon solar cell. Reprint from [39].

Dust is another factor that can have impact on solar cell efficiency, since it may reduce the incident light intensity [38]. It is reported that the efficiency of PV cells decreases with the increase of dust deposition density in a linear relationship, because the dust will reduce the short circuit current [41, 42]. The efficiency reduction of silicon solar cells increases to 26% with 22 g/m$^2$ of dust deposition density [41].

## 2.6 The cost of PV cell

In order to have renewable energy replace traditional energy source to generate electricity, the cost is an important factor that has to be taken into consideration. The costs of PV cell materials decrease year by year due to the improvement in cell efficiency by the new technology in materials and manufacturing, and the increasing of PV production [38]. The symbol \$/Wp which is Watts of peak power is often used to represent the cost of PV cells. The cost of polysilicon solar cell and module are around \$0.31 and \$0.72, respectively [43]. Figure 19 shows the average price of PV cell and modules from 2003 to 2012 [44]. Another usually used measure for the cost of energy generating technology is called levelized cost of electricity (LCOE), which is the average cost of the energy. LCOE equals to the cost of installing a system divided by its expected life time energy output. For example, if the cost of an energy system is \$10,000 and the electricity it can provide is 100,000 kWh, the LCOE of this system is \$10,000/100,000 kWh = \$0.10 per kWh. In 2010, it is reported that the LCOE of c-Si solar system and amorphous Si thin film PV cell are around \$0.25-0.65/kWh and \$0.26-0.59/kWh, respectively [45].

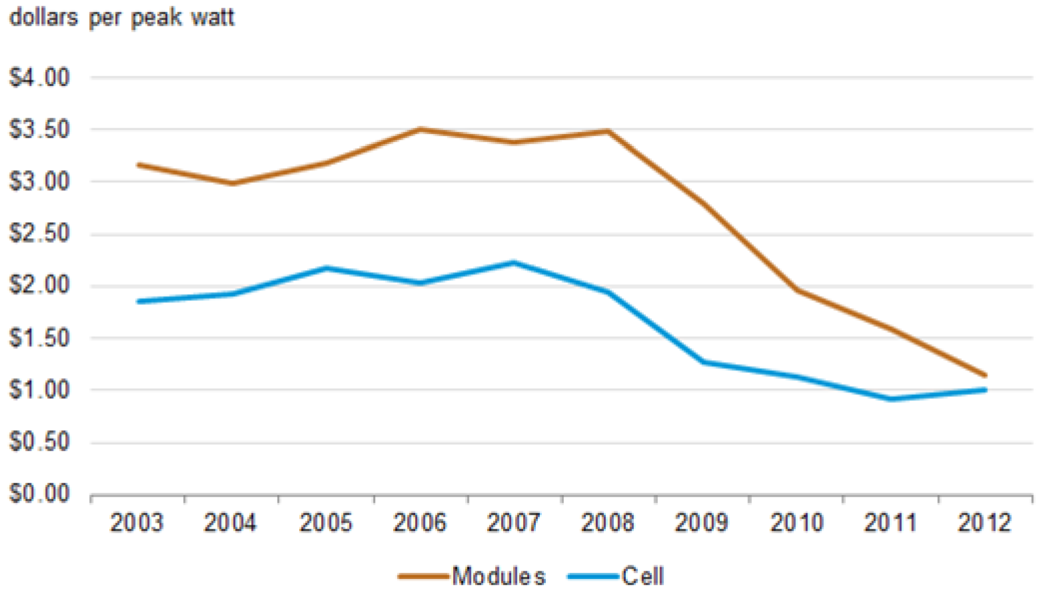

Figure 19. Average price of PV cell and modules from 2003 to 2012. Reprint from [44].

# CHAPTER III

# CONCENTRATING PHOTOVOLTAIC TECHNOLOGY

## 3.1 Overview

The main idea of concentrating photovoltaic (CPV) technology is to use cheaper optics such as lenses and mirrors to focal sunlight onto a tiny area of PV cells. In this case, the required PV cell area is reduced with a given amount collection of incident power. There are several advantages of CPV system. First, the cost of the PV system is reduced by replacing a large area of expensive PV cells with less expensive optical elements, which allows to use the most efficient multijunction tandem designed cells which is also the most expensive cells. Also, the efficiency of solar cells can be significant increased under concentrating system. High efficiency is one of the key point to make CPV more cost competitive with other PV and electricity generation technologies [46]. Figure 20 shows the development of efficiencies of MJ cell, CPV modules and system. Today’s champion efficiency of multijunction cell is around 46% with optical concentrators. Another advantage of CPV system is that it can be made of small high efficient individual cells since it is more difficult to make large area and high efficient cells than small cells.

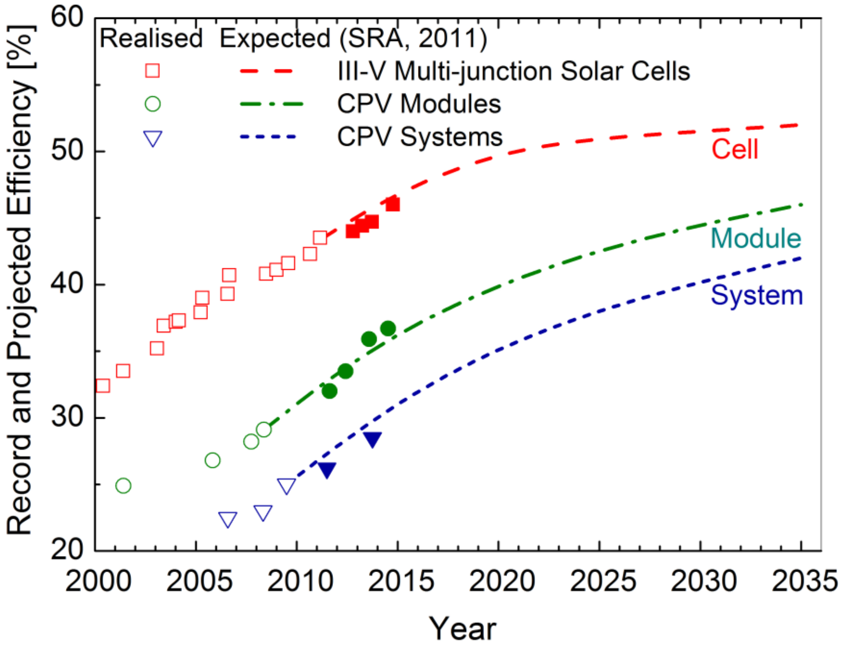

Figure 20. Development of efficiencies of MJ cell, CPV modules and system. Reprint from [46].

However, due to the high concentration ratio, CPV system requires high accurate and reliable tracking systems that track the sun throughout the day and year. Also, the high temperature of PV cells at high concentration is another challenge for CPV technology [47, 48].

### 3.2 Types of concentrator

Based on the primary concentrating elements, CPV system can be divided into two categories: refractive and reflective, which is shown in Figure 21 [49]. Reflective systems usually use reflective lenses or mirrors as the primary concentrator. Refractive systems always use Fresnel lens as the concentrator.

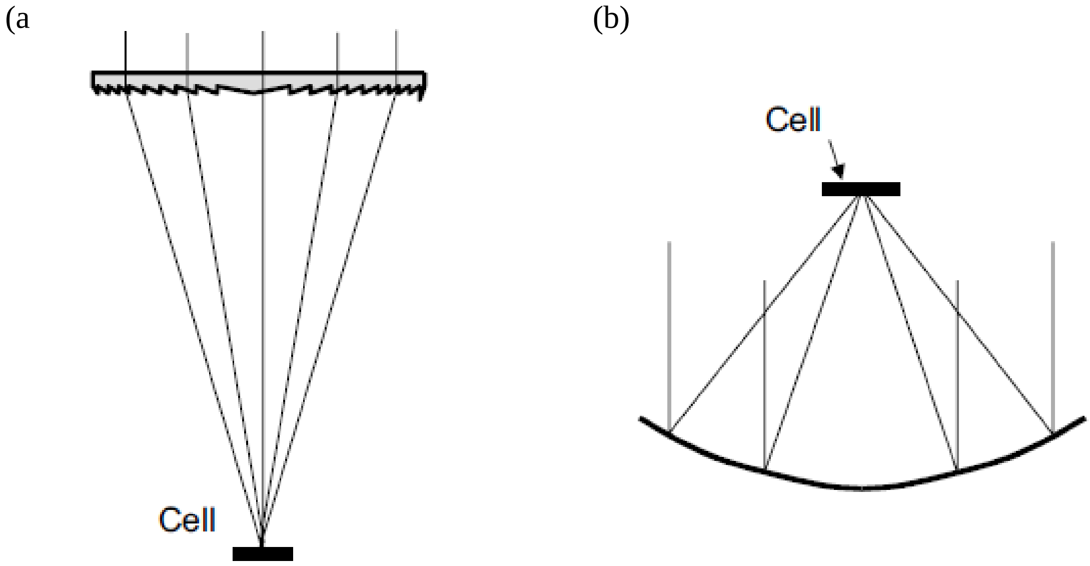

Figure 21. (a) Refractive and (b) reflective concentrators. Reprint from [49].

The reflective surface of reflector always has a shape of a parabola which can have a point focus configuration such as parabolic dish reflector or line focus configuration such as parabolic trough. Another type of reflector is the compound parabolic concentrator (CPC), which can provide the maximum possible concentration for a given maximum acceptance angle. It is also nonimaging concentrator which is not related to the image of the sun. However, CPC needs to be tall and thin to achieve high concentration, which is usually used in low concentration applications or used as a secondary concentrator. Figure 22 shows the structure of parabolic dish, parabolic trough and CPC reflector [47].

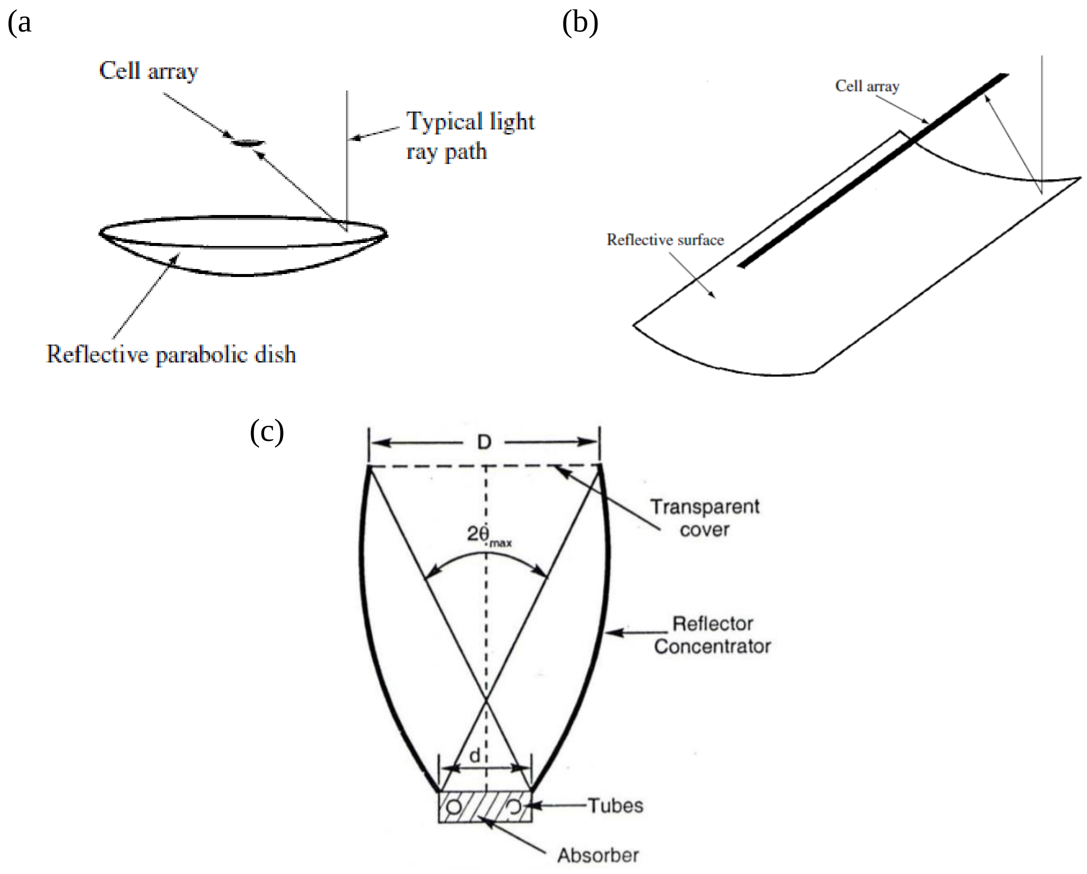

Figure 22. Schematic structure of (a) parabolic dish, (b) parabolic trough and (c) CPC reflector. Reprint from [49].

Refractive system usually use Fresnel lens as the primary concentrator, since it is light weight and cost effective. The surface of a Fresnel lens is actually a chain of prisms which is different with the conventional lens. An example of a typical Fresnel lens is shown in Figure 23. In this case, Fresnel lens can reduce the required material for traditional lens and can be made thinner and lighter. The disadvantage of using Fresnel lens with grooves is the light loss on the draft facet, which is called draft-loss. In order to keep high transmission efficiency, the loss can be minimized by make the facet perfectly vertical [50]. The early Fresnel lenses was made of glass which is highly transparent in visible and infrared region and can be used at high temperatures or for glazing applications. In 1951, the first plastic Fresnel lens was made by Miller et al. [51]. After that, polymethylmethacrylate (PMMA) is used as a suitable material to fabricate Fresnel lens, since it is light weight, low cost in manufacturing, thermally stable up to at least 80˚C and highly transparent in visible region. [47, 52].

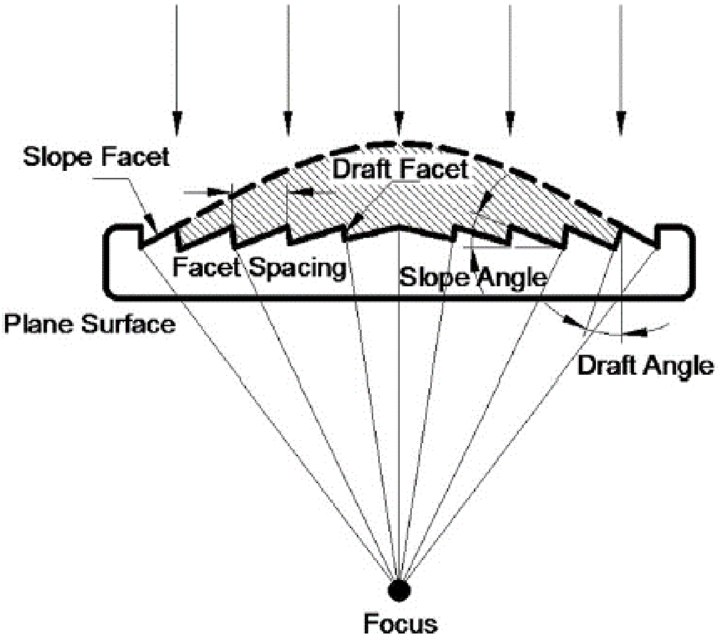

Figure 23. Cross-section of a typical Fresnel lens. Reprint from [53].

Based on different purposes of solar energy applications, Fresnel lens system can be divided into two fields: imaging Fresnel system and nonimaging system. The imaging Fresnel lens can refract the sunlight and form a sun image in the focal plane, which requires accurate two axis tracking system. On the other hand, nonimaging system try to optimize the light radiation transfer from a source to a target, but no attempt to form an image of the source [52]. Nonimaging Fresnel lens can have wide acceptance angle and high tolerance with less precise tracking system, which make it suitable for concentrating solar power technology [53].

### 3.3 Optics of Fresnel lens

Since Fresnel lens has one plat surface and one surface with periodic prism structure, it is important to know the transmission efficiency based on the direction that the Fresnel lens face. The direction of Fresnel can be defined as grooves out and grooves in. A grooves-out lens means the lens facets points to the incident light and a grooves-in lens is the lens that towards the focal point. Figure 24 shows the transmission efficiency based on the facing direction of the grooves [50]. In the figure, collimating means that a point light source is converted to parallel light by the lens and concentrating means the lens focus the light to a point.

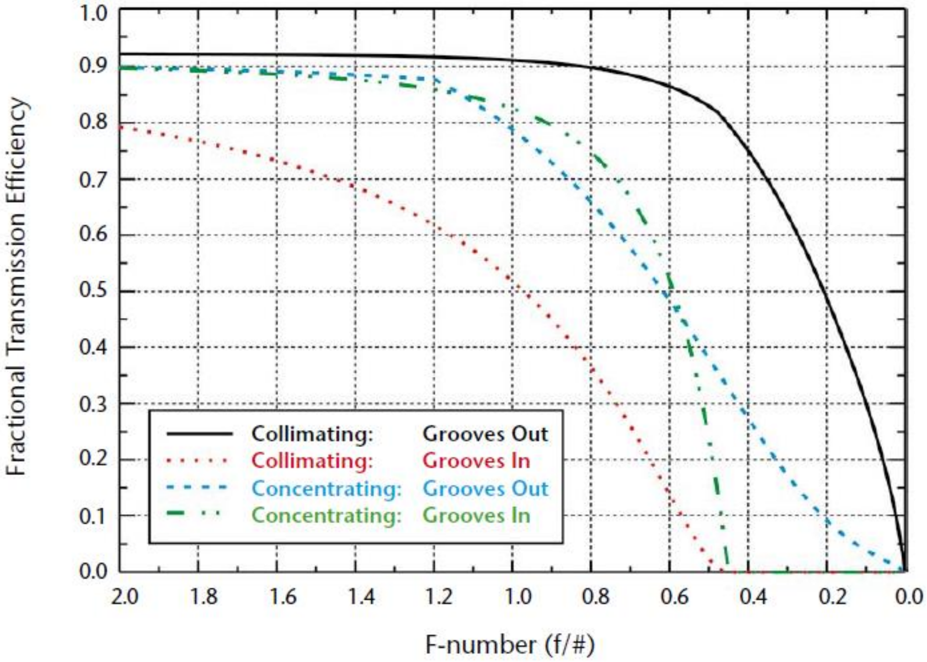

Figure 24. Transmission efficiency of Fresnel verse f-number based on the facing direction of the grooves. Reprint from [50].

The distance between the lens surfaces to the focal plane is called focal length (f). Another usually used parameter which is called f-number (f/# or N) is defined as the ratio of focal length to the clear aperture diameter (D) of the lens, which is given by

$$N = \frac{f}{D} \tag{3.1}$$

The aperture diameter would be the diagonal if the shape of lens is a square. Lens with large f-number can have small convergence cone angle of light rays. Oppositely, lens with small f-number can have large convergence angle, which can reduce the costs of tracking and mechanical support. However, chromatic aberration problem is an issue with a lens at small f-number. Figure 25 shows the relationship between transmission efficiency of lens with f-number. The transmission efficiency is decreased when the f-number is below 1 [53].

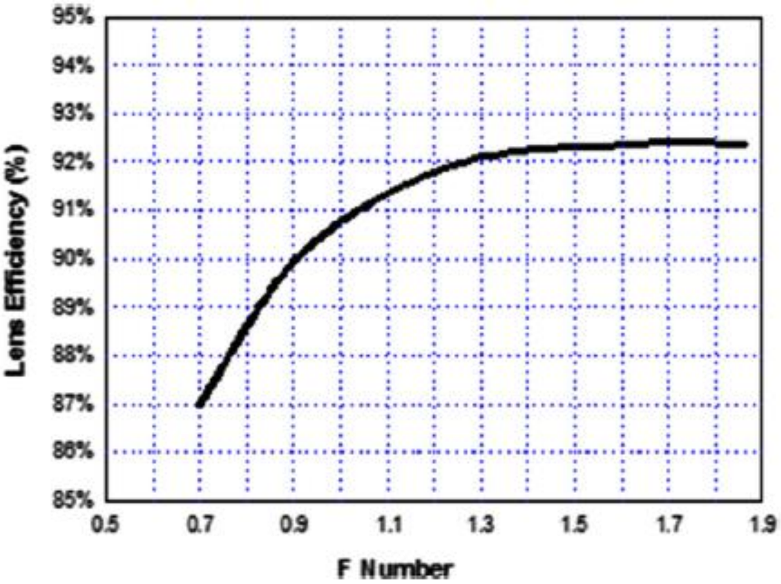

Figure 25. Lens efficiency verse f-number. Reprint from [53].

The main losses of Fresnel lens can be divided into three parts: Fresnel reflection loss, material absorption loss, efficiency loss due to geometric and manufacturing limitations.

Fresnel reflection loss is the transmission loss when the light comes from one medium to another medium with different refractive index. Figure 26 shows the Fresnel loss on the surface between the air and PMMA material based on different incident angle. When the light is normally incident on the Fresnel lens surface, the transmission loss is around 8%. Also, it is reported that the Fresnel loss increases with increasing radial distance [53].

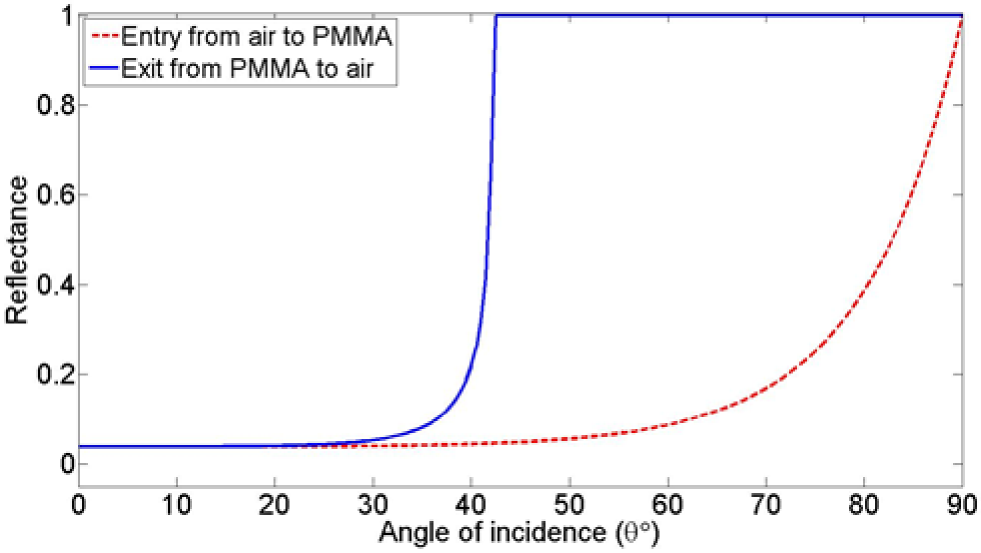

Figure 26. Fresnel loss on the surface between the air (n=1) and PMMA (n=1.49) based on different incident angle.

Fresnel lens is usually made from PMMA which is highly transparent in the wavelength of 400-1000 nm. Most of the solar spectral irradiance is in this visible region. However, PMMA has strong absorption in near infrared and infrared light. Glass is the best material with high transmission from visible to infrared, but the Fresnel lens made from glass is heavy and fragile.

Base on the geometric structure of the Fresnel lens, the ideal designed Fresnel lens has 0˚ draft angle and 0 radius sharp facet corner, which can have the maximum transmission efficiency. However, due to the manufacturing constraint, the transmission efficiency drops around 2% with 4˚ draft angle and around 4% with 10 µm radius facet corner [53].

Another essential loss of Fresnel lens is chromatic dispersion. Since sunlight can be treated as a white light source, when sunlight passes through the prism structure of the Fresnel lens, it can get separated with different wavelength or color, which is called chromatic dispersion. Also, chromatic dispersion increases when the refraction angle increases [54]. Thus, when sunlight passes through the Fresnel lens, the maximum chromatic dispersion happens at the outermost portion of the lens and the minimum chromatic dispersion occurs around the center of the lens. It is possible that some of the rays cannot reach to the focal point when using large size Fresnel lens. In addition, the sunlight is not perfectly parallel, the sun subtends an angle about 0.52˚C to an observer on the Earth [55], which leads to the fact that the light passing through the lens is not perfectly parallel and the outermost portion of the lens has the maximum deviation. Both chromatic dispersion and sunlight deviation can reduce the transmission efficiency and have larger focal spot than desired. Figure 27 shows the schematic of chromatic dispersion and deviation of incident sunlight.

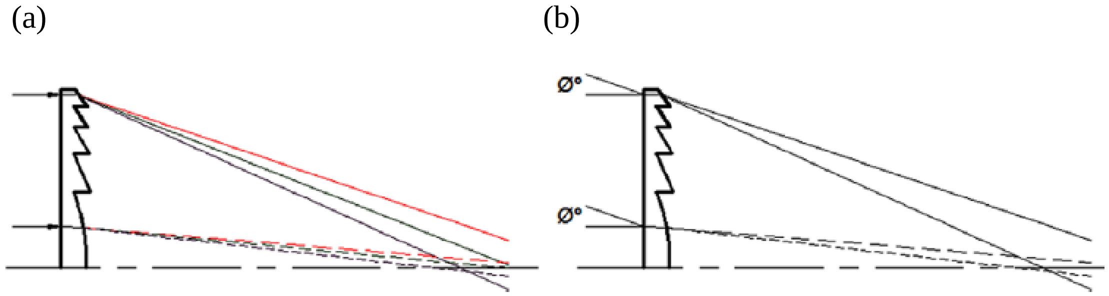

Figure 27. Schematic of chromatic dispersion and deviation of incident sunlight. Reprint from [53].

### 3.4 Basic characteristics of CPV system

In concentrating optics, an important metric is the concentration ratio which usually is defined in two ways: optical concentration ratio $C_o$ and geometric concentration ratio $C_g$ [56, 57]. The geometric concentration ratio $C_g$ is defined as the ratio of collector entry aperture area $A_E$ to receiver area $A_r$:

$$C_g = \frac{A_E}{A_r} \tag{3.2}$$

The optical concentration ratio $C_o$ is defined as the ratio of the light intensity (irradiance) at focal point or receiver $G_r$ surface to the incident light intensity (irradiance) $G_i$ at the surface of optical concentrating element:

$$C_o = \frac{G_r}{G_i} \tag{3.3}$$

Also, optical concentration can be expressed with geometric concentration and optical efficiency:

$$C_o = C_g \times \eta_{opt} \tag{3.4}$$

The optical efficiency of the system is defined as the percentage of light that passes through the optical system and reach the solar cell, which is the output power at the solar cell surface to the incident power of the lens or mirror:

$$\eta_{opt} = \frac{P_{out}}{P_{in}} \tag{3.5}$$

"Suns" is usually used to represent the geometrical concentration ratio: 1000 suns represents the geometrical concentration ratio of 1000. At 1000 W/m$^2$ DNI, the intensity at the focal point would be 1 MW/m$^2$ [57].

The maximum concentration ratio is limited by the incident angle. From the etendue conservation theorem of geometrical optics, the maximum concentration is given by [56, 57]:

$$C_g \le \frac{n^2 \sin^2 \theta_{out}}{\sin^2 \theta_{in}} \tag{3.6}$$

where $\theta_{in}$ is the maximum incident angle which is also the acceptance angle of the concentrator and $\theta_{out}$ is the maximum angle of the light rays at the receiver, as shown in Figure 28.

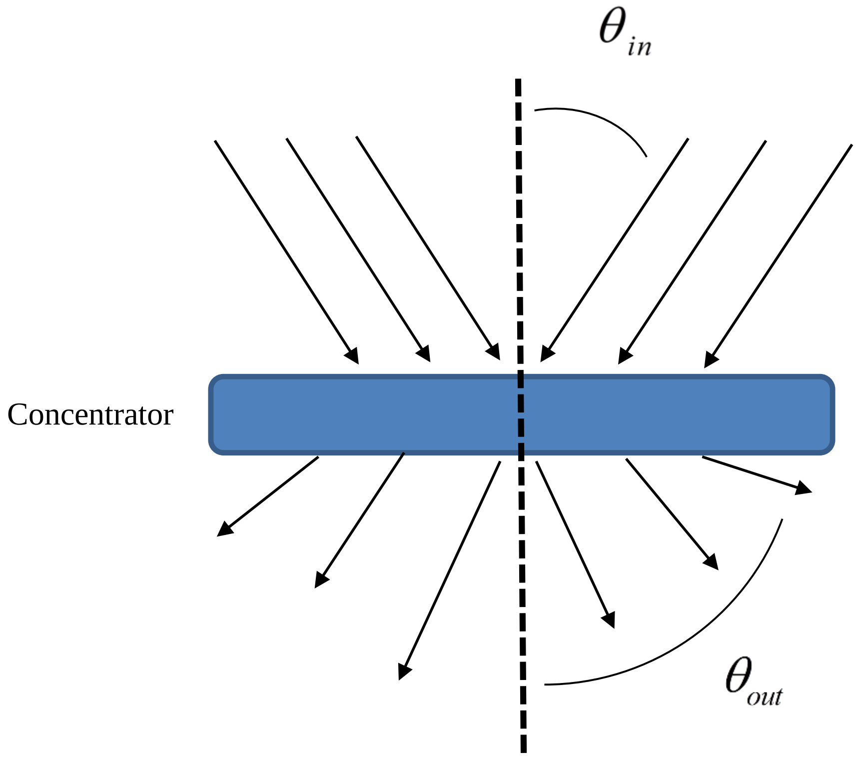

Figure 28. Description of acceptance angle and concentration ratio.

For a solar concentrator with the receiver in air and with the output angle of 90˚, the theoretical maximum geometric concentration becomes as:

$$C_{g\max} = \frac{1}{\sin^2 \theta_{in}} \tag{3.7}$$

From the equation, the geometric concentration mainly depends on the incident angle or acceptance angle of the concentrator. Very high concentration ratio of a concentrator can be made by reducing the acceptance angle, but the collector can only collect a small portion of solar radiation. A wide acceptance angle concentrator can be used for nontracking system but with low concentration ratio. The acceptance angle is typically made close to the angular size of the sun [57].

## 3.5 Types of CPV system

Based on the concentration ratio and light intensity at the solar cell surface, CPV system can be roughly classified to two types: low concentration system (LCPV) which has a concentration ratio less than 300 and high concentration system (HCPV) which has a concentration ratio from 300-1000 [46]. Also, CPV system can be divided into three types: LCPV, HCPV and medium concentration system (MCPV) which has a concentration ratio between LCPV and HCPV [58].

HCPV system is a point focus system which requires a two axis tracking system to track the sun in both azimuth and elevation. The tracking system can be more accurate with smaller acceptance angle [57]. HCPV system with accurate tracking can significant increase the solar cell efficiency. The maximum solar cell efficiency is around 46% using multijunction solar cell under 508 suns. Another advantage of HCPV with MJ cell is that it can be used in hot climates such as desert conditions with daytime temperatures over 50 ˚C, since the efficiency of MJ solar cells does not decline severely at high temperatures [46, 57]. MJ cell can have a coefficient of around -0.07 %/C and conventional c-Si cell have a coefficient of around -0.4 %/C [57].

LCPV can use concentrators with lower concentration ratio such as parabolic troughs, linear Fresnel reflectors and compound parabolic concentrator. Also, LCPV has larger acceptance angle than HCPV system and does not require two-axis tracking system with high accuracy. Thin film and c-Si solar cells can be used with LCPV to make it low cost.

### 3.6 Losses in CPV system

An idea CPV system will have 100% efficiency, however, there are several losses in CPV system. Figure 29 shows the estimated losses in CPV system [58]. As discussed previously, due to the manufacturing limited, Fresnel cannot be made with perfect sharp draft angle and periodic prism structures which leads to the reflection and dispersion loss. HCPV system will have non-uniform illumination on the cell surface which can increase the cell temperature and resistance. Other losses include material absorption, cell stringing and tracking issues. The total efficiency will drop around 40% during these losses in CPV system.

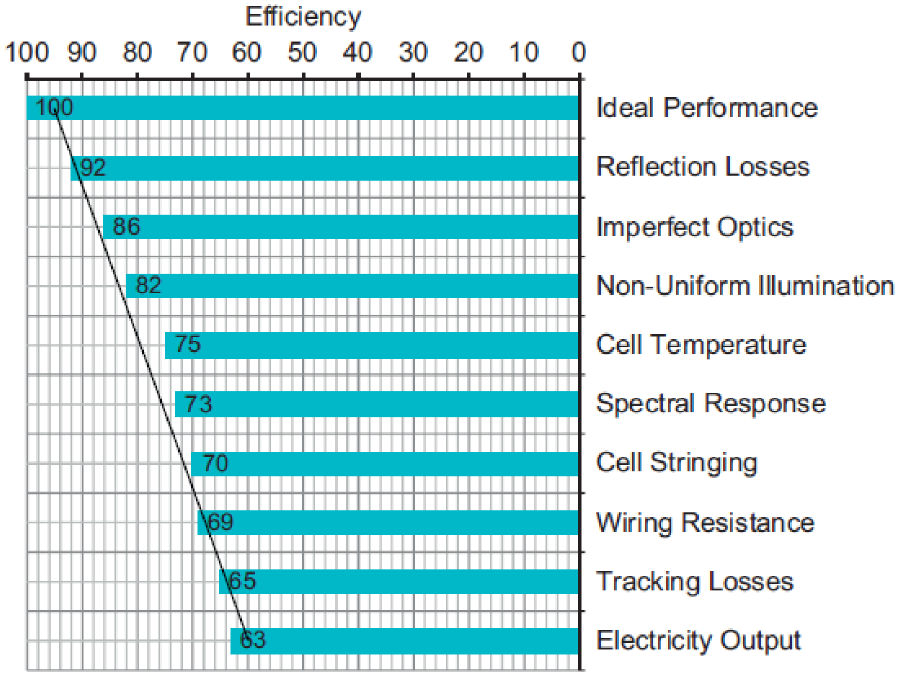

Figure 29. Estimated losses in CPV system. Reprint from [58].

The performance of CPV system reduces initially by Fresnel reflection loss on the surface of concentrators and solar cell. Fresnel reflection loss on the surface between the air and PMMA (n=1.49) is around 4%, which is shown in chapter 3.3. When sunlight passes through a Fresnel lens, both front and back surfaces have Fresnel reflection, which will reduce the transmission to around 92%. Materials with large difference of refractive index will have large Fresnel reflection loss. Antireflection layer can be coated on the front surface where the light will pass through to reduce the Fresnel reflection, but the back surface of a medium still has Fresnel reflection loss.

Ideally, the sunlight can be collected by the concentrator and focused onto a solar cell with uniform flux distribution. However, in real life, some parts of the PV cell get more exposed and some parts get less exposed which leads to the non-uniform illumination on PV cell. Because of the non-uniform irradiance on a PV cell, the temperature of the PV cell is non-uniform, which results in hotspots in some area of the solar cell. For example, this phenomenon of a CPV system using Fresnel lens can be described by Figure 30. Thus, some of the solar energy that collected by the concentrator are converted to heat which reduces the performance of the PV cell. Also, with higher concentration ratio, it is more difficult to have uniform irradiance on solar cell. The performance of the PV cell is limited by the non-uniform temperature on solar cell, which is due to the increasing series resistance.

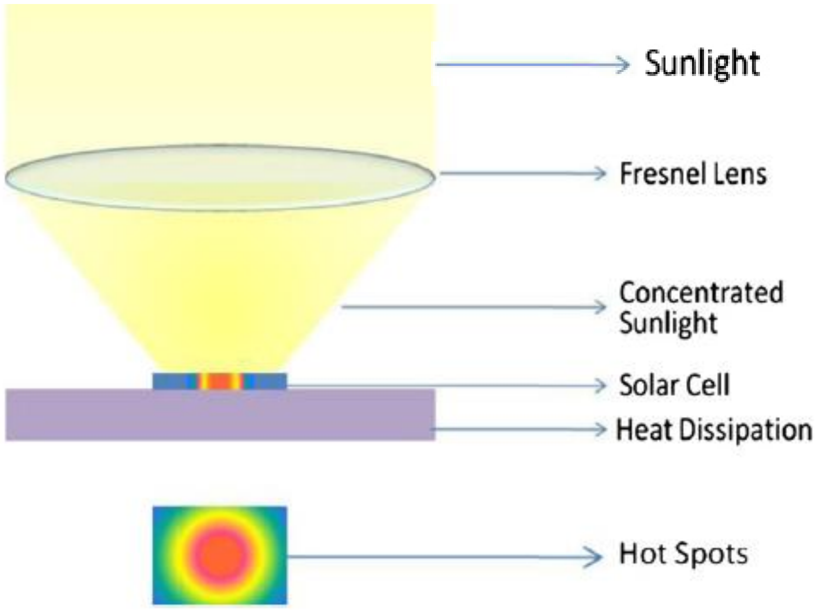

Figure 30. Hot spot on a PV cell because of the non-uniform irradiance in a Fresnel lens system. Reprint from [58].

In a concentrating photovoltaic system, the problem of non-uniform distribution can be separated into two cases: non-uniform irradiance on single cell surface and on a series of cells that are connected together. For non-uniform irradiance on single cell case, some regions of the cell have excessive irradiance which generates more current and heat, and some regions have less irradiance and does not operate. The electrical output power decreases due to the dissipation of power by heat. For the case of a series of cells, the performance of solar cells is limited by shadow effect. The generated current of each cell might be different based the shading area on cell. The current passing through the cells is confined by the cell with the least irradiance, since the current has to be the same in a series of solar cells. The power is dissipated by heat in the cell which has less irradiance [58, 59]. For example, a multijunction solar cell (GaInP/GaAs/Ge) which has an efficiency of 37% has around 63% of the energy that absorbed from the cell dissipated in heat [58, 60].

Non-uniformity of a CPV system can be caused by several factors, such as concentrator optics, shape errors in concentrator profile, tracking errors, misalignment of concentrator, impurities in optical elements, mechanical failures and spectral response of the solar cell [58]. For concentrator optics, non-uniform irradiance happens in all kinds of CPV systems including Fresnel system, CPC system and dish concentrator. Improper tracking can enhance the effect of non-uniform irradiance. Impurities on optical elements can change the property of reflective or refractive concentrators, which non-uniform flux on solar cell [61-67].

Non-uniform illumination on solar cells can have several problems in a CPV system, which include electrical and thermal impact. Some of the thermal effects that are caused by non-uniform illumination can lead to the changes of some electrical parameters, which reduces the system performance.

In a CPV system, non-uniform irradiance can reduce the efficiency and performance of fill factor, open circuit voltage, short circuit current and total generated photocurrent. The open circuit voltage of the solar cell is affected mainly by the cell area and the sheet resistivity [58]. Non-uniform illumination can result in non-uniform charge carrier density and have current passing through the emitter, which reduces the open circuit voltage. Figure 31 shows the experiment result of I-V curve of multijunction PV cells under non-uniform irradiance by R. Herrero et al [68]. The parameter peak-to-average ratio (PAR) which is defined as the peak irradiance to the average irradiance is used to describe the non-uniform light. It is reported that the increasing of non-uniformity will increase the sheet resistance and series resistance, which therefore decreases the fill factor and reduces the PV cell efficiency.

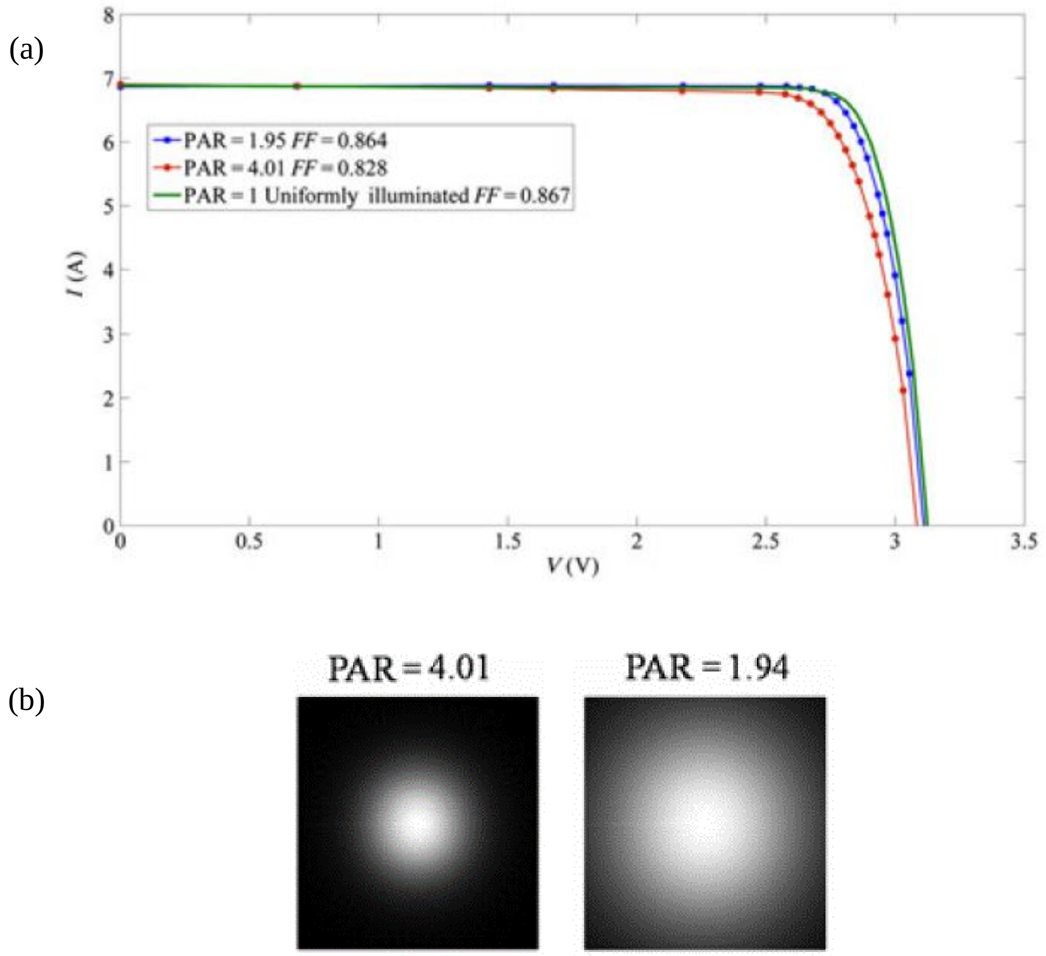

Figure 31.(a) I-V curve of multijunction PV cell under non-uniform irradiance and (b) examples of non-uniform light patterns on solar cells. Reprint from [68].

In thermal area, non-uniformity can lead non-uniform temperature distribution on the cell surface. Also, in MJ solar cell, there is a temperature distribution based on its depth as well as the temperature distribution on its surface, since MJ solar cell can collect different portion of solar spectrum with different layer subcell. Part of absorbed solar energy can convert to electricity, the rest of them will convert to heat. It is critical to know the behavior of PV cell with different temperature and concentration ratio, which is the key point to determine the solar cell performance. In the study of crystalline silicon solar cell, the reverse saturation current is the most sensitive factor to temperature. Also, it is found that series resistance can be increased by almost 65% and shunt resistance can be reduced by over 30% when temperature changes from 25˚C to 70˚C [69]. For multijunction solar cell, the efficiency decreases with increasing temperature and increases with increasing concentration ratio because of the increasing open circuit voltage. With the increase in concentration, it is found that the generated photocurrent and reversed saturated current increase, and series resistance and shunt resistance decrease. With the increase in temperature, the generated photocurrent, reversed saturated current and series resistance increase, and shunt resistance decreases [70]. The temperature dependent coefficient of a triple junction solar cell (InGaP/InGaAs/Ge) is -0.248%/˚C without concentration and -0.098%/ ˚C at a concentration of 200, and other temperature dependent factors are shown in Figure 32 [71]. Therefore, CPV system has more benefit at high temperature.

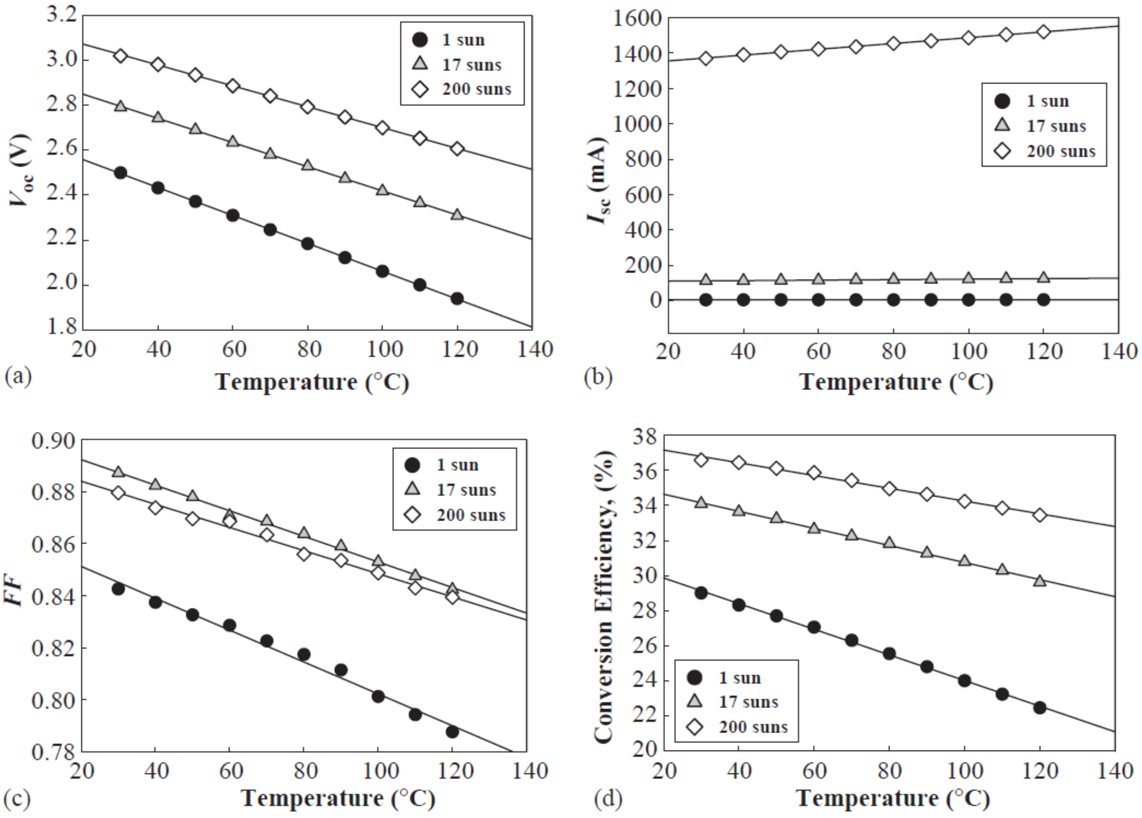

Figure 32. Temperature dependence of (a) open circuit voltage, (b) short circuit current, (c) fill factor and (d) efficiency of InGaP/InGaAs/Ge PV cell. Reprint from [71].

# CHAPTER IV

# INTEGRATED PHOTONICS

## 4.1 Overview

The basic idea of integrated photonics is to integrate various optical and photonic devices on a common planar substrate. The key component of integrated photonic is optical waveguide. The optical signals can be guided, coupled and split by optical waveguide. Thus, optical waveguide can be combined with other technologies, such as non-linear optics, optoelectronics and other photonic technologies (Figure 33) [72].

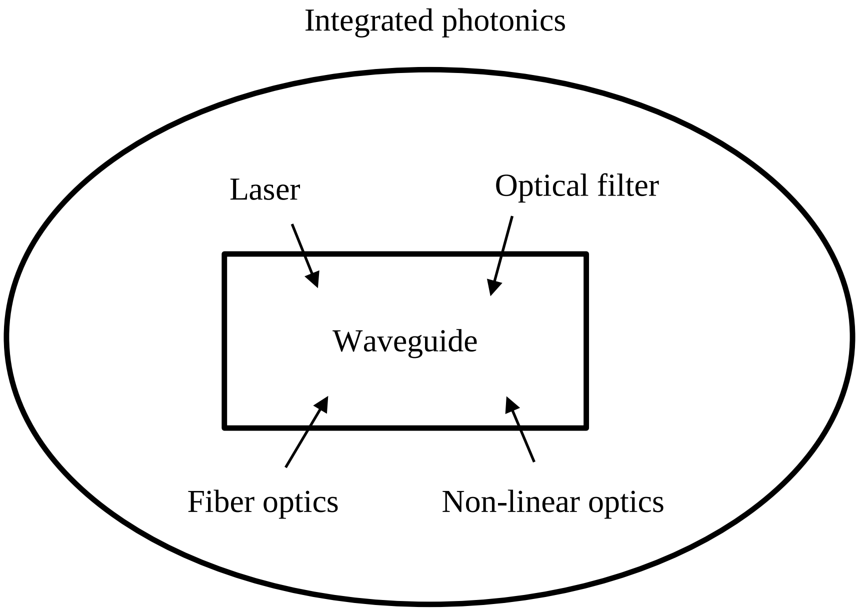

Figure 33. Integrated photonics: combining waveguide technology to several other technologies.

In 1960, S. E. Miller introduced planar optical circuit technology to the world, which was the first time to use the term “integrated photonics” [72]. The goal of integrated photonics is to use of optical technology or photons to create an integrated optical circuit which is similar to the integrated electronic circuit.

The advantage of using integrated photonic circuit instead of traditional electrical circuit is the high frequency of light which can have large bandwidth and transmit a large amount of information. When an electrical signal with high frequency propagates through a conductor, the conductor will have large impedance which leads to a high attenuation. At a transmission rate of around 100 MHz, the attenuation of a coaxial cable is around 5 dB/km [72], which can only be used in applications with short distances. On the other hand, optical signal can propagate in a non-conducting dielectric media with a wavelength in transparent window of the media material. The common used transparent window in optical communication is in the visible and near-infrared range, in which the frequency is $10^6$ times larger than the frequency used in electrical signal. In addition, since the wavelength range used in optical signal is 0.5-2 μm, it allows to use the waveguide with a dimension of micro level to confine the light.

The common used waveguide can be separated into three categories: planar waveguide, channel waveguide and optical fiber, as shown in Figure 34. The channel waveguide is the best choice for integrated optical devices [72]. In order to confine the light in the waveguide, the refractive index of the channel is larger than that of the substrate and upper medium. Integrated optical circuits with channel waveguides is also called planar lightwave circuits (PLC) [72].

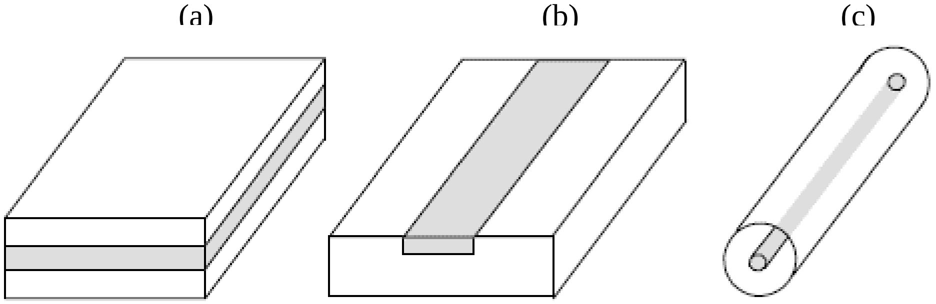

Figure 34. Common used waveguide: (a) planar waveguide, (b) channel waveguide and (c) optical fiber. Reprint from [72].

### 4.2 Electromagnetic theory of light

Light is the flow of electromagnetic (EM) radiation which propagates through free space or through a medium in the form of electrical field and the magnetic field. Both electrical filed and magnetic field depend on the position and time. The electrical field and magnetic field in free space can be given by Maxwell's equation [72]:

$$\nabla \cdot E = 0 \tag{4.1}$$

$$\nabla \cdot H = 0 \tag{4.2}$$

$$\nabla \times E = -\mu_0 \frac{\partial H}{\partial t} \tag{4.3}$$

$$\nabla \times H = \varepsilon_0 \frac{\partial E}{\partial t} \tag{4.4}$$

where $E(r,t)$ is the electric field, $H(r,t)$ is the magnetic field, $\mu_0$ is the magnetic permeability of free space which is $4\pi \times 10^{-7}$ $\mathrm{mkgs^{-2}A^{-2}}$, $\varepsilon_0$ is the dielectric permittivity of free space which is $8.85 \times 10^{-12}$ $m^{-3}kg^{-1}s^{4}A2$. Maxwell’s equations in a material medium is expressed as:

$$\nabla \cdot D = \rho \tag{4.5}$$

$$\nabla \cdot B = 0 \tag{4.6}$$

$$\nabla \times E = -\frac{\partial B}{\partial t} \tag{4.7}$$

$$\nabla \times H = J + \frac{\partial D}{\partial t} \tag{4.8}$$

where $D(r,t)$ is the electric displacement vector, $B(r,t)$ is the magnetic flux density vector, $\rho(r,t)$ is the charge density and $J(r,t)$ is the current density vector. The relationships between the vector $D(r,t)$ and $E(r,t)$, $J(r,t)$ and $E(r,t)$, and $H(r,t)$ and $B(r,t)$ are called constitutive relations which are given by:

$$D = \varepsilon E \tag{4.9}$$

$$B = \mu H \tag{4.10}$$

$$J = \sigma E \tag{4.11}$$

where $\mu$ is the magnetic permeability, $\varepsilon$ is the dielectric permittivity and $\sigma$ is the conductivity of the medium. The wave equations are obtained by combining Maxwell’s equation, which can be expressed as:

$$\nabla^2 \cdot E = \mu\sigma \frac{\partial E}{\partial t} + \mu\varepsilon \frac{\partial^2 E}{\partial^2 t} \tag{4.12}$$

$$\nabla^2 \cdot H = \mu\sigma \frac{\partial H}{\partial t} + \mu\varepsilon \frac{\partial^2 H}{\partial^2 t} \tag{4.13}$$

In a perfect dielectric medium, the conductivity $\sigma$ is 0. The electrical field of an incident wave is given by:

$$\vec{E}_i = \vec{E}_{io} \exp i\left(nkr - \omega t\right) \tag{4.14}$$

where k is the wave vector and $\omega$ is the angular frequency. The speed of light in free space and in a medium are given by:

$$c = \frac{1}{\sqrt{\mu_0 \varepsilon_0}} = 2.99792458 \times 10^8 m/s \tag{4.15}$$

$$v = \frac{1}{\sqrt{\mu \varepsilon}} = \frac{c}{n} \tag{4.16}$$

The refractive index n is related to the optical constant of the medium and the dielectric permittivity and the magnetic permeability of the free space, which is given by:

$$n = \sqrt{\frac{\mu \varepsilon}{\mu_0 \varepsilon_0}} \approx \sqrt{\frac{\varepsilon}{\varepsilon_0}} = \sqrt{\varepsilon_r} \tag{4.17}$$

where $\varepsilon_r$ is called dielectric constant.

## 4.3 Optic waveguide

The basic idea in optical integrated circuits is the use of waveguide to confine the light. Light can propagate in a medium with higher refractive index than that of surrounded medium and light cannot escape from this medium due to the total internal reflection, which is shown in Figure 35 [73]. From the Snell's law, the relationship between the incident angle and refraction angle is given by:

$$n_1 \cdot \sin\theta_1 = n_2 \cdot \sin\theta_2 \tag{4.18}$$

where $\theta_1$ is the angle of incidence and $\theta_1$ is the angle of refraction. If the refractive index $n_1$ is larger than $n_2$ and the incident angle is larger than the critical angle, the total internal reflection occurs. The critical angle can be calculated by:

$$\theta_c = \arcsin\left(\frac{n_2}{n_1}\right) \tag{4.19}$$

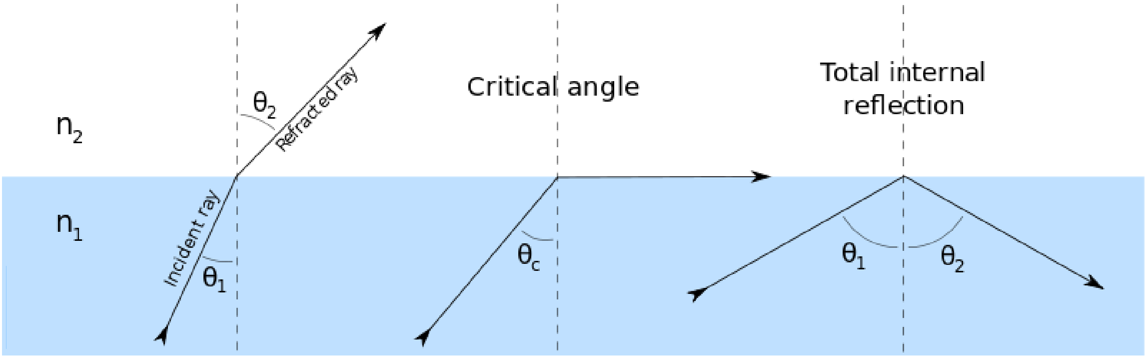

Figure 35. Refraction of light and total internal reflection. Reprint from [73].

When the light propagates in an absorption medium, the refractive index of the medium material is given by

$$n_c = n - i\kappa \tag{4.20}$$

where $n_c$ is called the complex refractive index, n is the real refractive index and $\kappa$ is called the absorption index. The attenuation or loss in waveguide can be divided into three different mechanisms: scattering, absorption and radiation loss. Scattering loss is mainly due to the imperfections such as voids, contaminant atoms and crystalline defects

[74]. Absorption loss is important in semiconductor materials. Radiation loss happens when waveguides are bent.

Optical loss can be described by the attenuation coefficient or absorption coefficient $\alpha$ which is given by [74]:

$$I(z) = I_0 e^{-\alpha z} \tag{4.21}$$

where $I_0$ is the intensity at the position z=0. The unit of $\alpha$ is cm-1. Optical loss is also use dB/cm to determine the attention, which is given by:

$$Loss(dB) = 10\log_{10}\left(\frac{I_0}{I}\right) = 4.3 \cdot \alpha \cdot d \tag{4.22}$$

where d is the length of the waveguide.

### 4.4 Measurement of waveguide losses

One of the simplest method to determine the loss of the waveguide is called end-coupling method or end-fire coupling, which is shown in Figure 36. In this method, the light at the certain wavelength is focused onto a polished face of a waveguide sample and then is coupled to a detector which can measure the total power transmitted. In order to measure the waveguide loss accurately, this method is usually repeated several times with different length of the waveguide sample. The waveguide can be shortened by cleaving, cutting and polishing. A good polishing can reduce the coupling loss of the waveguide. For example, a waveguide sample is shortened five times and can be measured five times. Based on the length of waveguide and the measured power at each length, the loss at each waveguide length can be calculated and the loss data can be drawn in a straight line based on different length of waveguide. The slop of the line represents the propagation loss which can be described as [75]:

$$\alpha = \frac{\ln\left(P_0 / P_1\right)}{L_0 - L_1} \tag{4.23}$$

where $L_0$, $L_1$ are two different lengths of the waveguide, and $P_0$, $P_1$ are transmitted powers of two different lengths of the waveguide. Also, in the graph of loss versus length of the waveguide, the intersection with y axis represents the coupling loss of the waveguide.

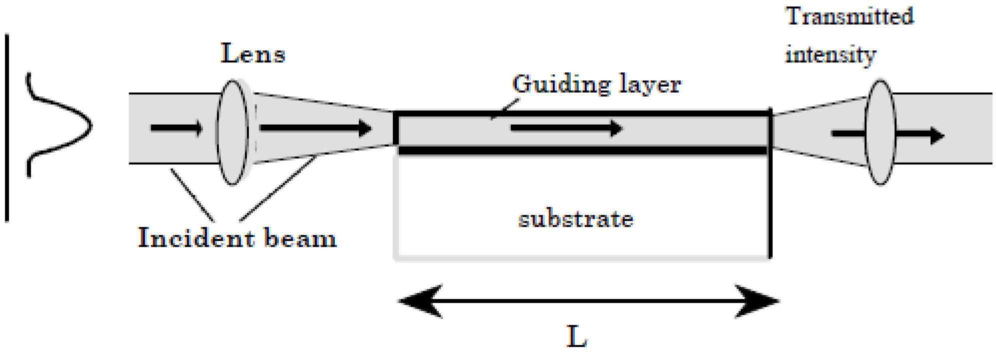

Figure 36. Experiment setup for waveguide loss measurement by the end-coupling method. Reprint from [75].

The accuracy of this method depends on the alignment and polishing which are two important factors to this method. Since the waveguide is required to be cut for each measurement, it is critical to keep the alignment and polishing quality in consistent. Otherwise, the data points will be scattered and it is difficult to obtain accurate slop of the loss versus length curve [74].

# CHAPTER V

# DESIGN OF LENS-TO-CHANNEL WAVEGUIDING CONCENTRATOR SYSTEM

## 5.1 Overview

A traditional CPV system use optical element to concentrate the sunlight directly onto a PV cell. At this point, it may have the problems of the high temperature and non-uniform illumination on the PV cell at high concentration ratio, which can reduce the performance of the PV cell. Due to these disadvantages of conventional CPV system, planar waveguides which are used as the secondary optics have been developed for CPV system since 2010 [76-81]. The advantage of the use of the waveguides as the secondary optics is that it can provide uniform illumination on PV cell and may have additional concentration.

## 5.2 Structure of lens-to-channel waveguiding concentrator system

The designed lens-to-channel waveguiding concentrator contains a lens array which acts as the primary concentrator, channel waveguides and MJ cells, as shown in Figure 37 [82, 83]. Compared with the single Fresnel lens, the use of a lens array as the primary concentrator can not only collect a large amount of sunlight, but also reduce the thickness of the whole system. For example, a Fresnel lens with a dimension of 1 m × 1 m can collect 1000 W of sunlight under normal DNI. If the f number is 1, the total thickness of the system is at least 1 m. However, if using a lens array instead of the single lens, the thickness of the system can be significantly reduced. Consider that if the dimension of each lens is 1 cm × 1 cm and the dimension of the lens array is 1 m × 1 m, the total sunlight power collected by the lens array is the same with the single lens, but the total thickness can be reduced to 1 cm if the lens array have a f number of 1.

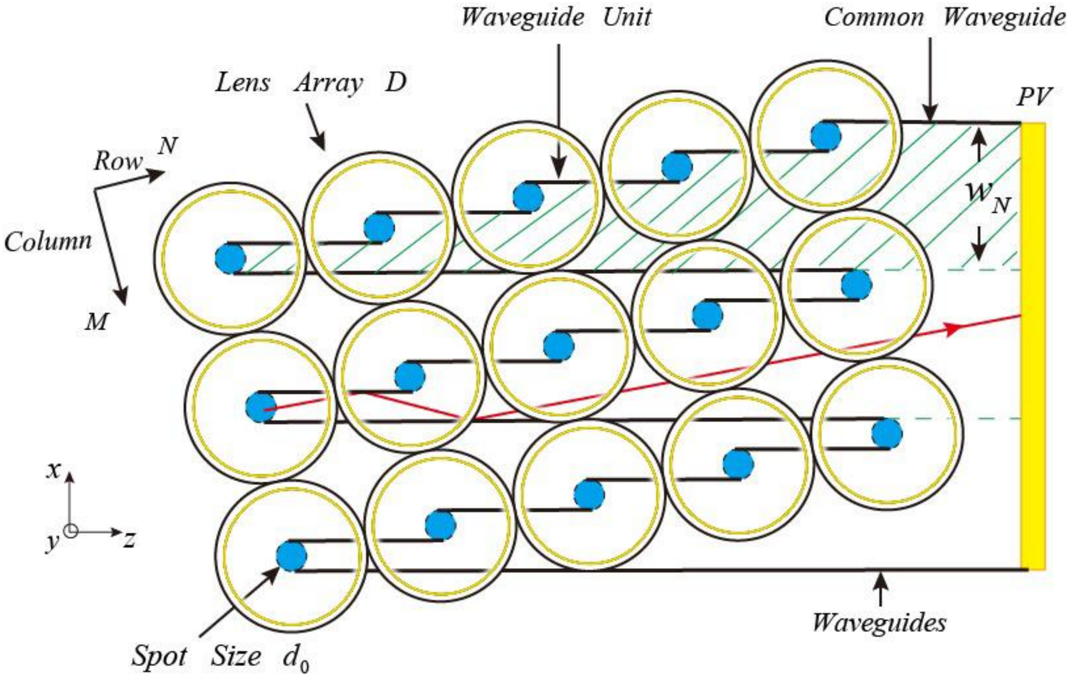

Figure 37. The top side of the lens-to-channel waveguiding concentrator system. Reprint from [82, 83].

In the designed CPV system, the sunlight can be absorbed by a lens array and concentrated onto the waveguide by a 45° coupler that is made in the waveguide. The 45° coupler is positioned at the focal point of each lens. The collected sunlight can propagate by total internal reflection (TIR) in the waveguide and hit the PV cell at the end of the waveguide.

In Figure 37, a lens array can have M x N lenses, where M can be any number and N is given by:

$$N = \sqrt{\frac{D^2}{w^2} - 1} \tag{5.1}$$

where w is the width of the waveguide and D is the diameter of the lens. In order to achieve the maximum concentration, the width of the waveguide is designed as the same size as the spot size $d_0$ of each lens, and the minimum thickness of waveguide is the same with the spot size. Therefore, the geometric concentration of the lens can be expressed as:

$$C_l = \frac{M \times N \times D^2}{M \times N \times w \times t} = \frac{D^2}{w \times t} = \frac{D^2}{{d_0}^2} \tag{5.2}$$

where t is the thickness of the waveguide. Also, the waveguides can be tapered to provide additional concentration, which is shown in Figure 38. The total geometric concentration becomes as:

$$C = C_l \times C_w \tag{5.3}$$

where $C_w$ is the concentration of the waveguide and can be expressed as:

$$C_w = \frac{W}{W - 2 \cdot l \cdot \tan \sigma} \tag{5.4}$$

where W is the total width of the waveguide array, l is the length of the tapered waveguide and $\sigma$ is the tapered angle.

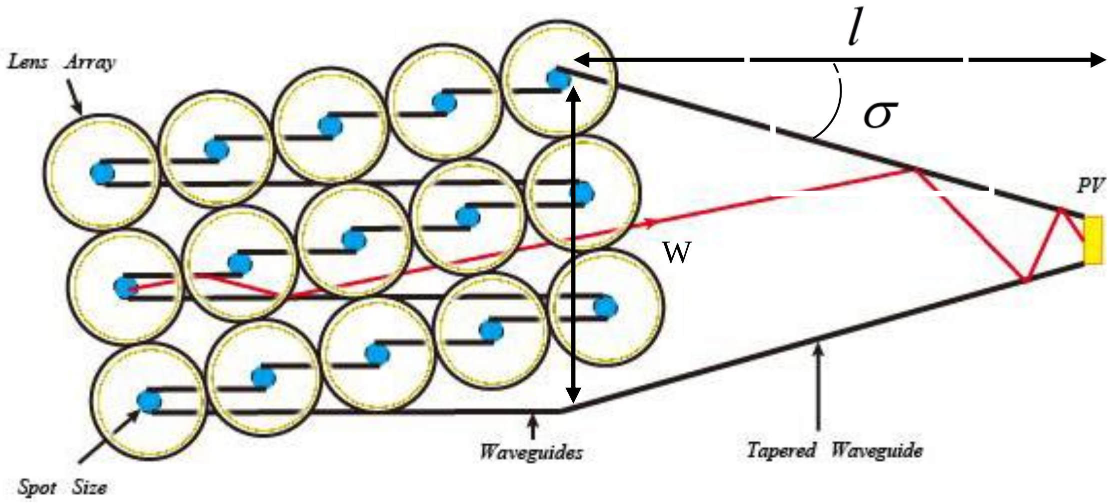

Figure 38. The schematic structure of tapered waveguide concentrator.

Since the maximum geometric concentration of the lens depends on the diameter of the lens and spot size at the focal point. It is important to know the factors that can have impact on the spot size. The spot size d can be described with focal length of the lens and the incident angle, which is shown as:

$$d = 2 \cdot f \cdot \tan\delta \tag{5.5}$$

where f is the focal length of the lens and $\delta$ is the half angle of the incident light. The geometric concentration ratio of the lens becomes as:

$$C_l = \left(\frac{D}{d}\right)^2 = \frac{1}{\left[2\left(f / D\right)\tan\delta\right]^2} \tag{5.6}$$

where $f / D$ is the f number of the lens. The maximum angle after the lens or the marginal ray angle can be calculated by:

$$\theta_M = \arctan\left[\tan\delta + \frac{1}{2(f/D)}\right] \tag{5.7}$$

which is shown in Figure 39. Therefore, the maximum of the marginal ray angle is determined by the maximum half angle of the incident light and the f number of the lens.

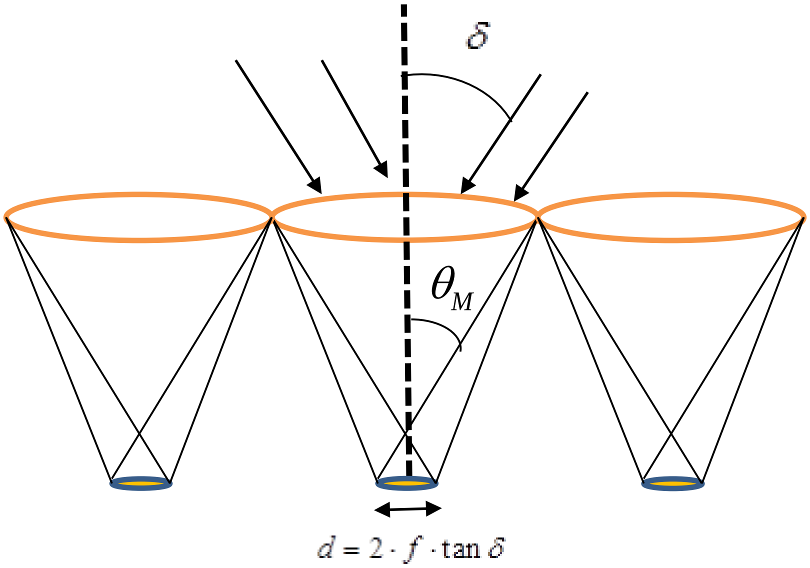

Figure 39. The relationship between the spot size, the incident angle and the marginal ray angle.

### 5.3 Simulaton and discussion

The use of waveguide as the secondary optical element can provide uniform illumination to the solar cell. Also, using the tapered waveguide instead of straight waveguide can have additional concentration. The uniform output at the end of waveguide is shown in Figure 40. To evaluate the importance of having a uniform output, the peak-to-average ratio (PAR) is defined. As discussed previously, the fill factor for MJ cells under uniform illumination (PAR = 1) is 0.867, but it reduces to 0.828 for PAR=4.01 [68]. The efficiency of the MJPV cell will decrease 4.5% which translates to a 2% degradation.

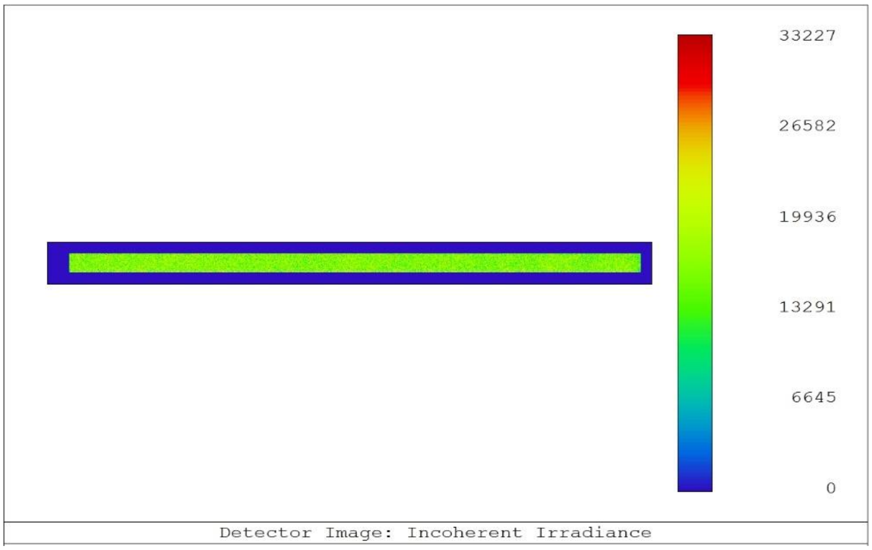

Figure 40. Simulation result of the intensity distribution at the waveguide output.

Material absorption losses for waveguides and lens are critical for the designed system. Table 3 and Table 4 summarize the spectral loss for a three junction PV cell and a four junction PV cell, respectively. The simulation compare the spectral loss of a 10 cm-long waveguide made from PMMA and low OH glass, and 3 mm thick Fresnel lens made from PMMA. The AM1.5 direct spectrum is used in the simulation. The relative power and photon flux in each sub-band for a three junction PV cell and a four junction

PV cell is calculated. The average transmission is calculated in each band as well as the ratio of output to input photon flux. For silica, the transmission is greater than 99.5% for both three junction and four junction PV cell, but the short wavelength band sees more loss compared to the other bands. Due to the absorption, PMMA material has a transmission of above 80% in visible region and 50% or less in near infrared region. For four junction PV cell, the transmission of PMMA waveguide in the bottom cell is around 15%, which may have a significant impact on the current generation of the cell and the cell efficiency, since the cell current is limited by the minimum current generated from the subcell. The thickness of the Fresnel lens is assumed to be 3 mm in the simulation. The transmission of PMMA lens is above 99% in the visible region.

Table 3. Spectral loss calculation for three junction PV cell

| | BB | SR1 | SR2 | SR3 |
|---|---|---|---|---|
| | AM1.5D | InGaP | GaAs | InGaAsNSb |
| Wavelength (nm) | 280-4000 nm | 280-655 nm | 656nm-880nm | 881-1240nm |
| Input power (W/m$^2$) | 887.65 | 381.91 | 229.57 | 176.92 |
| %Power-Relative to BB | 88.8% | 43.0% | 25.9% | 19.9% |
| Input photons flux (#/m$^2$) | 3.55E+21 | 9.72E+20 | 8.77E+20 | 9.25E+20 |
| %Photons-Relative to BB | 78.2% | 27.4% | 24.7% | 26.1% |
| Low OH silica waveguide | | 357-655 nm | 656-880 nm | 881-1240 nm |
| Power T(L=10 cm) | | 99.83% | 99.99% | 99.99% |
| Photons T(L=10 cm) | | 99.86% | 99.99% | 99.99% |
| PMMA waveguide | | 357-655 nm | 656-880 nm | 881-1240 nm |
| Power T(L=10 cm) | | 80.51% | 85.13% | 51.42% |
| Photons T(L=10 cm) | | 81.36% | 85.05% | 49.36% |
| Power T(L=3 mm) | | 99.34% | 99.52% | 95.56% |
| Photons T(L=3 mm) | | 99.38% | 99.51% | 95.07% |

Table 4. Spectral loss calculation for four junction PV cell

| | BB | SR1 | SR2 | SR3 | SR4 |
|---|---|---|---|---|---|
| | AM1.5D | GaInP | GaAs | GaInAsP | GaInAs |
| Wavelength (nm) | 280-4000 nm | 280-689 nm | 690nm-886nm | 887-1240nm | 1241-1771nm |
| Input power (W/m$^2$) | 887.65 | 423.76 | 192.89 | 171.75 | 90.83 |
| %Power-Relative to BB | 99.0% | 47.7% | 21.7% | 19.4% | 10.2% |
| Input photons flux (#/m$^2$) | 3.55E+21 | 1.08E+21 | 7.59E+20 | 9.02E+20 | 6.71E+20 |
| %Photons-Relative to BB | 96.1% | 30.4% | 21.4% | 25.4% | 18.9% |
| Low OH silica waveguide | | 357-689 nm | 690nm-886nm | 887-1240nm | 1241-1770nm |
| Power T(L=10 cm) | | 99.85% | 99.99% | 99.99% | 99.99% |
| Photons T<br>(L=10 cm) | | 99.88% | 99.99% | 99.99% | 99.99% |
| PMMA waveguide | | 357-689 nm | 690nm-886nm | 887-1240nm | 1241-1770nm |
| Power T(L=10 cm) | | 81.09% | 84.79% | 50.57% | 14.78% |
| Photons T<br>(L=10 cm) | | 81.98% | 84.71% | 48.58% | 13.14% |
| Power T(L=3 mm) | | 99.36% | 99.50% | 95.45% | 54.28% |
| Photons T(L=3 mm) | | 99.40% | 99.50% | 94.97% | 50.01% |

Based on the structure, the transmission losses in the designed system can be divided into three categories: Fresnel reflection loss, propagation loss and coupling loss. Fresnel reflection loss happens at all the interfaces between two different materials with different refractive index, which includes the lens surface, waveguide surface and MJ cell surface. Propagation loss mainly depends on the waveguide material and fabrication process. Coupling loss occurs at the coupler surface.

The coupler angle is the most important factor for the coupling loss. In designed structure, the incident light is collected and concentrated onto the waveguide surface, and then it is refracted to the coupler surface. Ideally, all the light that hit on the coupler surface can be reflected to the waveguide by the coupler which acts as a turning mirror. However, based on Snell's law, total internal reflection happens when the angle of the incident light is larger than the critical angle, which means that the light with an incident angle smaller than the critical angle is impossible reflected to the waveguide by the coupler surface. Therefore, the coupling efficiency of the system depends on the angle of the incident light and the refractive index of the waveguide materials.

To reduce the coupling loss, the coupler angle has to be optimized. Figure 41 shows the simulation to find the best coupler angle. The incident light with an incident angle $-\theta_M \le \theta \le \theta_M$ can be expressed as:

$$\vec{k}_{in} = k\left(\sin\gamma \cdot \cos\Omega, \cos\gamma, \sin\gamma \sin\Omega\right) \tag{5.8}$$

The light is incident on the top of the waveguide surface first, and then refracted to the coupler surface. The relationship between the incident angle $\theta$ and the refracted angle $\gamma$ can be given by Snell's law:

$$n_{air} \cdot \sin\theta = n_w \cdot \sin\gamma \tag{5.9}$$

where $n_{air}$ is the refractive index of the air and $n_w$ is the refractive index of the waveguide. At the coupler surface, the light with an incident angle that is larger than the critical angle can be reflected to the waveguide by total internal reflection. The reflected light can be expressed as:

$$\vec{k}_r = k\left(\sin\gamma \cdot \cos\Omega, \cos\theta_y \sqrt{1-\sin^2\gamma\cos^2\Omega}, \sin\theta_y \sqrt{1-\sin^2\gamma\cos^2\Omega}\right) \tag{5.10}$$

where $\theta_y = 2\beta - \arctan\left(\tan\gamma \cdot \sin\Omega\right)$. Figure 39 (c) shows that when the coupler angle is 45 °, the angle of reflected light in both the XZ plane $\varnothing_{x0}$ and YZ plane $\varnothing_{y0}$ reach the minimum value, which leads to minimum coupling loss to the waveguide.

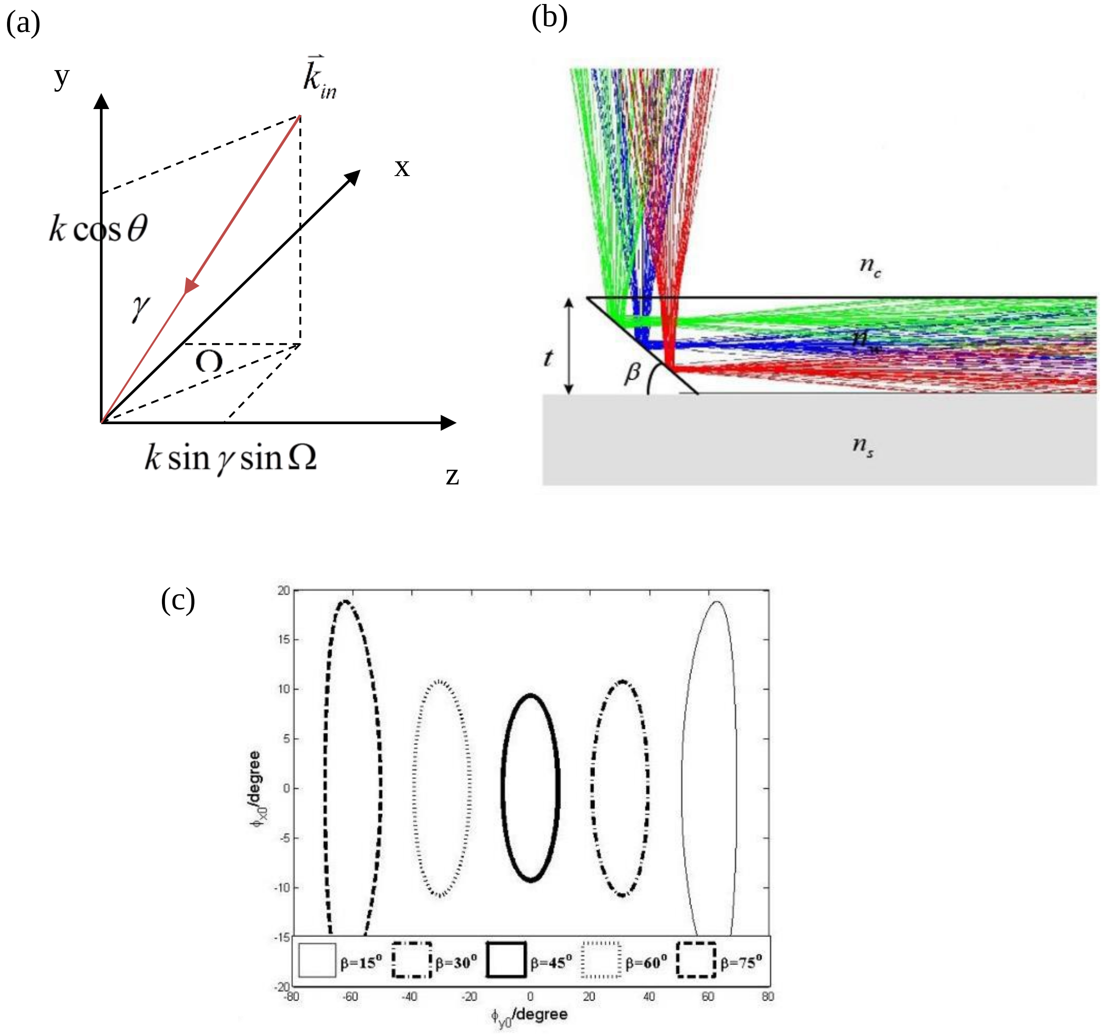

Figure 41. (a) The incident light with an incident angle; Simulation of (b) ray traces in waveguide and (c) the angle of the reflected light at the coupler surface based on different coupler angle.

# CHAPTER VI

# DEMONSTRATION OF A MICRO WAVEGUIDING SOLAR CONCENTRATOR

## 6.1 Overview

The main advantage of the CPV system and the use of the lens array is to reduce the area of the solar cell as well as the thickness and the weight of the system. In order to make a compact CPV system, photolithography technique is used to fabricate micro leveled waveguide system.

SU-8 photoresist is used as the waveguide material since polymer planar waveguide technology is reported to be one of the cost effective technology for fabrication of large cross sectional multimode devices. SU -8 photoresist has some interesting properties, which make it a very attractive material for a wide range of applications including micro-machining, micro-optics and packaging. Moreover, SU-8 photoresist is highly transparent for wavelengths that is greater than 600 nm, and it is chemically and mechanically stable. Also. It has shown a good heat resistance. The operating temperature is around 200 ℃. It can be spin coated at a thickness ranging from a few microns to a millimeter [84].

## 6.2 Fabrication process of SU-8 waveguide

Since the feature size of the designed waveguide is in micron level, wafer fabrication technique is used to fabricate SU-8 waveguide on silicon wafer. In the fabrication process, patterning or photolithography is one of the most critical operations. The goal of photolithography is to create or transfer a pattern with the dimensions established in the design in and on the wafer surface.

The fabrication process starts with a pattern and photomask design that can be transferred to the wafer. L-Edit is the software that is used to design the pattern in the mask. The waveguide pattern in the photomask is shown in Figure 42. Then, the pattern on the photomask can be transferred into a layer of photoresist. Photoresist is a light-sensitive material. When the photoresist is exposed to the light at certain wavelength, the structure and properties can be changed. Basically, there are two types of photoresist: positive photoresist and negative photoresist. Negative photoresist can be changed from a soluble condition to an insoluble after exposure. This chemical change is called polymerization. The soluble part can be removed by developer and the exposure area is remained on the wafer. On the other hand, the exposure area of positive photoresist can be removed after development.

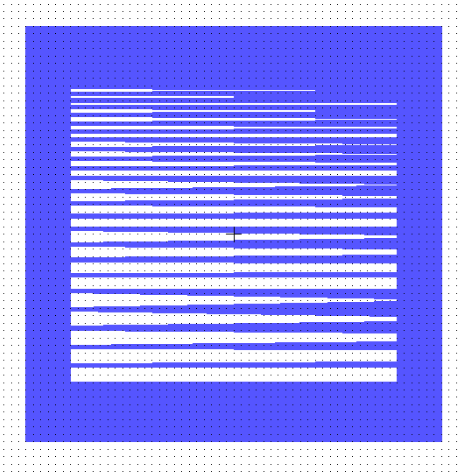

Figure 42. Mask design of straight waveguide and tapered waveguide.

Transferring the image from the mask onto the wafer surface layer usually have ten steps, which includes surface preparation, photoresist apply, soft bake, alignment and exposure, development, hard bake, develop inspect, etch, photoresist removal and final inspection. Since SU-8 photoresist is used as the waveguide material, there is no etch step in our fabrication process. The photolithography process for making SU-8 waveguide is shown in Figure 43.

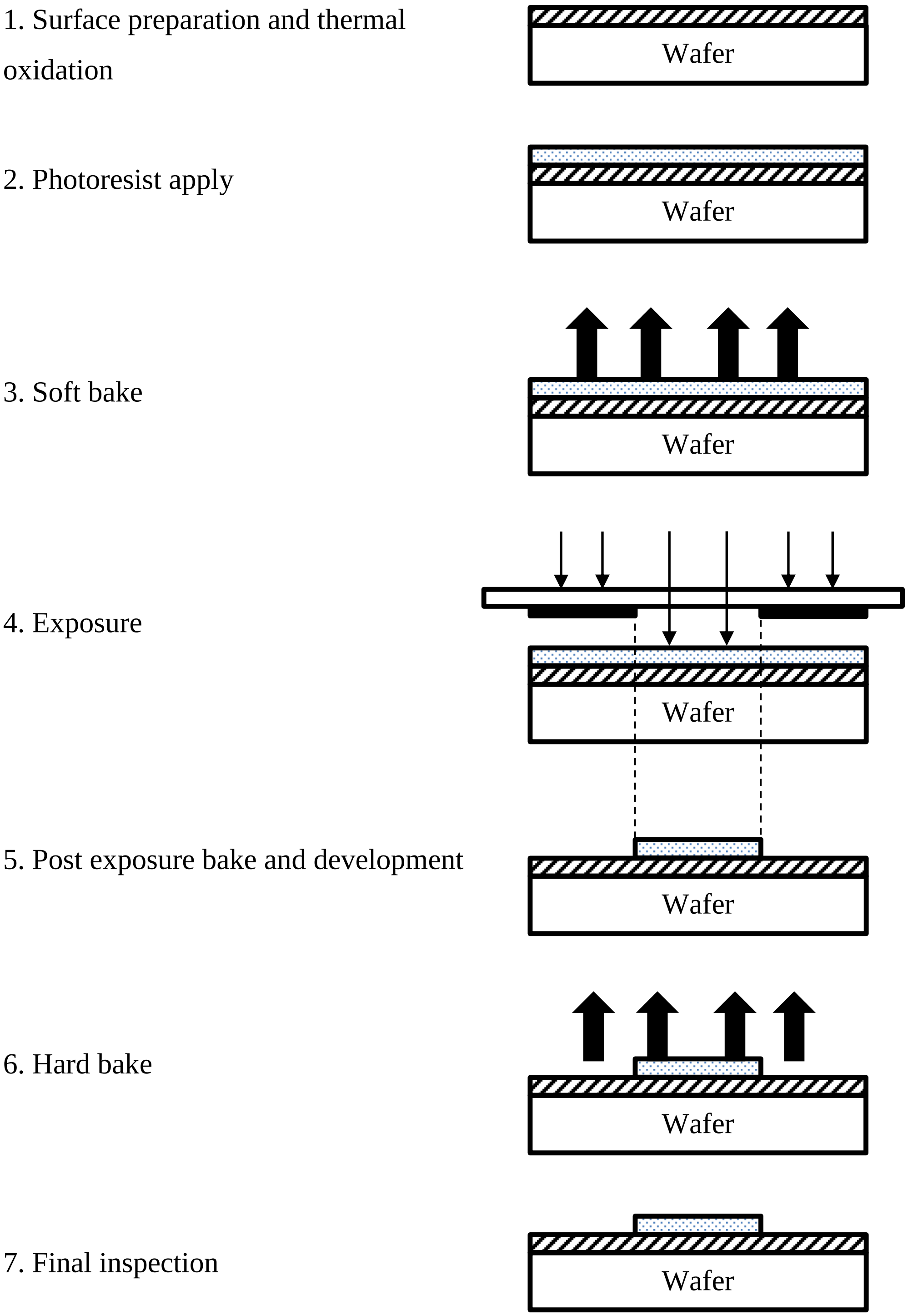

Figure 43. Photolithography process for making SU-8 waveguide.

The light can be guided in the waveguide by total internal reflection, which requires a core material with higher refractive index than that of the covered layer. The goal of thermal oxidation is to grown a $SiO_2$ layer between the waveguide and silicon wafer as the covered layer, because the refractive index of $SiO_2$ and SU-8 are around 1.45 and 1.69, respectively. Thermal oxidation is based on a simple chemical reaction and can be separated into two methods: dry oxidation and wet oxidation:

$$Si(solid)+O_2(gas)\rightarrow SiO_2(Solid) \tag{6.1}$$

$$Si(solid)+H_2O(gas)\rightarrow SiO_2(Solid)+2H_2(gas)\uparrow \tag{6.2}$$

The oxidation growth rate in wet oxidation is faster than the dry oxidation, but the quality in wet oxidation is not as good as dry oxidation. Oxidation temperatures are between 900 ˚C and 1200 ˚C. In our fabrication process, the temperature is set to be 1100 ˚C.

The thickness of SU-8 photoresist is determined by the spin coating speed, as shown in Figure 44. In our case, the thickness of designed waveguide is around 100 µm, which requires a spin coating speed of around 2000 rpm. After the spin coating, the thickness of the edge is higher than the thickness in the center of the wafer due to the strong air turbulences. Edge bead may cause sticking to the mask as well as an undesired gap during exposure. In order to have uniform surface and reduce the edge bead, Q-tips can be used to remove the photoresist on the edge after the spin coating. Also, a solvent can be dispensed onto the edge of the rotating substrate to lower the edge bead. Figure 45 shows the picture of the sample after the spin coating.

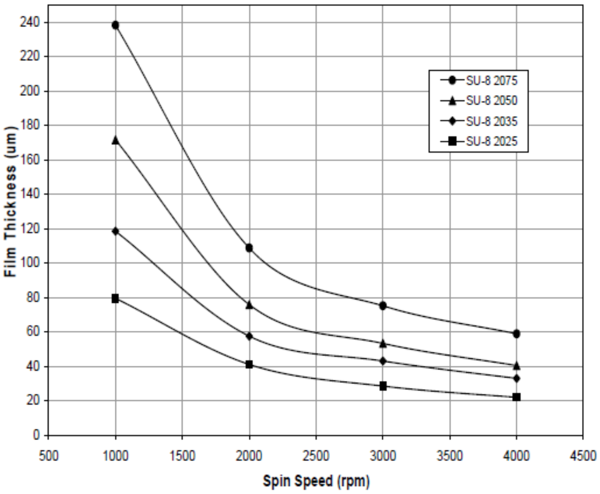

Figure 44. SU-8 spin speed versus thickness.

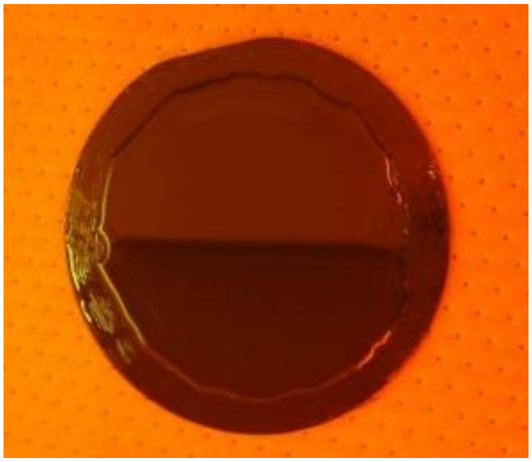

Figure 45. The picture of the sample after the spin coating. The photoresist on the edge is removed by Q-tips.

Soft bake is to evaporate solvents from the resist. Soft bake temperature and time are determined by the thickness of the resist. Underbaking can have incomplete image formation at exposure and poor adhesion. Overbaking can cause the polymers not sensitive to exposure. For a thickness of 100 µm resist, soft bake time is round 5 minutes at 65˚C and 10-20 minutes at 95 ˚C. A hotplate or a convection oven can be used for soft bake. In our case, a level hotplate is used for soft bake procedure. A level hotplate has good thermal control and uniformity. Using convection oven may from a skin on the resist, which can inhibit the evolution of solvent and results in incomplete drying of the film.

In order to obtain vertical sidewalls of the resist, a 350 nm UV light source is used for exposure process. The exposure energy required for a 100 µm resist is around 230 mJ/cm$^2$. Based on the type of substrate, it may require another 50% exposure doses. With optimal exposure, a visible image can be seen in the film within 5-15 seconds after being placed on the post exposure bake (PEB) hotplate.

Development processes are aimed to form a pattern with the same dimension of the design. Underdevelopment can have coved sidewall in the resist. Overdevelopment will remove too much resist from the edge and top surface. The development time of a 100 µm resist is around 8 minutes.

Hard bake is the last step in our lithography process. The purpose is to evaporate solvents in the resist and harden the resist. The recommend temperature is in the range of 150 ˚C to 250 ˚C for a time between 5 and 30 minutes.

The 45˚ angle coupler is also made in SU-8 waveguide by lithography technology. Based on Snell's law, the coupler angle can be calculated by:

$$\varphi = 90 - \arcsin\left[\sin\left(90-\theta\right)\times\frac{n_1}{n_2}\right] \tag{6.3}$$

where $\varphi$ is the coupler angle, $\theta$ is the tilt angle of the sample, $n_1$ is the refractive index of incident medium and $n_2$ is the refractive index of SU-8. The minimum coupler angle can be achieved in the air is around 53˚. In order to make a 45˚ coupler, the sample and film photomask are immersed in the water. Figure 46 shows the fabrication process of the waveguide with 45˚ coupler and photograph of the tilt stage and coupler.

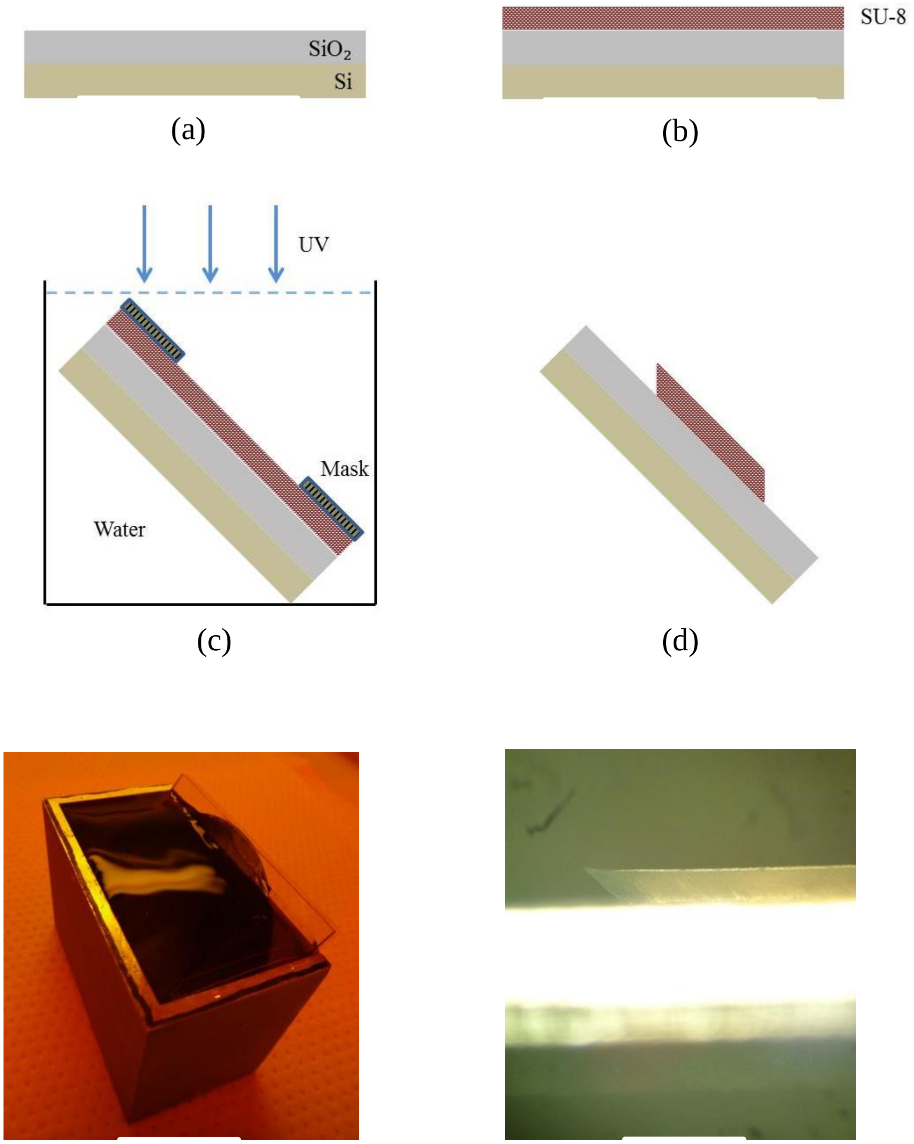

(a) (b) (c) (d) (e) (f)

Figure 46. Key procedures of fabrication process for SU-8 waveguide with 45˚ coupler: (a) thermal oxidation, (b) photoresist spin coating, (c) exposure in the water and (d) development and photograph of (e) the tilt stage and (f) coupler.

After lithography, the sample is diced by a diamond saw to match the size of the measurement setup. So as to reduce the coupling loss, the cross section surface is polished by the polishing pad with different grain size. The sample is first polished by the polishing pad with a grain size of 5 µm, and followed by 3 µm and 0.5 µm polishing pad. Figure 47 shows the photograph of the cross section of the polished SU-8 waveguide.

Figure 47. Photograph of the cross section of the polished SU-8.

## 6.3 Measurement setup and results

Figure 48 shows the experimental setup for measuring the optical loss of the waveguide. The Ocean optics high power white light and Ocean optics spectrometer are used as the light source and detector, respectively. A multimode fiber with a diameter of 62.5 µm is connected to light source and a multimode fiber with a diameter of 200 µm is connected to the detector.  The numerical aperture NA determines the range of angles of the light that the optical system can accept or emit, which is given by: [85]

$$NA = n \sin \theta \qquad (6.4)$$

where n is the refractive index of the medium, θ is the maximum half angle of the light that can enter or exit the optical system. In the measurement setup, the NA of the input fiber is smaller than the waveguide and output fiber which reduces the coupling loss of the waveguide. Also, a refractive index matching gel is used to attach the fiber and waveguide sample to reduce the coupling loss. The measured spectrum of fiber to fiber is used as the reference. The transmission of the waveguide can be calculated by the ration of the sample spectrum to the reference spectrum.

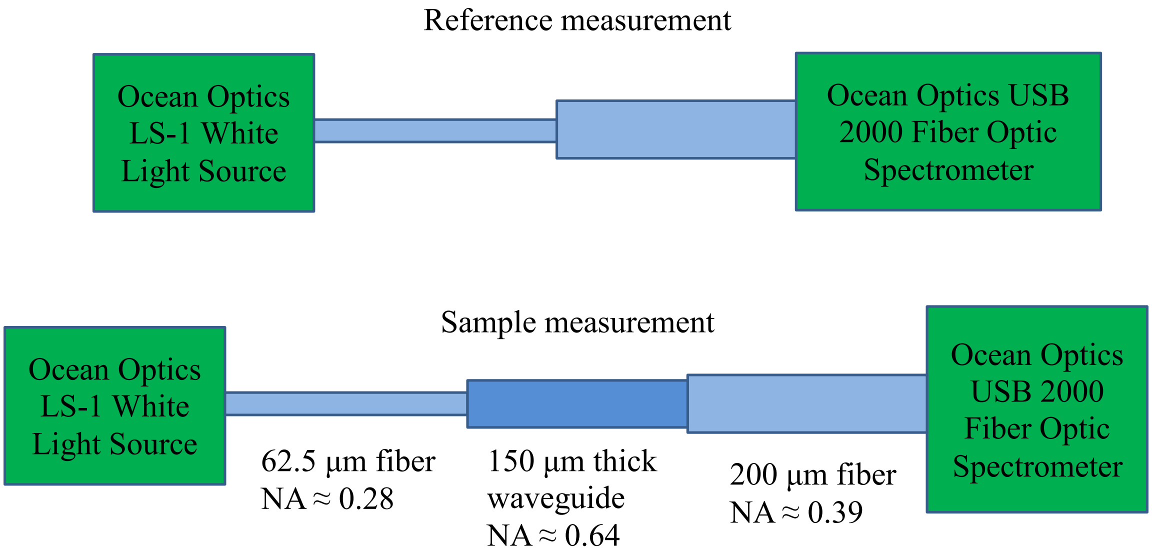

Figure 48. Experimental setup for measuring the optical loss of the waveguide.

The measurement results of the transmission, propagation loss and coupling loss are shown in Figure 49. The photograph and the transmission spectrum indicate that SU-8 material has a high absorption in visible range and the waveguide has strong scattering loss. The coupling loss of the waveguide is around 7 dB and the propagation loss is around 6 dB/cm at the wavelength of 650 nm, which is obtained by cut back method.

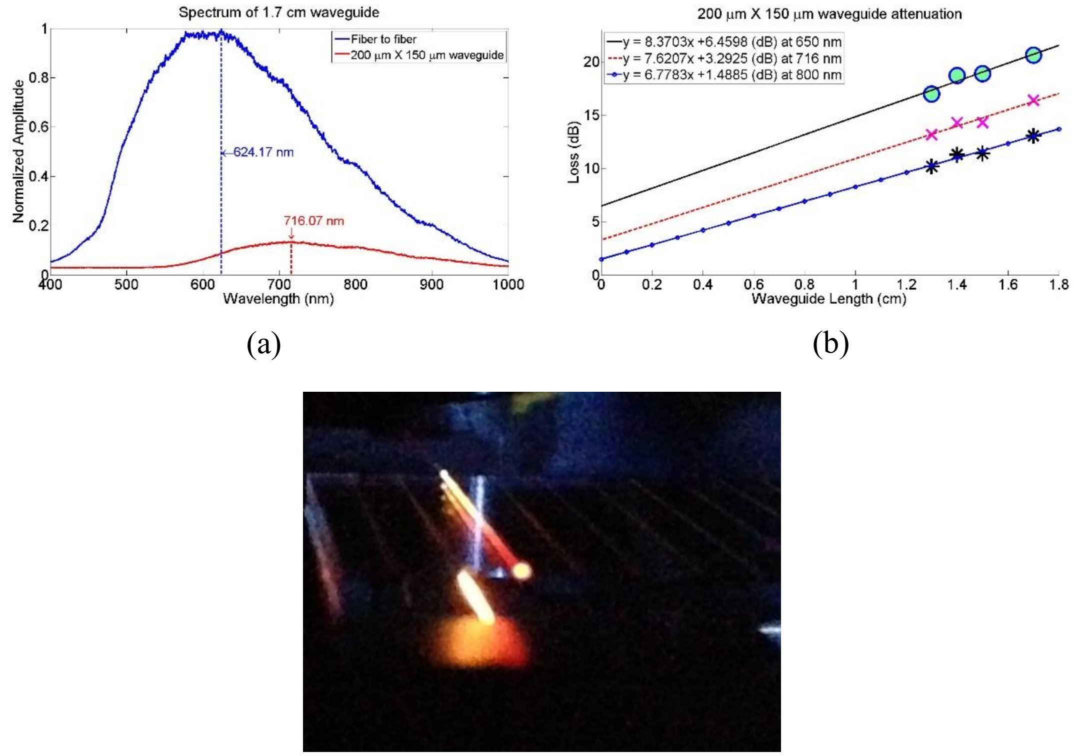

(a) (b)

(c)

Figure 49. The measurement results of (a) the transmission spectrum, (b) propagation loss and coupling loss, and (c) the picture of the waveguide during the measurement.

In order to reduce the scattering loss, the surface roughness and uniformity are characterized by DekTak surface profiler. Two samples are used in this measurement: one sample has a thickness of around 70 μm and the other has a thickness of around 50 μm. The results shows that the difference of the waveguide thickness from center to the edge is around 5-10 μm. There are several reasons that can lead to non-uniform thickness. One reason is the edge bead. After the spin coating, the thickness of the edge will be higher than the center, and this effect will be more critical for small wafers even if we removed the photoresist on the edge after spin coating. The temperature and time of soft bake process are also important to control the surface uniformity and surface roughness. The recommended soft bake time of SU-8 resist with a thickness of 100 µm from the manufacture data sheet is around 5 min at 65 ˚C and 20 min at 95 ˚C. The increase of the soft bake time can reduce the roughness of the surface and make the surface more uniform. In the experiment, the soft bake time is increased to 24 hours. The fabrication parameters and surface profile of two samples are shown in Table 5 and Figure 50.

Table 5. Fabrication parameters of two samples.

| 2 inch wafer | Sample 1 | Sample 2 |
|---|---|---|
| Spin coating speed | 500/3000/6000rpm | 500/4000/6000rpm |
| Soft bake | 24 hours at 65 ℃<br>ramp to 95 ℃ | 24 hours at 65 ℃<br>ramp to 95 ℃ |
| Exposure | 230×1.5 mJ/cm² | 220×1.5 mJ/cm² |
| thickness | 70-79 µm | 51-56 µm |

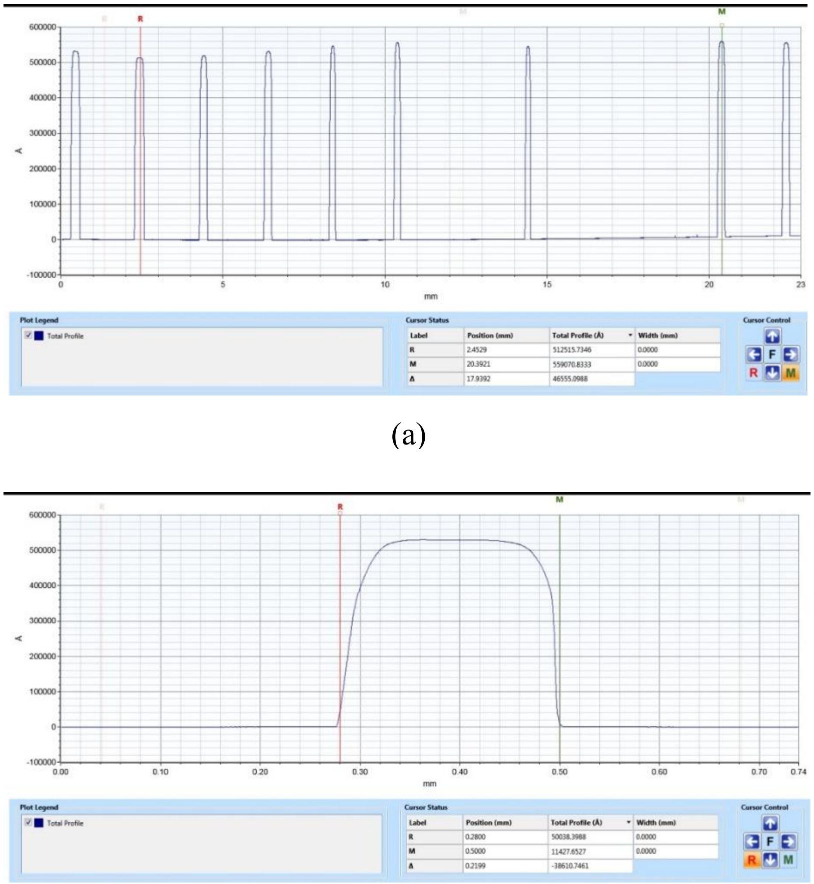

Cursor Status

| Label | Position (mm) | Total Profile (Å) | Width (mm) |
|---|---|---|---|
| R | 2.4529 | 512515.7346 | 0.0000 |
| M | 20.3921 | 559070.8333 | 0.0000 |
| Δ | 17.9392 | 46555.0988 | |

(a)

Cursor Status

| Label | Position (mm) | Total Profile (Å) | Width (mm) |
|---|---|---|---|
| R | 0.2800 | 50038.3988 | 0.0000 |
| M | 0.5000 | 11427.6527 | 0.0000 |
| Δ | 0.2199 | -38610.7461 | |

(b)

Figure 50. Surface uniformity and surface roughness measurement using DekTak surface profiler.

Figure 51 shows the experiment setup for the waveguide with a 45˚ coupler. A Xe arc lamp is used as the light source, which has an intensity over 1000 W/m$^2$. Since the light source is not a perfect collimated light, two mirrors with 45˚ angle are used to reflected the light and make the light collimated by keeping a long distance between two mirrors.

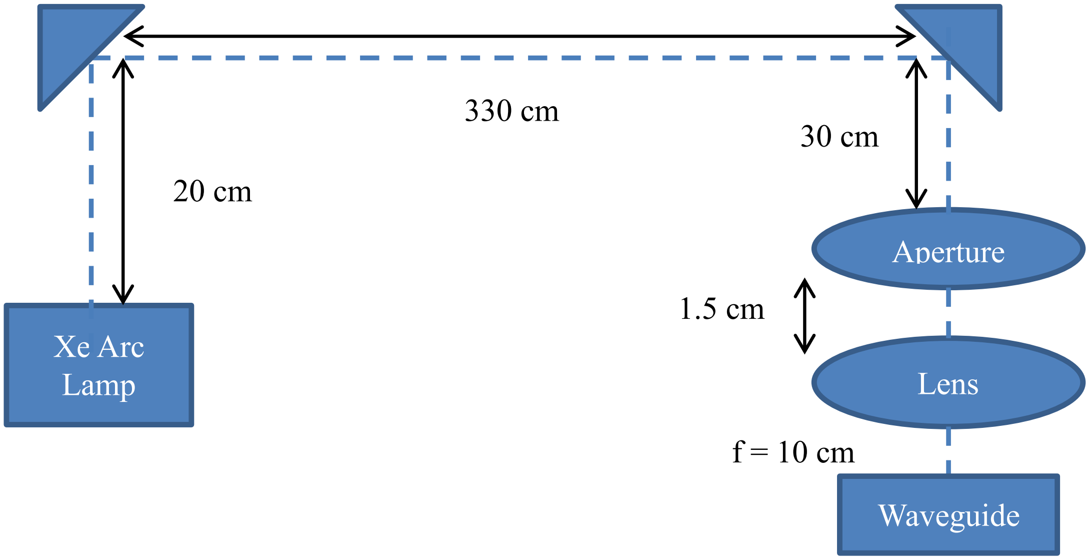

(a)

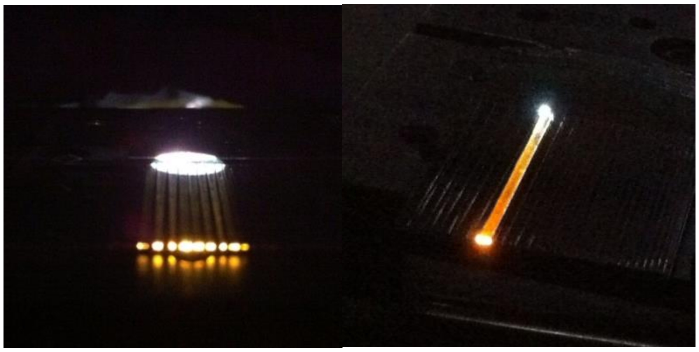

(b)

Figure 51. (a) Experiment setup for the waveguide with a 45˚ coupler and (b) the picture of the measurement.

## 6.4 Conclusion

A micro-level solar concentrator waveguide is made using SU-8 photoresist. In order to make 45˚ coupler in the waveguide, the sample is positioned on a tilted stage and immersed in the water during the exposure procedure. Surface roughness and uniformity are important to the performance of the waveguide. The propagation loss of the SU-8 waveguide is around 8 dB/cm at the wavelength of 650 nm, which is primarily due to the scattering in the waveguide and absorption of the material.

# CHAPTER VII

# DEMONSTRATION OF A 2D-WAVEGUIDING SOLAR CONCENTRATOR*

## 7.1 Overview

This chapter will show an experimental demonstration results for a novel, two-dimensional waveguiding solar concentrator consisting of a lens array which is used as the essential concentrator and a multimode waveguides as the secondary concentrator. The lens array collects the incident sun light and focuses it onto a 45˚ coupler which acts as a turning mirror. The turning mirror couples the light into the multimode waveguide, which alleviates connection, cooling and uniformity issues associated with conventional solar concentrating systems. Therefore, a large amount of sunlight can be efficiently focal to a small waveguide cross-section and reach to an array of PV cells with high optical efficiency. To achieve the maximum coupling efficiency of the light to the waveguide, the design of the turning mirror and waveguides are optimized to eliminate any inherent coupling loss in the waveguide propagation. Experimental results indicate that a 38 mm diameter lens with a multimode waveguide that is 3 mm ×3 mm ×10 cm can achieve 126x concentration with 62.8% optical efficiency by using total internal reflection. A critical requirement for this design is maintaining low waveguide

---

* Part of this chapter is reprinted by the permission from “First demonstration of a novel 2D-waveguiding solar concentrator” by R. Huang, Y. Liu, C. K. Madsen, SPIE Optics + Photonics 2014, 19-21 August 2014, San Diego, California. Copyright 2014 SPIE.

propagation losses, which as we demonstrate can be less than 0.1 dB/cm. Considering 100% TIR coupling and the use of antireflection layers, the theoretical efficiency limit for this particular system is  around 88%.

## 7.2 Simulation results of the 2d-waveguiding solar concentrator

Table 6 shows the simulation results of the designed system by ZEMAX. The lens that has a diameter of 38 mm and a focal distance of 123 mm is used as the concentrator. A 3 mm × 3 mm PMMA waveguide is used in the simulation. In this structure, the concentration ratio of the lens is around 126x. The incident light angle on the lens is assumed as ±0.5° in this simulation. The optical efficiency η is defined as the ratio of the output power at the end of waveguide to the power of the incident light on the lens. The simulation results shows that the optical efficiency of the system is 69.6%, which is mainly due to the Fresnel loss and TIR coupling loss. Since the refractive index of PMMA is around 1.49, the critical angle of the PMMA waveguide is 42 °, which leads to the fact that all the light can be reflected to the waveguide by TIR at the coupler surface, if the maximum incident angle at the top surface of the waveguide is around ±5 °. The angle of light after the lens, however, is approximately ±8.8 °, which means that the efficiency is reduced due to the coupling loss and part of the light leaks at the coupler surface [86].

In order to improve the coupling efficiency, a lens with larger f-number could be used to have zero TIR loss at the coupler surface, in trade for a larger spot size which reduces the concentration ratio of the system. Moreover, there are a total of four interfaces suffering Fresnel reflections, which are the front and back side of the lens, the air/waveguide interface and the output end of the waveguide. Antireflection layers can be coated at the lens surfaces, as well as the end of the waveguide surface, effectively reducing the total Fresnel loss to around 12%.

Thus, considering 100% TIR coupling efficiency and the use of antireflection layers to reduce the Fresnel loss, the theoretical efficiency limit for this particular system is around 88%.

Table 6. Simulation results of lens-to-waveguide system.

| | | Relative Percent |
|---|---|---|
| Fresnel loss | Lens | 6.1% |
| | Waveguide top | 3.8% |
| | Waveguide end | 4.2% |
| | Total | 14.1% |
| | | Absolute Percent |
| Propagation Loss | For L=50mm straight waveguide | 0.1% |
| Coupling Loss | Spot Size | 0.3% |
| | TIR | 19.0% |
| Total Efficiency | | 69.6% |

In order to reach the maximum concentration, the simulation in Figure 52 shows the maximum achievable waveguide concentration for the system presented above. It shows that the upper limit is 7.3x before the efficiency drops, which indicates that the total concentration of the system can be 126x*7.3x=920x by using the tapered waveguide.

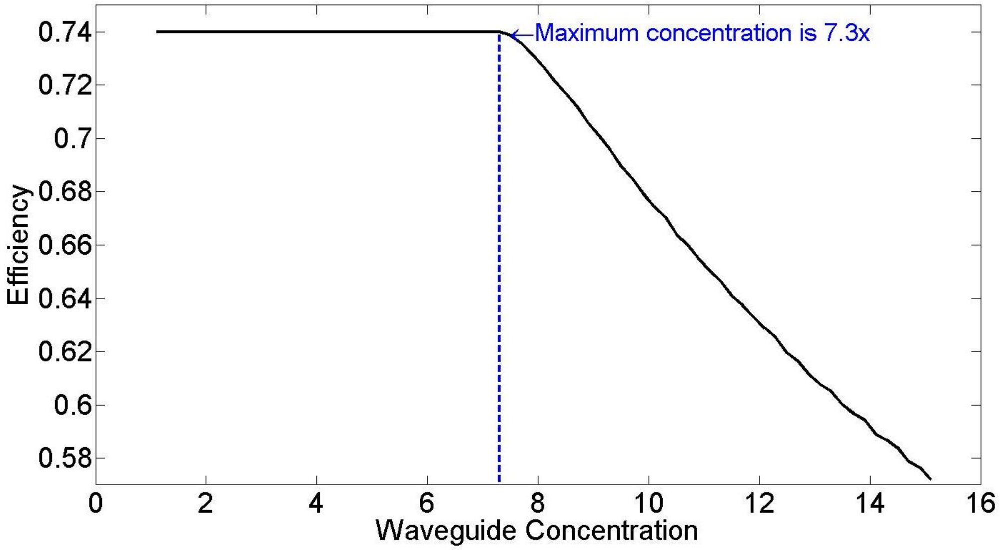

Figure 52. The maximum achievable waveguide concentration for the system.

## 7.3 Experiment results of the 2d-waveguiding solar concentrator

We selected PMMA as our waveguide material, since this material has been studied previously and reported to be transparent and low loss in the visible range[87]. The PMMA waveguide, shown in Figure 53, is made using Full Spectrum H-Series 20×12 $CO_2$ laser cutter. The full power of the laser cutter is 40 W. With a precise focal length, the minimum feature size is around 1 mm.

Figure 53. A PMMA waveguide is made by CO2 laser cutter.

In order to have the smooth surface and reduce the scattering loss of the waveguide, the parameter of the laser cutter is optimized. The waveguide structure can be designed in laser cutter software RetinaEngrave3D. There are three important parameters in the laser cutter software: power, speed and pass. The parameters can be adjusted based on the thickness of the waveguide material. The laser beam is reflected by three mirrors and focal to the target by a 2” lens. The focal point of the laser beam is set at the middle of the material thickness to minimize beam divergence. The coaxial gas jet can remove the cutting debris and protect the lens from contamination. The gas pressure is adjusted depending on the cutting speed and the thickness of the material. A protective masking layer can be used to avoid buildup of vapor residue on cut surfaces. Figure 54 shows the laser cutter and design in RetinaEngrave3D.

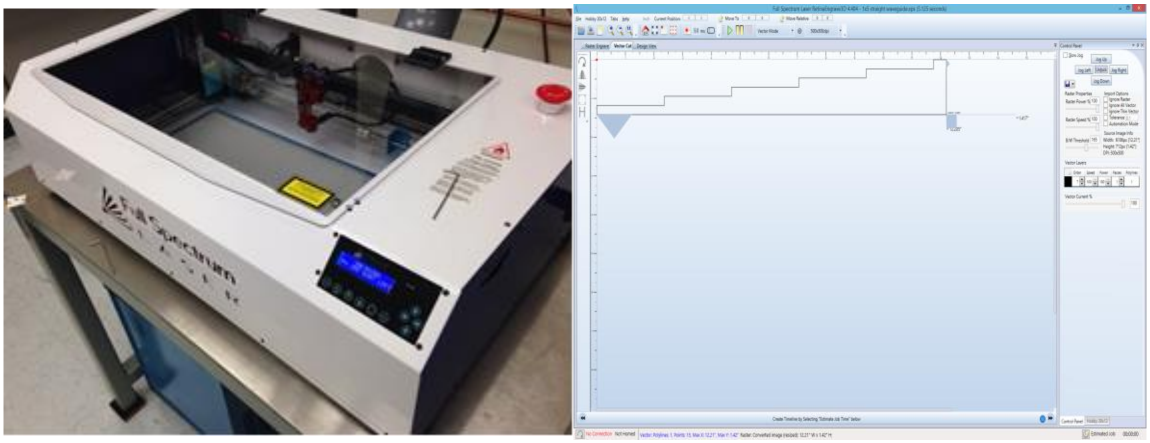

(a) (b)

Figure 54. (a) Full Spectrum H-Series 20×12 $CO_2$ laser cutter and (b) the control panel of RetinaEngrave3D.

End coupling method or cut back method is used to measure the coupling loss of the 45° coupler and propagation loss of a straight PMMA waveguide. In the measurement, a 532 nm laser is used as the light source, and PM320E power meter with a Si photodiode power sensor is used as the detector to measure the output power of the waveguide. In this case, the 8 cm straight waveguide is shortened 6 times in order to have accurate data to calculate the loss. The loss versus waveguide curve shows in Figure 55, in which the slope and y axis intercept represent the propagation loss and the coupling loss, respectively. Thus, the measured propagation loss is less than 0.1 dB/cm and the coupling loss is 0.8 dB, which indicates that 17% of the light escapes from the waveguide due to the incident angle and TIR.

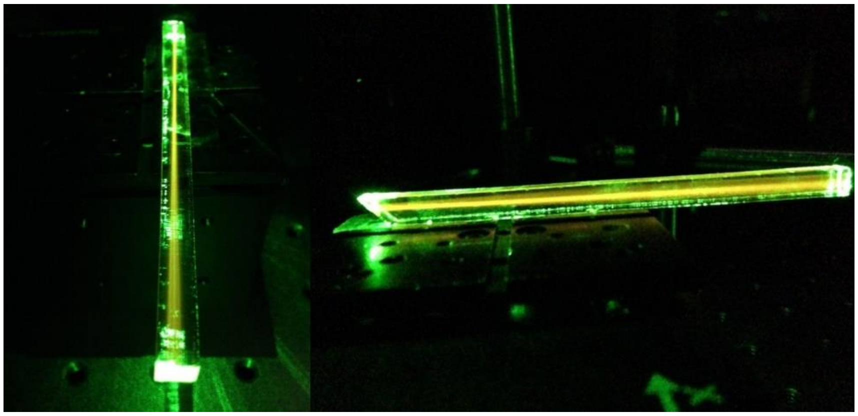

(a)

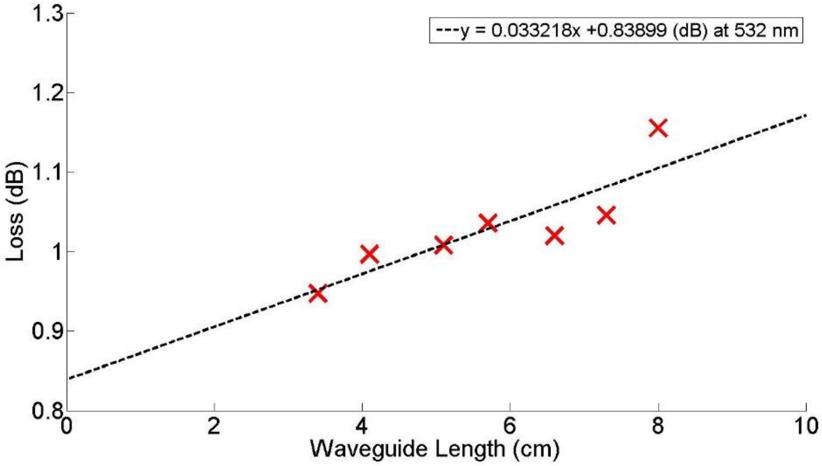

(b)

Figure 55. (a) The waveguide loss is measured by cut back method with a 532 nm laser. (b) The loss versus waveguide curve is obtained by shorten the waveguide.

Figure 56 shows the experimental setup for measuring the optical efficiency of the designed system, which contains a high power white light source, two mirrors and power meter. The high power white light source is used to mimic the sun light. In order to have a collimated light, the distance between the first mirror and the second mirror is around two meters. Then, the light is made normal to the lens by the second mirror which is a 45 °turning mirror. The light collected by the lens is concentrated to the coupler and coupler into the waveguide. The lens diameter is 38 mm and the dimension of the PMMA waveguide used in this experiment is 3 mm × 3 mm × 10 cm. No tapered waveguide is measured in this demonstration.

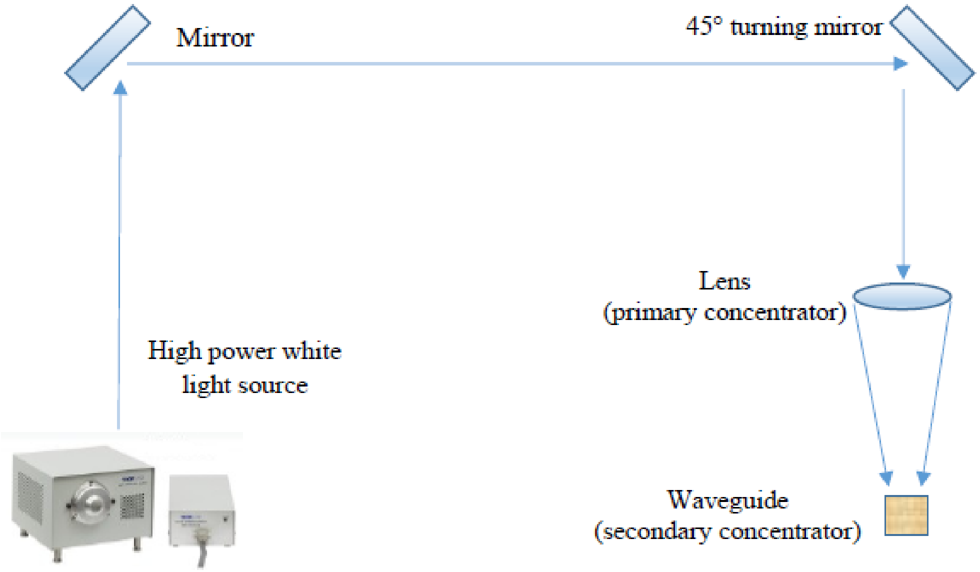

Figure 56. Experiment setup for measuring optical efficiency of the system.

The experimental results are shown in Table 7, which indicates that a geometric concentration ratio of 126x and an optical concentration ratio of 72x can be achieved by a straight waveguide concentrator system. According to the simulation results, the maximum waveguide concentration is 7.3x, which leads to 920x geometric concentration and 525x optical concentration when using a tapered waveguide instead of the straight waveguide as the secondary concentrator. The measured optical efficiency is

62.8% which is a difference of 6.6% from the simulation result of 69.4%. One possible reason is that the incident light angle before the lens is larger than our expected angle of ±0.5 °. As discussed in the simulation results, all the light can be reflected to the waveguide by TIR at the coupler surface if the incident angle on the top of the waveguide surface is less than 5 °. However, the divergence angle of this lens (38 mm diameter, f = 123 mm) is 8.8 ° which is larger than the maximum angle of the light that can be coupled to the waveguide. Based on Snell's law, a material with higher refractive index can have a smaller critical angle, which means the light with large incident angle on the waveguide can be reflected to the waveguide by TIR at the coupler surface if using the material with higher refractive index as the waveguide material. Another possible reason is the surface roughness of the waveguide. Undesired reflection of the light would happen at a rough coupler surface, which will increase the angle of the reflected light, part of the light may escape from the waveguide surface and cannot be constricted by total internal reflection.

Table 7. The experiment results of lens-to-channel waveguide system.

| Parameter | 38 mm diameter lens |
|---|---|
| Focal length | 12.3 cm |
| Optical efficiency | 62.8% |
| Geometric concentration | 126 |
| Optical concentration | 72 |

The device demonstration is shown in Figure 57, which contains a 1×3 lens array and waveguide array. The holder of the concentrator system is made by a 3D printer. The light is concentrated to the waveguides by a lens array, and reflected to the waveguides by a 45 °coupler. The light is finally guided to the edge of waveguide by total internal reflection.

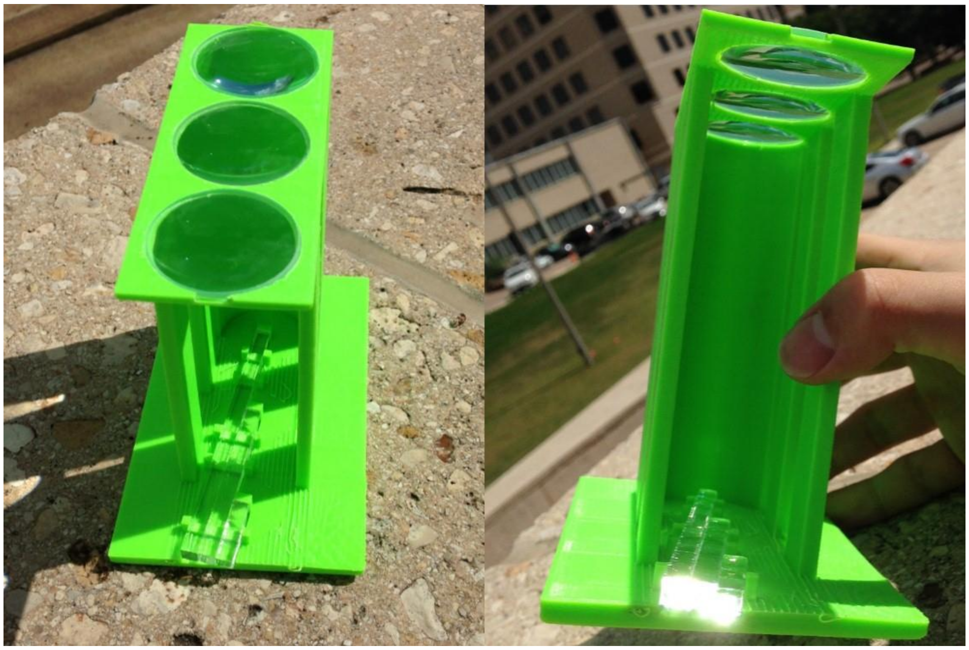

Figure 57. The demonstration of 1×3 lens-to-channel waveguiding concentrator system.

## 7.4 Conclusion

The designed waveguide concentrator system contains a lens array and a channel waveguide array. In this system, any decoupling loss in the waveguide can be avoided. An optical efficiency of 69.6% and 7.3x waveguide concentration can be achieved by ZEMAX simulation based on 38 mm diameter lens and PMMA waveguide. Experimental results show that the system can have 62.8% optical efficiency at 126x concentration for the straight waveguide. Overall, 920x concentration can be reached if using a tapered waveguide instead of the straight waveguide.

# CHAPTER VIII

# DEMONSTRATION OF AN INTERMEDIATE-SCALE LENS-TO-CHANNEL WAVEGUIDE SOLAR CONCENTRATOR*

## 8.1 Overview

Solar concentrating photovoltaic systems have the potential to reduce total system cost and achieve higher efficiency by replacing a large solar cell surface with cheap optical elements, in which a large area of light can be efficiently collected and concentrated onto a small optical device and guided to an array of co-located photovoltaic cells with high optical efficiency. In this work, a 60 mm by 60 mm lens to channel waveguide system is used for demonstration. A separate, aluminum-coated 45° coupler is fabricated and attached to the waveguide to improve the coupling efficiency and to avoid any inherent decoupling loss.

## 8.2 Structure of the designed system

Previously we proposed a lens-to-channel waveguide system which consists of a primary concentrator (a Fresnel lens array) and a secondary optic (PMMA multimode waveguide). The sunlight is collected by the lens array and coupled to the waveguide by

---

* Part of this chapter is reprinted by the permission from "Demonstration of an intermediate-scale lens-to-channel waveguide solar concentrator" by R. Huang, Y. Liu, C. K. Madsen, SPIE Optics + Photonics 2015, 9-13 August 2015, San Diego, California. Copyright 2015 SPIE

a 45 °coupler which is fabricated in the PMMA waveguide and is aligned at the focal point of each lens. The light can propagate in the waveguide by total internal reflection (TIR) and reach the PV cell at the edge of the waveguide [88].

The measured optical efficiency of previous experiment demonstration is 62.8%, which is mainly due to the TIR loss at the coupler surface in the PMMA waveguide and Fresnel losses. Since the 45 °coupler is made in the waveguide, the maximum incident angle is limited by the waveguide material. Figure 58 shows the calculation of the relationship between the incident angle, coupler angle and efficiency for PMMA waveguide. Since the critical angle of PMMA material is around 42˚, only the light with an incident angle larger than the critical angle can be reflected to the waveguide by TIR. When the coupler angle is 45˚, the increase of the incident angle can reduce the TIR efficiency at the coupler surface. Also, part of the light than is coupled to the waveguide cannot be confined in the waveguide by TIR if the coupler angle increases to above 70˚. In order to keep high coupling efficiency, the incident angle must be small enough by using large f-number lens, which increases the thickness and weight of the whole system.

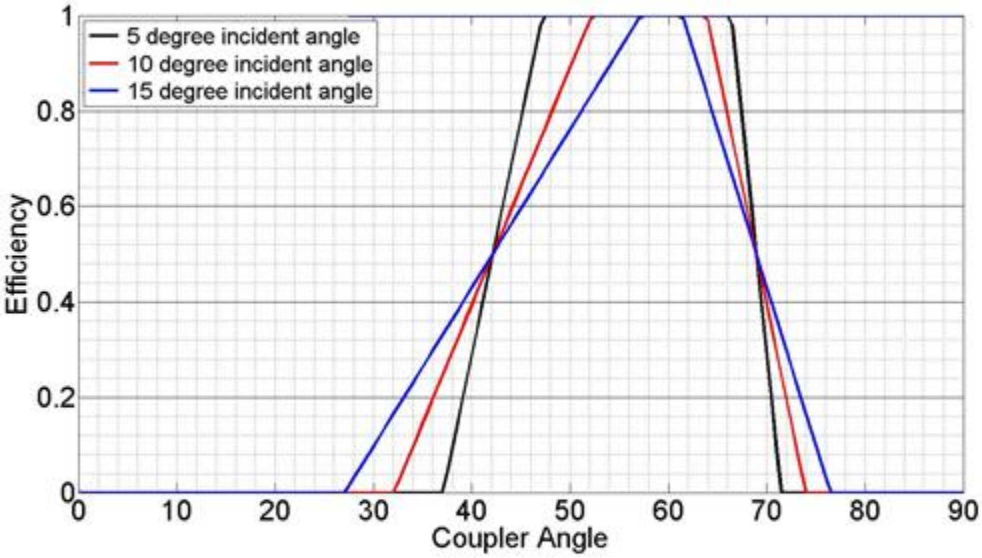

Figure 58. The relationship between the incident angle, coupler angle and efficiency for PMMA waveguide.

In order to reduce the decoupling loss and improve the performance of the waveguide solar concentrator system, a separate coupler with an attached aluminum mirror is used to couple to the waveguide in the new system, as shown in Figure 59. The sunlight can be reflected to the waveguide by the aluminum coated turning mirror and reach the PV cell at the end of the waveguide. In this case, there is no TIR coupling loss at the coupler surface and the coupling efficiency at the coupler surface will only depend on the reflectance of the coated metal. Also, the maximum incident angle at the coupler surface will depend on the critical angle of the waveguide material, which allows a large f-number Fresnel lens to attach to the system. Therefore, the system efficiency is increased due to the high reflectance turning mirror and the system can be more compact with a large f-number Fresnel lens array.

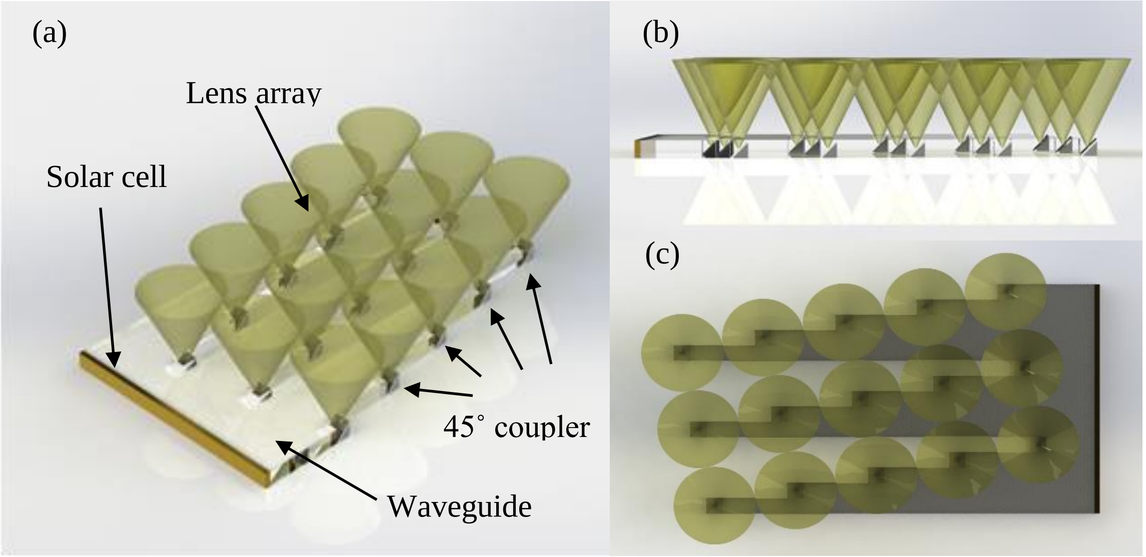

Figure 59. (a) A 3D view of lens-to-channel waveguide system with separated 45˚ coupler. (b) Side view and (c) top view of the system.

## 8.3 Experiment method

Figure 60 is a photograph of the CPV module used in this experiment. An 8 × 8 PMMA Fresnel lens array is used as the primary concentrator and is installed with an aluminum frame. The clear aperture of each lens is 60 mm × 60 mm. The f-number of the Fresnel lens is 1, which results in a 26.6° divergence angle at the coupler surface and the output of waveguide. The 45˚ aluminum coated coupler is aligned at the focal point of each lens and attached to the waveguide. A 5.5 mm × 6 mm PMMA waveguide array is used as the secondary optics to provide uniform irradiance, which is made by $CO_2$ laser cutting. All of the waveguides and couplers are positioned on an acrylic plate by low refractive index optical adhesive to reduce the TIR loss at the contact surface between the waveguide and holder. The bottom aluminum plate and the waveguide holder stage which is shown in Figure 50 (c) can be moved in horizontal and vertical direction. In this case, the coupler and waveguide can be aligned at the focal point of the lens array by adjusting the stage and bottom plate.

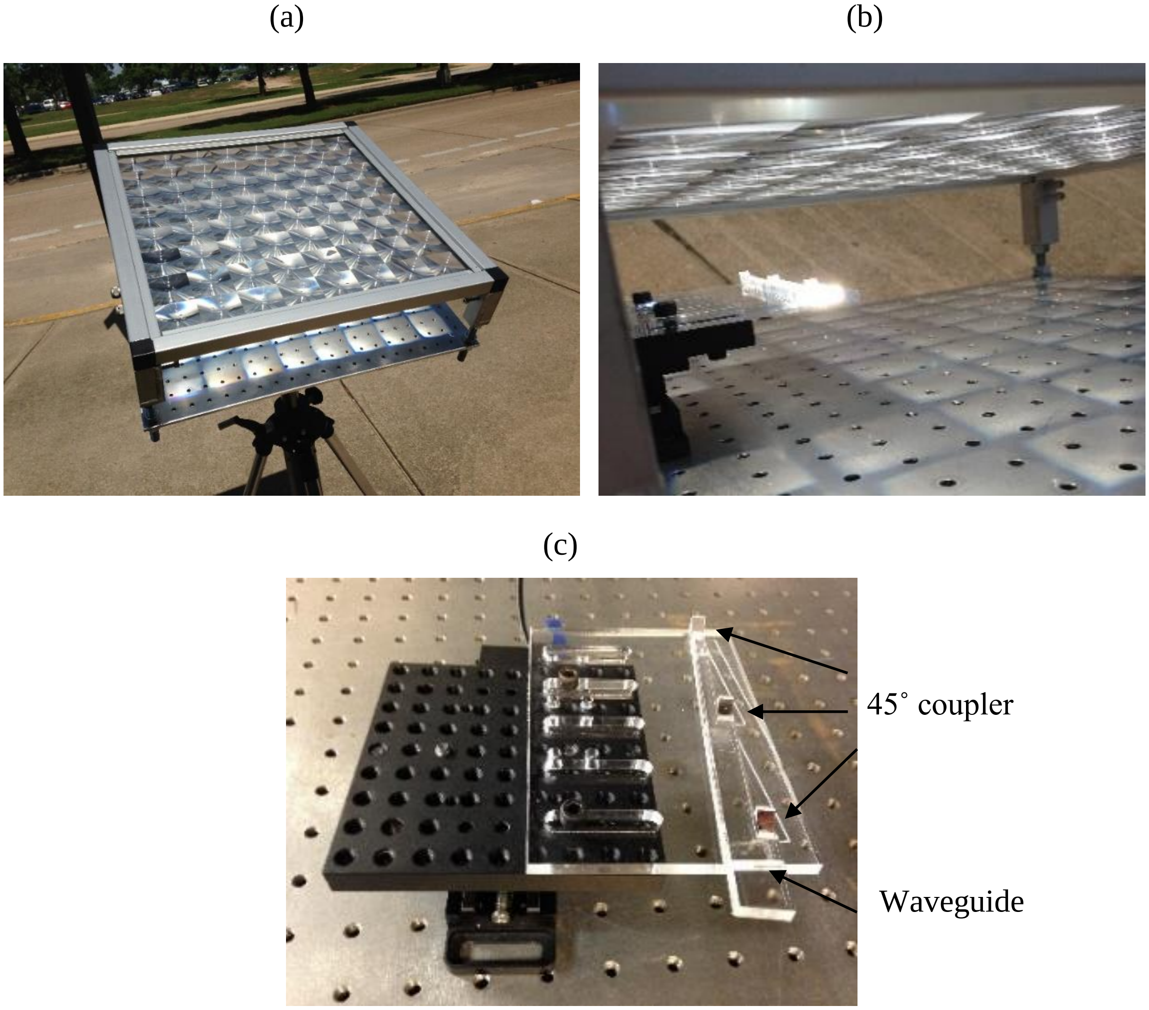

Figure 60. Photograph of (a) 8 × 8 Fresnel lens array, (b) waveguide holder stage and (c) the output of waveguide.

In order to test optical efficiency of the concentrator system, two photodiodes and an Apogee pyranometer are used as the detectors to measure the intensity of the input sunlight and the output of the waveguide. Figure 61 shows the diagram and photograph of the measurement setup. The geometric concentration of the system is defined as the ratio of the area of the collected incident sunlight to the area of the output of the waveguide:

$$C_{geo} = \frac{A_{in}}{A_{out}} \tag{8.1}$$

Thus, the geometric concentration of the system is around 109x and the intensity at the output of the waveguide will be more than 100, 000 W/m$^2$ under 100% efficiency condition, which leads to the fact that the current of photodiode will saturate at the output of the waveguide. A reflective neutral density (ND) filter is fixed at the top surface of the photodiode to provide uniform attenuation over the broad spectral range from 350 – 1200 nm. This ND filter has optical density 2.0, which allows 1% of the light reach to the photodiode from the output of the waveguide. The optical density d for an ND filter is defined as the logarithm of the ratio of the intensity after the filter to the intensity of the incident light:

$$d = -\log_{10} \frac{I_{out}}{I_{in}} \tag{8.2}$$

The diameter of the ND filter is 12.7 mm and the radiant sensitive area of photodiode is 1 mm $\times$ 1 mm. At the same time, another photodiode and an Apogee pyranometer are installed to the other side of the aluminum plate to measure the intensity of the input sunlight.

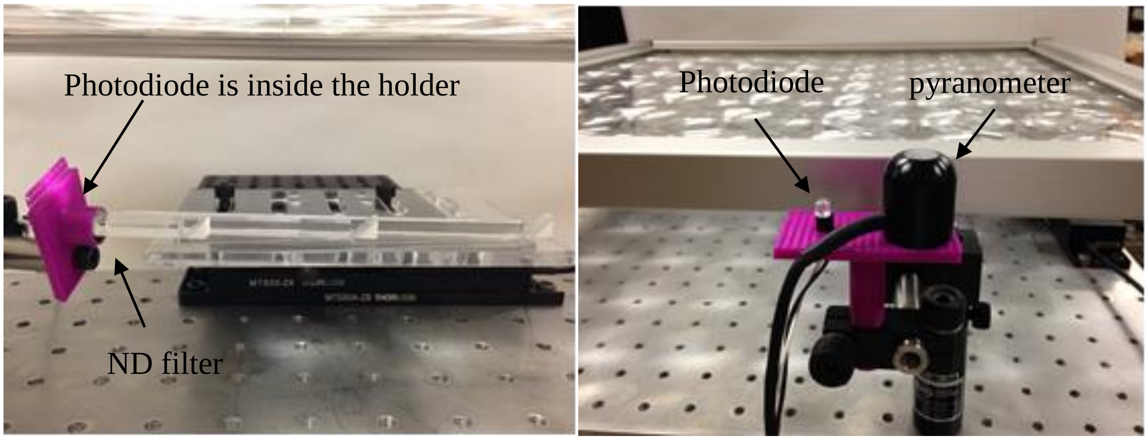

(a) (b)

Figure 61. Optical measurement setup for measuring (a) the intensity of the waveguide output and (b) the incident sunlight.

Since the f-number of the Fresnel lens is 1, the divergence angle of the lens is 26.6 ° which is smaller than the critical angle of the waveguide, all the light can propagate in waveguide by TIR. Also, the maximum angle of the light at the output of waveguide is 26.6 °. In order to get a more accurate measurement result, Figure 62 compares the angular response of the photodiode with an ideal cosine response and shows the linearity response of photodiode. This type of photodiode can collect around 90% of the light at 26.6 ° and have a linear relationship with light intensity up to 2200 W/m$^2$.

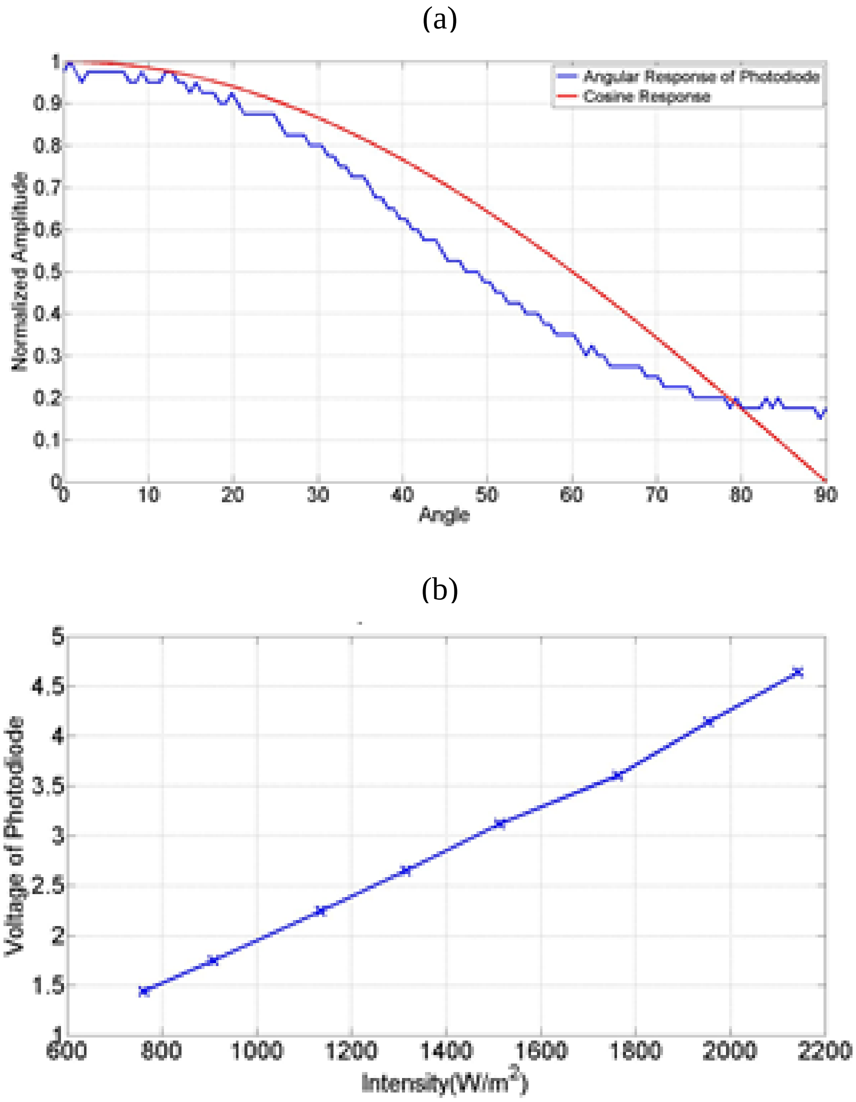

Figure 62. Angular response of photodiode and ideal cosine response. (b) Linearity response of photodiode.

Finally, a 6 mm × 6 mm MJ cell is positioned at the output of the waveguide, as shown in Figure 63. Since the waveguide dimension is 6 mm × 5.5 mm, the size of MJ cell is sufficient to collect all the irradiance from the waveguide if butt coupled with no intervening gap. A Keithley sourcemeter is used to measure the current and voltage of the MJ cell.

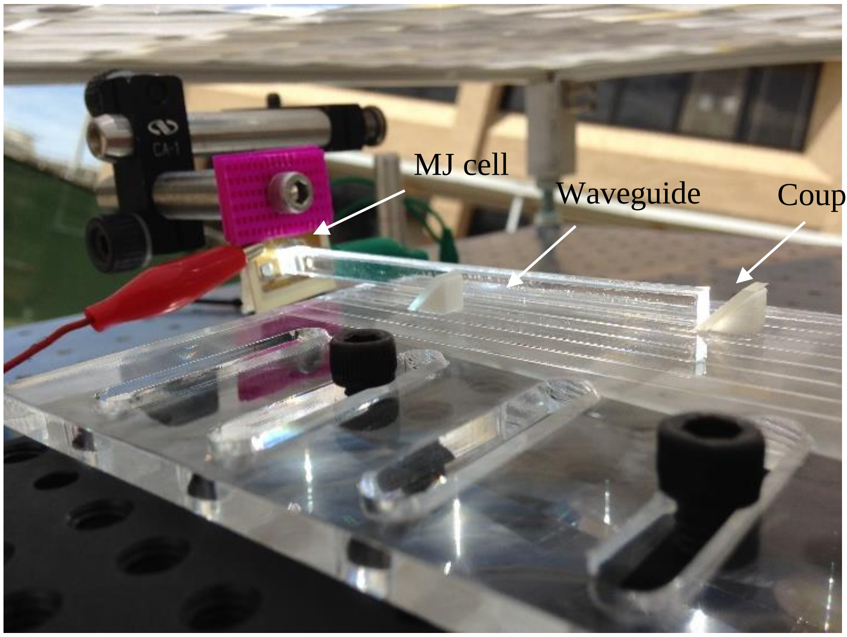

Figure 63. Measurement setup of the lens-to-channel waveguide system with a MJ cell.

### 8.4 Results and discussion

Table 8, Table 9 and Figure 64 show the ZEMAX simulation results of a 60 mm × 60 mm lens (f-number is 1) to a 6 mm × 5.5 mm PMMA straight waveguide with a separate aluminum coated coupler. Due to the Fresnel reflection loss the maximum transmission of the Fresnel lens is around 88%. Then, the transmission drops to 81% at the coupler surface, which mainly depends on the reflection of the coated surface. The reflection efficiency of an Al coated mirror is typically around 94%. Since the size of the mirror is 6 mm × 10 mm, which does not exactly match the size of the waveguide, 1.64% of the light cannot be coupled to the waveguide from the coupler. The refractive index difference between the air and waveguide material leads to the Fresnel reflection loss at the front and back surface of waveguide. Therefore, the maximum theoretical optical efficiency of this system is 75.4%. Since there is a divergence angle at the output of the waveguide, the position of the detector is also important to measure the output power. The detected power will reduce to less than 40% if the distance between the waveguide output and detector is larger than 1 mm.

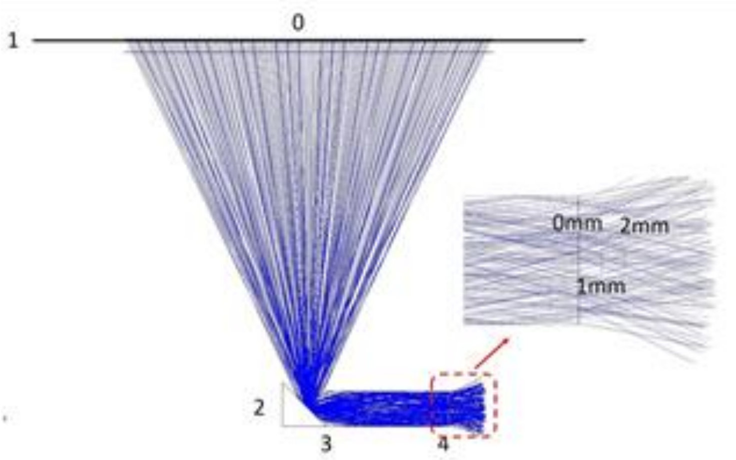

Figure 64. The simulation model in ZEMAX.

Table 8. ZEMAX simulation results of the system.

| | Interface | Transmission | Loss Source |
|---|---|---|---|
| 0 | Start | 100% | |
| 1 | Lens front/back | 88.25% | Fresnel reflection |
| 2 | Coupler | 81.68% | ~1.64% misses waveguide input<br>94.1% reflection from Al |
| 3 | Waveguide (front) | 78.49% | Fresnel reflection |
| 4 | Waveguide (output) | 75.40% | Fresnel reflection |

Table 9. Detected power verse distance from waveguide output.

| Distance from waveguide output | Percentage of detected power |
|---|---|
| 0 mm | 100% |
| 1 mm | 40.5% |
| 2 mm | 33.3% |

Figure 65 compares the V-I result of MJ cell with system concentration and without concentration. The experiment setup is shown in Figure 63, in which the MJ cell is attached to the output of the waveguide and is measured by Keithley sourcemeter. A 10 cm long PMMA waveguide is used in this measurement. The maximum power generated by MJ cell is 600 mW under Fresnel lens concentration and 288 mW with lens and waveguide system. The maximum transmission of an ideal 10 cm long PMMA waveguide is 78.89% at 400 nm to 1100 nm, based on absorption coefficient calculations [89].

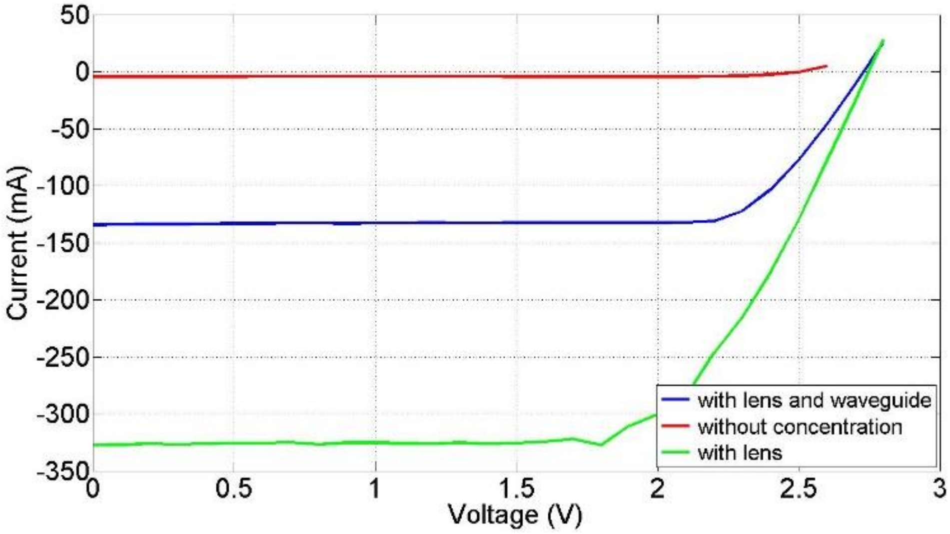

Figure 65. Measurement result of MJ cell V-I curve.

Table 10 compares the transmission and efficiency of the current system with the ideal system which has low loss components. In the measurement of the current system, the transmission of the lens and the reflection efficiency of the aluminum coated mirror are around 70% and 83.49%, respectively. The transmission of the waveguide and coupler is 54% which is measured in the lab. The transmission of the waveguide can be found using the transmission of the waveguide and coupler divided by the reflection efficiency of the coupler, which is around 65.3%. Therefore, the whole system efficiency is around 38.5%. The low efficiency of the waveguide is mainly due to absorption loss and scattering loss. Low loss waveguide materials and advanced fabrication processes are required to improve the waveguide transmission and system efficiency. The transmission would be close to 99% if using low OH silica as the waveguide material.

Alignment and tracking are also important to the designed system. The coupling efficiency at the coupler surface and waveguide depends on the accuracy of the tracking and alignment. In order to have low coupling loss, the focal point of the Fresnel lens has to be positioned at the center of the 45° coupler, which requires ±0.5° tolerance in tracking and alignment. For a system with better components, whose transmission is noted in Table 10, a system efficiency of 86% should be achievable.

Table 10. Measurement results of current system and estimated efficiency of the system with better components [53].

| | Transmission of the lens | Transmission of the waveguide and coupler | Efficiency of the system |
|---|---|---|---|
| Measurement in the lab | 70.59% | 54.52% | 38% |
| Measurement outside | 70.18% | 40.98% | 29% |
| System with better components | 92% | 94% | 86% |

## 8.5 Conclusion

The designed a lens-to-channel waveguide concentrator system which consists of a Fresnel lens array, 45° coupler and channel waveguide. In this system, an 8 × 8 square lens array which has a dimension of 60 mm × 60 mm and a PMMA multimode waveguide are used as the primary concentrator and the secondary concentrator, respectively. No further decoupling losses are encountered in the waveguide. An optical efficiency of 75.4% can be achieved according to our ZEMAX simulation. Experimental results based on 60 mm × 60 mm lens to one PMMA waveguide and MJ cell are also presented in Table 10. With better components and low loss material as the waveguide, a system efficiency of 86% can be achieved.

# CHAPTER IX

# CONCLUSION

CPV technology is of most interest for power generation in sun-rich regions with high efficiency. The idea of CPV technology is to use cheap optics such as lenses and mirrors to focal sunlight onto a tiny area of a PV cell. In this case, the cost of the PV system is reduced by replacing a large area of expensive PV cells with less expensive optical elements.

Our designed lens-to-channel waveguiding CPV system contains a lens array which is used as the essential concentrator, a channel waveguide array and MJ cells. Compared with the single Fresnel lens, the use of a lens array as the primary concentrator can absorb a large area of sunlight, but also reduce the thickness and weight of the whole system. Using waveguide as the secondary concentrator can reduce the connection problem of solar cell and further increase the concentration ratio by tapering the waveguide. Also, waveguide concentrator can provide uniform illumination on solar cell.

The designed CPV system with integrated 45˚ couplers inside the waveguide consists of a lens array with a diameter of 38 mm and a multimode waveguide array. The system have a concentration ratio of 126x and can be increased to 920x if using tapered glass waveguides instead of straight PMMA waveguides. The theoretical efficiency and experiment efficiency are 69.6% and 62.8%, respectively. The main losses are Fresnel loss, coupling loss and propagation loss.

The system with separated 45° couplers can significantly reduce the coupling loss at the coupling surface. The use of the aluminum or silver coated mirror as the separated coupler can increase the coupling efficiency due to the high reflectance of aluminum and silver. With better components and low loss material as the waveguide, a system efficiency of 86% can be achieved.

# REFERENCES

[1] R. Pode, B. Diouf, and SpringerLink (Online service). (2011). *Solar lighting*. Available: http://lib-ezproxy.tamu.edu:2048/login?url=http://dx.doi.org/10.1007/978-1-4471-2134-3

[2] Y. Chu and P. Meisen, "Review and Comparison of Different Solar Energy Technologies," Global Energy Network Institute2011.

[3] L. M. Fraas, *Low-Cost Solar Electric Power*: Springer International Publishing, 2014.

[4] Arthouros Zervos, "renewables 2015 global status report", REN21. 2015.

[5] D. Myers, *Solar radiation : practical modeling for renewable energy applications*, Taylor & Francis Group, 2013.

[6] Link: http://healingtones.org/2012/03/.

[7] M. Iqbal, *An introduction to solar radiation*. Toronto ; New York: Academic Press, 1983.

[8] Link: https://en.wikipedia.org/wiki/Horizontal_coordinate_system.

[9] P. I. Cooper, "The absorption of radiation in solar stills," *Solar Energy*, vol. 12, p. 333, 1969.

[10] Link: http://help.solidworks.com/2012/English/SolidWorks/.

[11] A. S. Blazev, *Solar technologies for the 21st century*.

[12] J. A. Duffie and W. A. Beckman, *Solar engineering of thermal processes*, 3rd ed. Hoboken, N.J.: Wiley, 2006.

[13] M. Naqi, *Encyclopaedia of Geomorphology*: Anmol Publications Pvt Ltd, 2006.

[14] "ISO 9845-1 Solar energy-Reference solar spectral irradiance at the ground at different receiving conditions," 1992.

[15] B. AE, *Comt Rend. Academie d. Sciences*, vol. 9, p. 561, 1839.

[16] A. Goetzberger and V. U. Hoffmann, *Photovoltaic solar energy generation*. Berlin ; New York: Springer, 2005.

[17] D. M. Chapin, C. S. Fuller, and G. L. Pearson, "A New Silicon P-N Junction Photocell for Converting Solar Radiation into Electrical Power," *Journal of Applied Physics,* vol. 25, pp. 676-677, 1954.

[18] B. L. Anderson and R. L. Anderson, *Fundamentals of semiconductor devices*. Boston: McGraw-Hill Higher Education, 2005.

[19] C. Kittel, *Introduction to solid state physics*, 6th ed. New York: Wiley, 1986.

[20] J. Singh, *Semiconductor devices : basic principles*. New York: Wiley, 2000.

[21] "Solar Cells: Materials, Manufacture and Operation, 2nd Edition," *Solar Cells: Materials, Manufacture and Operation, 2nd Edition,* pp. 1-641, 2013.

[22] A. P. Kirk and ebrary Inc., *Solar photovoltaic cells : photons to electricity*.

[23] Link: http://www.pveducation.org/pvcdrom/solar-cell-operation/open-circuit-voltage.

[24] R. A. Sinton and A. Cuevas, "Contactless determination of current–voltage characteristics and minority-carrier lifetimes in semiconductors from quasi-steady-state photoconductance data," *Applied Physics Letters,* vol. 69, pp. 2510-2512, 1996.

[25] M. A. Green, *Silicon solar cells: advanced principles & practice*: Centre for photovoltaic devices and systems, University of New South Wales, 1995.

[26] Link: http://hyperphysics.phy-astr.gsu.edu/hbase/tables/elabund.html.

[27] M. A. Green, K. Emery, Y. Hishikawa, W. Warta, and E. D. Dunlop, "Solar cell efficiency tables (Version 45)," *Progress in Photovoltaics,* vol. 23, pp. 1-9, Jan 2015.

[28] Link: http://www.solarbuzz.com/resources/blog/2014/02/new-us-trade-investigations-for-solar-pv-industry-any-winners.

[29] M. A. Green, "Thin-film solar cells: review of materials, technologies and commercial status," *Journal of Materials Science-Materials in Electronics,* vol. 18, pp. S15-S19, Oct 2007.

[30] W. Shockley and H. J. Queisser, "Detailed Balance Limit of Efficiency of P-N Junction Solar Cells," *Journal of Applied Physics,* vol. 32, pp. 510-&, 1961.

[31] L. El Chaar and N. El Zein, "Review of photovoltaic technologies," *Renewable and Sustainable Energy Reviews,* vol. 15, pp. 2165-2175, 2011.

[32] H. Cotal, C. Fetzer, J. Boisvert, G. Kinsey, R. King, P. Hebert*, et al.*, "III-V multijunction solar cells for concentrating photovoltaics," *Energy Environ. Sci,* vol. 2, 2009.

[33] F. Dimroth, M. Grave, P. Beutel, U. Fiedeler, C. Karcher, E. O. Thomas N. D. Tibbits1, Gerald Siefer1, Michael Schachtner1, Alexander Wekkeli1,*, et al.*, "Wafer bonded four-junction GaInP/GaAs//GaInAsP/GaInAs concentrator solar cells with 44.7% efficiency," *Prog. Photovolt: Res. Appl,* vol. 22, 2014.

[34] S. V, Y. H, and W. M, "High-efficiency multijunction solar cells employing dilute nitrides," presented at the 8th International Conference on Concentrating Photovoltaic Systems., 2012.

[35] G. JF, FriedmanDJ, W. JS, D. A, OlavarriaWJ, K. J. Moriarty TE, RomeroMJ, Norman AG, Jones*, et al.*, "40.8% efficient inverted triple-junction solar cell with two independently metamorphic junctions," *Applied Physics Letters,* vol. 93, 2008.

[36] S. K, A. T, N. K, T. N, O. R, and T. T, "Development of InGaP/GaAs/InGaAs inverted triple junction concentrator solar cells," presented at the 9th International Conference on Concentrator Photovoltaic Systems, Miyazaki, Japan, 2013.

[37] P. Singh and N. M. Ravindra, "Temperature dependence of solar cell performance—an analysis," *Solar Energy Materials and Solar Cells,* vol. 101, pp. 36-45, 2012.

[38] V. Tyagi, N. A. Rahim, N. Rahim, A. Jeyraj, and L. Selvaraj, "Progress in solar PV technology: Research and achievement," *Renewable and Sustainable Energy Reviews,* vol. 20, pp. 443-461, 2013.

[39] E. Cuce, P. M. Cuce, and T. Bali, "An experimental analysis of illumination intensity and temperature dependency of photovoltaic cell parameters," *Applied Energy,* vol. 111, pp. 374-382, 2013.

[40] N. Shenck, "Alternative energy systems," *US Naval Academy Lecture Readings*, 2010.

[41] H. Jiang, L. Lu, and K. Sun, "Experimental investigation of the impact of airborne dust deposition on the performance of solar photovoltaic (PV) modules," *Atmospheric Environment*, vol. 45, pp. 4299-4304, 2011.

[42] S. Mekhilef, R. Saidur, and M. Kamalisarvestani, "Effect of dust, humidity and air velocity on efficiency of photovoltaic cells," *Renewable and Sustainable Energy Reviews*, vol. 16, pp. 2920-2925, 2012.

[43] Link: http://www.seia.org/research-resources/solar-market-insight-report-2015-q1.

[44] Link: http://www.eia.gov/renewable/annual/solar_photo/.

[45] D. Gielen, "Renewable energy technologies: cost analysis series," *Sol Photovolt*, vol. 1, p. 52, 2012.

[46] S. Philipps, A. Bett, K. Horowitz, and S. Kurtz, "Current Status of Concentrator Photovoltaic (CPV) Technology," National Renewable Energy Laboratory (NREL), Golden, CO.2015.

[47] A. Luque and S. Hegedus, *Handbook of photovoltaic science and engineering*: John Wiley & Sons, 2011.

[48] M. A. Green, *Third generation photovoltaics*: Springer, 2006.

[49] P. Benıtez and J. Miñano, "Concentrator optics for the next-generation photovoltaics," *Next Generation Photovoltaics*, p. 285, 2003.

[50] A. Davis and F. Kühnlenz, "Optical design using Fresnel lenses," *Optik & Photonik*, vol. 2, pp. 52-55, 2007.

[51] O. Miller, J. McLeod, and W. Sherwood, "Thin sheet plastic Fresnel lenses of high aperture," *JOSA*, vol. 41, pp. 807-814, 1951.

[52] W. Xie, Y. Dai, R. Wang, and K. Sumathy, "Concentrated solar energy applications using Fresnel lenses: A review," *Renewable and Sustainable Energy Reviews*, vol. 15, pp. 2588-2606, 2011.

[53] V. Kumar, R. Shrivastava, and S. Untawale, "Fresnel lens: A promising alternative of reflectors in concentrated solar power," *Renewable and Sustainable Energy Reviews*, vol. 44, pp. 376-390, 2015.

[54] R. Leutz and L. Fu, "Dispersion in tailored Fresnel lens concentrators," in *Proceedings of ISES World Congress 2007 (Vol. I–Vol. V)*, 2009, pp. 1366-1370.

[55] Link: http://www.mathopenref.com/subtend.html.

[56] P. Benítez and J. C. Miñano, "Concentrator optics for the next-generation photovoltaics," in *Next Generation Photovoltaics*, ed: Taylor & Francis, 2003.

[57] K. Lovegrove and W. Stein, *Concentrating solar power technology: Principles, developments and applications*: Elsevier, 2012.

[58] H. Baig, K. C. Heasman, and T. K. Mallick, "Non-uniform illumination in concentrating solar cells," *Renewable and Sustainable Energy Reviews*, vol. 16, pp. 5890-5909, 2012.

[59] J. S. Coventry, "Performance of a concentrating photovoltaic/thermal solar collector," *Solar Energy*, vol. 78, pp. 211-222, 2005.

[60] H. Cotal, C. Fetzer, J. Boisvert, G. Kinsey, R. King, P. Hebert, *et al.*, "III–V multijunction solar cells for concentrating photovoltaics," *Energy & Environmental Science*, vol. 2, pp. 174-192, 2009.

[61] S. Hatwaambo, K. Chinyama, M. Mwamburi, and B. Karlsson, "Fill factor improvement in non-imaging reflective low concentrating photovoltaic," in *Clean Electrical Power, 2007. ICCEP'07. International Conference on*, 2007, pp. 335-340.

[62] I. Anton and G. Sala, "Losses caused by dispersion of optical parameters and misalignments in PV concentrators," *Progress in Photovoltaics: Research and Applications*, vol. 13, pp. 341-352, 2005.

[63] M. Sabry and A. E. Ghitas, "Effect of edge shading on the performance of silicon solar cell," *Vacuum*, vol. 80, pp. 444-450, 2006.

[64] R. Schultz, F. Vorster, and E. van Dyk, "Performance of multi-junction cells due to illumination distribution across the cell surface," *Physica B: Condensed Matter,* vol. 407, pp. 1649-1652, 2012.

[65] E. Franklin and J. Coventry, "Effects of highly non-uniform illumination distribution on electrical performance of solar cells," *Made available in DSpace on 2011-01-05T08: 26: 50Z (GMT). No. of bitstreams: 3 ANZSES_2002_ETF. pdf. jpg: 3099 bytes, checksum: 73672974543080a819ddcfa66bd789cb (MD5) 1779-01.2003-07-23T02: 13: 43Z. xsh: 360 bytes, checksum: 6c895093b97c406800532d2421025f80 (MD5) ANZSES_2002_ETF. pdf: 1361372 bytes, checksum: 9b76fbcbd4dc8d38542190fba56c7a1c (MD5) Previous issue date: 2004-05-19T13: 00: 35Z*, 2002.

[66] Y. Tripanagnostopoulos, "Linear Fresnel lenses with photovoltaics for cost effective electricity generation and solar control of buildings," in *4th International conference on solar concentrators for the generation of electricity or hydrogen. El Escorial*, 2007.

[67] N. Sarmah, B. S. Richards, and T. K. Mallick, "Evaluation and optimization of the optical performance of low-concentrating dielectric compound parabolic concentrator using ray-tracing methods," *Applied optics*, vol. 50, pp. 3303-3310, 2011.

[68] R. Herrero, M. Victoria, C. Domínguez, S. Askins, I. Antón, and G. Sala, "Concentration photovoltaic optical system irradiance distribution measurements and its effect on multi-junction solar cells," *Progress in Photovoltaics: Research and Applications,* vol. 20, pp. 423-430, 2012.

[69] F. Ghani, G. Rosengarten, M. Duke, and J. Carson, "On the influence of temperature on crystalline silicon solar cell characterisation parameters," *Solar Energy*, vol. 112, pp. 437-445, 2015.

[70] A. B. Or and J. Appelbaum, "Dependence of multi-junction solar cells parameters on concentration and temperature," *Solar Energy Materials and Solar Cells,* vol. 130, pp. 234-240, 2014.

[71] K. Nishioka, T. Takamoto, T. Agui, M. Kaneiwa, Y. Uraoka, and T. Fuyuki, "Annual output estimation of concentrator photovoltaic systems using high-efficiency InGaP/InGaAs/Ge triple-junction solar cells based on experimental solar cell's characteristics and field-test meteorological data," *Solar Energy Materials and Solar Cells*, vol. 90, pp. 57-67, 2006.

[72] G. Lifante, *Integrated photonics : fundamentals*. Chichester, England ; Hoboken, NJ: J. Wiley, 2003.

[73] Link: https://en.wikipedia.org/wiki/Total_internal_reflection.

[74] R. G. Hunsperger, *Integrated optics: theory and technology* vol. 2: Springer, 1984.

[75] A. Boudrioua, "Optical Waveguide Characterization Techniques," in *Photonic Waveguides*, ed: ISTE, 2010, pp. 77-123.

[76] J. H. Karp, E. J. Tremblay, and J. E. Ford, "Planar micro-optic solar concentrator," *Optics express*, vol. 18, pp. 1122-1133, 2010.

[77] J. H. Karp, E. J. Tremblay, J. M. Hallas, and J. E. Ford, "Orthogonal and secondary concentration in planar micro-optic solar collectors," *Optics express*, vol. 19, pp. A673-A685, 2011.

[78] W.-C. Shieh and G.-D. Su, "Compact solar concentrator designed by minilens and slab waveguide," in *SPIE Solar Energy+ Technology*, 2011, pp. 81080H-81080H-9.

[79] S. Bouchard and S. Thibault, "Planar waveguide concentrator used with a seasonal tracker," *Applied optics*, vol. 51, pp. 6848-6854, 2012.

[80] S.-C. Chu, H.-Y. Wu, and H.-H. Lin, "Planar lightguide solar concentrator," in *SPIE Photonics Europe*, 2012, pp. 843810-843810-7.

[81] H.-Y. Wu and S.-C. Chu, "Ray-leakage-free sawtooth-shaped planar lightguide solar concentrators," *Optics express*, vol. 21, pp. 20073-20089, 2013.

[82] Y. Liu, R. Huang, and C. K. Madsen, "A lens-to-channel waveguide solar concentrator," in *Optics for Solar Energy*, 2013, p. RT3D. 1.

[83] Y. Liu, R. Huang, and C. K. Madsen, "Design of a lens-to-channel waveguide system as a solar concentrator structure," *Optics express,* vol. 22, pp. A198-A204, 2014.

[84] A. Borreman, S. Musa, A. Kok, M. Diemeer, and A. Driessen, "Fabrication of polymeric multimode waveguides and devices in SU-8 photoresist using selective polymerization," 2002.

[85] Link: https://en.wikipedia.org/wiki/Numerical_aperture.

[86] R. Huang, Y. Liu, and C. Madsen, "First demonstration of a novel 2D-waveguiding solar concentrator," in *SPIE Solar Energy+ Technology*, 2014, pp. 91750N-91750N-7.

[87] Y.-G. Zhao, W.-K. Lu, Y. Ma, S.-S. Kim, S. Ho, and T. Marks, "Polymer waveguides useful over a very wide wavelength range from the ultraviolet to infrared," *Applied Physics Letters*, vol. 77, pp. 2961-2963, 2000.

[88] R. Huang, Y. Liu, and C. Madsen, "Demonstration of an intermediate-scale lens-to-channel waveguide solar concentrator," in *SPIE Optics+ Photonics for Sustainable Energy*, 2015, pp. 955903-955903-7.

[89] L. Hornak, "Polymers for lightwave and integrated optics: technology and applications," *Marcel Dekker, Inc, 270 Madison Ave, New York, New York 10016, USA, 1992. 768,* 1992.